3-24-2016

Surface Roughness of Electron Beam Melting TI-6AL-4V Effect on Ultrasonic Testing

Evan T. Hanks

SURFACE ROUGHNESS OF ELECTRON BEAM MELTING TI-6AL-4V EFFECT ON ULTRASONIC TESTING

THESIS

Evan T. Hanks, Captain, USAF

AFIT-ENY-MS-16-M-216

DEPARTMENT OF THE AIR FORCE
AIR UNIVERSITY

AIR FORCE INSTITUTE OF TECHNOLOGY

Wright-Patterson Air Force Base, Ohio

AFIT-ENY-MS-16-M-216

SURFACE ROUGHNESS OF ELECTRON BEAM MELTING TI-6AL-4V EFFECT ON ULTRASONIC TESTING

THESIS

Presented to the Faculty

Department of Aeronautics and Astronautics

Graduate School of Engineering and Management

Air Force Institute of Technology

Air University

Air Education and Training Command

In Partial Fulfillment of the Requirements for the

Degree of Master of Science in Aeronautical Engineering

Evan T. Hanks, BS

Captain, USAF

March 2016

AFIT-ENY-MS-16-M-216

SURFACE ROUGHNESS OF ELECTRON BEAM MELTING TI-6AL-4V EFFECT ON ULTRASONIC TESTING

Evan T. Hanks, BS

Captain, USAF

Committee Membership:

Maj David Liu, PhD
Co-Chair

Dr. Anthony Palazotto, PhD
Co-Chair

Dr. Edwin Schwalbach, PhD
Member

Abstract

Experimental research was conducted on the effects of surface roughness on ultrasonic non-destructive testing of Electron Beam Melted (EBM) additively manufactured Ti-6Al-4V. Additive Manufacturing (AM) is a developing technology with many potential benefits, but certain challenges posed by its use require further research before AM parts are viable for widespread use in the aviation industry. Possible applications of this new technology include, Aircraft Battle Damage Repair (ABDR), small batch manufacturing to fill supply gaps, and replacement for obsolete parts. The research presented here assesses the effectiveness of ultrasonic inspection in detecting manufactured flaws in EBM manufactured Ti-6Al-4V. EBM products are known to have high surface roughness in as-manufactured condition, and surface roughness is known to affect the results of ultrasonic inspections. The experimental data from this research demonstrates the ability of ultrasonic inspections to identify flaws as small as 0.51 mm at 2.25 MHz, 5 MHz and 10 MHz through a machined surface. A frequency of 10 MHz provides better results than 2.25 MHz and 5 MHz through an as manufactured surface, where the highest natural surface roughness is present.

Acknowledgments

I would like to express my sincere gratitude to my research advisors, Maj David Liu and Dr. Anthony Palazotto, for their guidance and support throughout the course of this thesis effort. Their insight and experience was invaluable and appreciated. I would also like to recognize Dr. Edwin Schwalbach for the guidance and for allowing me to work with him on such an important project, Dr. Eric Lindgren for the support and resources, and Josiah Dierken for the training and coding assistance. Additionally I would like to thank my sponsors, Mr. Dennis Lindell from the Joint Aircraft Survivability Program Office, and Mr. Don Littrell of the Munitions Directorate, AFRL for both the support and latitude provided to me in this endeavor. Finally, I extend my sincere appreciation to my wife for all of her support throughout my time at AFIT.

Evan T. Hanks

Table of Contents

Page

List of Figures

Page

List of Tables

Page

SURFACE ROUGHNESS OF ELECTRON BEAM MELTING TI-6AL-4V

EFFECT ON ULTRASONIC TESTING

I. Introduction

1.1 Motivation for Research

Additive manufacturing (AM) is a relatively new technology making an appearance in Japan in 1981. A photo-hardening polymer and ultraviolet light were used to manufacture small samples and prototypes in this original form of the technology [1]. In a fairly short period of time, this technology has grown from small plastic models to complex metallic geometries [2]. Given the flexibility and potential of AM, various industries are able to harness this new technology more than ever before, including the aviation and aerospace industries. Benefits to AM include significant cost savings, reduced production time, and virtually no waste. As technology has advanced, AM equipment has gotten smaller while allowing the manufacture of larger parts. Rapid advancement within the field has allowed for one piece of equipment to replace an entire production facility. Reducing the manufacturing footprint would bring greater flexibility to field level units and those in deployed locations, allowing on-site component fabrication.

The use of "3D-printing" is quickly spreading. What was once used as a technology for companies and developers to make basic prototypes has grown into a burgeoning and expansive new field that is changing the fabrication industry. In the past few years AM has opened up to anyone with an idea and access to a computer. Retail office supply chains, shipping stores, and even small startup companies have capitalized on this

growing field, putting the power of AM into the hands of the general public. This rapid spread of technology has even led to 3D-printing's incorporation into vending machines. A customer can upload a design and have an item in hand with the simplicity and convenience of purchasing a soft drink [3]. AM is a rapidly growing industry, increasing 83% in just two years as manufactures are realizing the added benefits and decreasing costs of AM [4, 5]. A major contributing factor to the rapid growth of AM is the ever expanding material selection available; these materials include various steels, aluminum, and titanium alloys [6]. The growth of available materials from simple low strength plastics to high strength alloys has opened the door to custom, as needed, manufacturing of components.

According to a 2012 report from the Institute for Defense Analyses, AM has the potential to change the fundamentals of manufacturing in the future. Industrial AM machines are expected to continue to improve as quality control increases and material innovations come to the market. It is expected by the year 2030, machines will construct entire assemblies at once from multiple materials [5]. This capability is very attractive prospect in any industry and will likely find a niche in the field of aviation. AM allows designers to create complex optimized designs which were restricted by previous manufacturing techniques [2]. Due to the freedom of design and high levels of component complexity with essentially no additional cost, future aircraft can incorporate optimized designs not limited to today's manufacturing techniques [7]. Reduced weight and increased strength will translate to lower fuel consumption and lower cost of operation in future aircraft that are optimally designed using AM [7]. The 2010 Air Force

Energy Plan calls for research and development to deliver new technologies required to reduce energy consumption. With 2.5 billion gallons of jet fuel consumed by the US Air Force in 2010, nearly 50% of the entire Department of Defense's fuel use, optimization of future aircraft design will contribute greatly to the Air Force's 2030 energy end state goal [8]. AM gives this flexibility of optimization to the designers of the next generation of DOD aircraft.

AM stands to play a crucial role in the future of aircraft sustainment. Many DOD aircraft are retained and utilized well beyond their design service life. This leads to parts failing which were never intended for replacement, therefore replacements may not exist. Through traditional manufacturing techniques, such as forging and machining, remanufacturing an outdated part can take up to two years [5]. This time does not include testing for qualification and delivery of the completed item. Traditional manufacturing not only costs substantially more than the original component, but may lead to grounding of aircraft for extended periods of time [5]. A potential solution to these problems is the use of AM, where small quantities of parts are manufactured in a fraction of the time at substantially lower costs. Titanium alloy parts were identified as the first likely candidate for this supply chain solution. In 2011, the U.S. Navy and the Defense Logistics Agency identified over 300 titanium alloy parts with a production time estimated at over one year [5]. The use of AM to manufacture these long production time and often obsolete parts could alleviate years of logistical backlogs.

Certain roadblocks stand in the way of on-demand aircraft parts manufacturing. The first of these barriers is the need for a process to qualify parts for use in a weapon

system. Traditional production run sampling and first article testing can add significant time and money to the cost of spares. For low number productions, where AM has the most benefit, this qualification process could negate any potential cost or time savings [5]. Another issue is the need for the spare parts required to have digital designs [5]. Many airframes in the current Air Force inventory were designed in the 1950's and have no 3-D digital files for the vast number of parts comprising them [9]. As these aircraft are retired over the next few decades and newer model aircraft are brought in as replacements, more components will have computer based models. This will increase the number of parts available for manufacturing using AM without the repetitive task of redesigning the part.

Among the challenges to qualify AM components for use in aircraft, is the need to nondestructively inspect finished products throughout the life of the system they are used on. According to a 2014 NASA report, "the impact of Nondestructive Evaluation (NDE) on AM is crosscutting and spans materials, processing, quality assurance, testing, and modeling disciplines. Simply put, NDE techniques are needed before, during, and after the AM production process." [10] Certain technology gaps exist in terms of materials, processes and equipment as well as standards. The avenue to validate, verify, and qualify AM parts is of universal concern throughout the industry as well as throughout the government. Adoption of parts made by AM is hampered by doubt in the current Nondestructive Inspection (NDI) based validation approaches. Current NDI methods are not optimized for AM materials or processes. The use of traditional NDI techniques for completed AM components are either untested or still emerging [10]. In 2013, the

National Institute of Standards and Technology (NIST) laid out a roadmap for metal based AM. Included in this roadmap was a 5 year action plan to explore and develop NDI techniques and protocols. One of the first steps outlined in this NIST roadmap is to benchmark AM measurements, accuracies, and NDI techniques to enable process performance validation [11]. Current industry and government research is split into two distinct categories, *in situ* process NDI, and post process NDI. The focus of *in situ* NDI is to provide real-time effective feedback to the AM equipment to allow for detection or mitigation of anomalies [11]. Post process NDI is also a concern and is laid out in a five year plan of evaluation and development by the NIST. This plan calls for proven techniques based on adapting existing NDI practices to meet the needs of AM [11].

1.2 Research Scope

The purpose of this research is to investigate the use of ultrasonic nondestructive testing (UT) on Electron Beam Melting (EBM) Ti-6Al-4V. Due to the variability in manufacturing using EBM, surface finish is less than desirable for traditional forms of field level NDI. Additional data will help develop a greater understanding of inspection technique and surface finish requirements. Existing research conducted at various NASA facilities has focused on using UT to inspect inconel, aluminum, and titanium manufactured using the electron beam freeform fabrication (EMF3) [10]. The focus of the research conducted in this study is to investigate the impact of surface finish on UT of EBM Ti-6Al-4V. Surface conditions tested in this thesis are representative of parts in manufactured condition as well as those which have received post process machining.

1.3 Problem Statement

Current Air Force Research Laboratory (AFRL) efforts have focused on computer tomography (CT) inspection of Ti-6Al-4V. Previous work has shown high fidelity results with a resolution in the range of 38-51 μm [12]. CT is not a standard USAF NDI technique requiring extensive equipment [13]. It is known CT does not perform crack detection well, and requires large amounts of time for data acquisition and analysis [10]. Alternately, UT is a standard USAF NDI method and is widely used throughout the aircraft maintenance and repair industry [13]. Current guidance and practices for NDI of metallic parts using UT does not address the uniqueness of AM. Previous research has shown unfavorable results using conventional NDI techniques, mainly eddy current, on as manufactured surfaces. Flaws were not discernable from general surface noise [10]. Given the lack of reliable analytical data to correlate surface roughness to flaw detection using NDI, this research will attempt to determine if surface finish causes a measureable difference in flaw detection of EBM titanium alloy samples.

1.4 Research Objectives

The goal of this research is to assess the effect of surface roughness on NDI of EBM Ti-6Al-4V alloy. To offer an assessment of the surface finish this research will focus on the following objectives:

1. Determine to what extent an as-manufactured versus a machined surface affects the ability of UT to detect known defects in a Ti-6Al-4V sample.
2. Determine detectable size of flaw as a function of ultrasonic frequency, on a range of frequencies from 2.25 to 10 MHz.

3. Determine the effect of depth of a defect on the detectability over a range of frequencies from 2.25 to 10 MHz

To reach these objectives, data was collected from twelve samples in six configurations, as manufactured, milled and ground on both the top and side surfaces. All samples were manufactured by Oakridge National Laboratories on either the Arcam model A2 or Q10 machine. Four of the twelve samples were manufactured using recycled powder from previous builds. This will provide a minimum of four surface finishes for which to collect data on each of the twelve samples as well as two potentially different powder configurations.

1.5 Assumptions and Limitations

The research conducted contains experimental data collected from EBM Ti-6-4 titanium alloy. Given the limits of time, resources, and equipment, results are intended to correlate surface roughness to detectable flaw size characteristics. The testing reflects the quality of the manufacturing technique as well as the raw materials used to manufacture the samples. This research does not attempt to qualify any manufacturing method or input conditions to the EBM or any other AM process. The input parameters of each specific build were set by the machine manufacture and are not within the scope of this research.

1.6 Chapter Outline

This research will begin in Chapter 2 with a literature review of the fundamental aspects that make up AM and UT. The methodology for the research is then covered in Chapter 3. The topics covered are data collection methods as well as data processing.

The results of the processed data is then discussed in Chapter 4. The report will conclude with Chapter 5, including recommendations for future work.

II. Background & Theory

2.1 Additive Manufacturing Overview

Additive manufacturing is a layered based approach used in manufacturing solid three dimensional parts of varying shapes [14]. As the name implies, AM is additive in nature as opposed to traditional subtractive manufacturing techniques such as machining or cutting. AM allows the direct manufacture of parts from computer generated files; this characteristic leads to AM's categorization as a direct digital manufacturing technique. Several techniques currently exist for metal fabrication within the realm of AM; these include Direct Metal Laser Sintering (DMLS), Direct Metal Deposition (DMD), Electron Beam Free Form Fabrication (EBF3) and Electron Beam Melting (EBM) [15]. This report will focus on the EBM method of layer based additive manufacturing.

The world was first introduced to AM in 1981 when Hideo Kodama of Nagoya, Japan presented his review of three dimensional plastic modeling with a photo-hardening polymer. The earliest versions of AM in the United States were called Stereolithography Rapid Printing Systems, and used a programmed movable ultraviolet beam to cure layers of a liquid acrylate compound [16]. This was the first generation of AM which would quickly spread throughout the world [1]. This early form of AM was used as a low cost way to produce three dimensional prototypes and scaled models during preliminary stages of design in multiple industries [17]. As the usefulness and value of AM were realized, the market has seen an increasing number of processes and equipment. With the

advancements in technology and competition in business, manufacturers have developed AM machines capable of creating items from various metals, ceramics, and plastics. These advancements have led to AM becoming more affordable and dynamic removing many barriers between design and production [7].

2.2 Powder Bed Fusion

Powder bed fusion (PBF) was among the first commercial AM processes developed. The University of Texas developed a PBF process called Selective Laser Sintering (SLS). Additional PBF techniques have seen development in recent years, including EBM. PBF opened the field of AM to a wide range of metals and ceramics. Despite its limitations, PBF also brought many new capabilities to AM. To date PBF has proven to provide flexibility not achievable by other AM approaches [14].

As the name suggests PBF uses powder of the desired material to create end products. This powder is metallic, ceramic, or polymer and is stored in a reservoir or a hopper until it is deposited on the build surface. The build platform, also known as build plate or bed is a movable surface on which the part is created. During the manufacturing process powder is retrieved from a hopper by a rotating roller, rake, or blade and spread into an even layer over the build plate. This layer is then selectively melted using either a laser in SLS or an electron beam in EBM. The unmelted powder remains on the build platform and acts as a means of support as the part is built. Once the necessary areas of the powder layer are melted, the build platform is then lowered and a new layer of powder is added. This process is repeated as needed to create the end item.

The original development of SLS as with many AM processes began with manufacturing plastic prototypes. This process used a point-wise laser scanning technique. Technological improvements advanced SLS, allowing for metal and ceramic powder use to create more than just plastic models. Techniques have also evolved moving from point-wise melting to layer-wise fusion. In the manufacture of complex metal components, one of four common approaches is used: full melting, liquid-phase sintering, solid-state sintering, and chemically-induced binding. Full melting relies on a laser or electron beam to heat the powder to a molten state, creating each layer of a component. Liquid-phase sintering is arguably the most versatile form of PBF [14]. During liquid-phase sintering a portion of the powder particles are melted while the remainder are left solid. The molten particles cool to act as a glue holding together the often higher temperature particles. Solid-state sintering refers to fusion of powder particles without melting at elevated temperatures. To achieve this, a temperature less than the melting point of the powder is used. With this technique, sintering time and temperature are adjusted to achieve various porosity levels. Chemically-induced sintering relies on thermally activated chemical reactions between different powders or between a powder and atmospheric gasses. This reaction forms a by-product which bonds the powder together. This technique has allowed the use of structural ceramics in AM. Ceramic materials usually having high melting temperatures are sintered using this process, but also require post process high temperature furnace sintering. The cost and time associated with the additional processing has led to limited use in commercial equipment. Among these four techniques, full melting remains the most common due to

the ability to produce well bonded, dense structures from common engineering alloys [14].

2.3 Electron Beam Melting

EBM was developed by Arcam, a Swedish company founded in 1997 [18]. EBM is a direct digital manufacturing technique, producing near net shape parts from powdered metal. The EBM technology has the ability to build dense parts using a fully computer controlled automated system with minimal interaction during the build process [18]. EBM systems are power efficient as compared to other AM systems [19]. A high vacuum maintained in the build chamber provides a controlled environment, which ensures material purity is held throughout the build process [20].

The EBM systems manufactured by Arcam consist of an electron beam generating system, a build chamber, and the computer system used to control the build process, see Figure 1. The electron beam generating system, also called the Electron Gun, generates a beam by passing current through a tungsten filament, causing the filament to heat and emit electrons. This continuous flow of electrons is focused by a series of lenses as it passes into the build chamber. The position of the electron beam's focus on the built table is controlled by deflection coils or a set of deflection lenses [18].

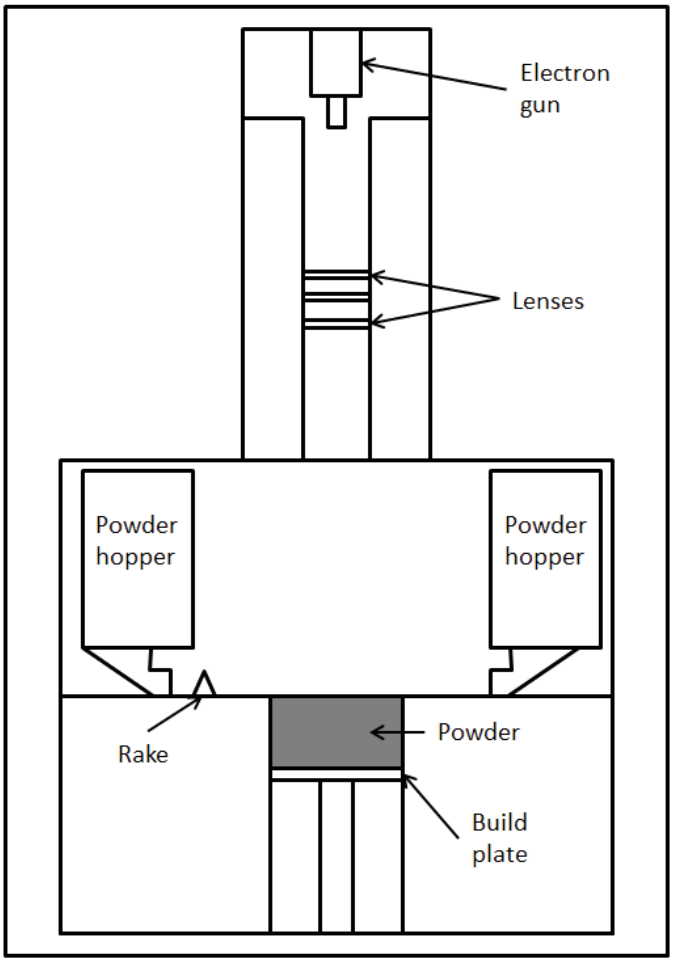

Figure 1. EBM manufacturing machine primary components [21]

As with most AM, the buildup process starts with a Computer Aided Design (CAD) model [11]. This model is then sliced into layers, typically on the order of 50 μm thick. The EBM system then physically reproduces the computer slices layer by layer, melting metal powder in the build chamber only in locations necessary to produce the desired shape [18]. Once each layer is melted as designated by the computer, the stainless steel build table is lowered the distance corresponding to the layer thickness. A thin layer of powder, approximately 100 μm, is deposited over the build table using a

rake. The rake fetches the powder from one of two hoppers on either side of the build table. A preheating sequence is used prior to melting to maintain an elevated temperature in the build chamber and to increase build rate. This process is repeated until the entire component is complete. The build table is typically made of stainless steel, where the thermal properties differ from those of the working powdered metal, allowing for removal of the completed component from the build table [18].

EBM differs from other PBF techniques in several ways. SLS is the most similar PBF technique to EBM. Even with the similarities, there are many engineering tradeoffs between these two techniques. The primary difference between EBM and SLS, is the thermal source used in the melting process. The build chambers also differ, EBM operates in a vacuum whereas during SLS, the build chamber is filled with inert gas. Both methods employ a pre-heating phase prior to the fusion process. In EBM, the electron beam is used to preheat the powder in contrast, SLS requires the use of infrared heaters for this step. EBM is able to produce end items more quickly. This is due to the electrically driven scans of EBM as opposed to SLS's galvanometers which drive focusing mirrors. EBM does have the drawback of only processing conductive materials, where SLS is used with ceramics, polymers, and metals. Conversely electron beam generation is a more energy efficient process compared with laser beam generation. In SLS only 10%-20% of the input electrical energy is converted into beam energy. Energy use in EBM is much more efficient, with minimal losses during the generation of the beam, allowing more efficient use of electricity. The inherent higher operating temperatures of EBM produce a contiguous grain pattern, similar to a cast material [14].

EBM has grown in popularity since its commercialization in 2001. The PBF technique behind EBM provides support of the component during manufacture. This support comes from the unmelted powder which remains on the build platform. Other, non-PBF, forms of AM require additional consideration to sacrificial supports designed into the 3-D model. These supports are then removed after manufacturing requiring time and wasting material. The reduced need for sacrificial supports has allowed EBM to become more popular in the aerospace and biomedical fields, where complex geometries sometimes include small passageways. In traditional subtractive manufacturing these passageways are impossible due to tooling constraints. EBM's flexibility and capability will likely ensure it as a manufacturing technique widely used throughout multiple industries [14].

2.4 Titanium Alloy 6% Aluminum, 4% Vanadium - Ti-6Al-4V

Titanium is a relatively lightweight, structural material which is strengthened greatly through alloying and, in some cases, heat treatment. Titanium's greatest advantages are: high corrosion resistance, good strength-to-weight ratio, low density, low coefficient of thermal expansion, high fracture toughness, and low heat treating temperatures [22]. Material properties of titanium and its alloys are controlled by alloy content and the heat treatment process. Significant creep in certain alloys of titanium can occur at stresses as low as 0.5 F_{ty} (force of yield in tension) at room temperature. Titanium alloys are also susceptible to stress corrosion cracking in the presence of certain chemicals, including dry sodium chloride and methyl alcohol. Despite these limitations, titanium alloys are versatile structural materials [22].

Ti-6Al-4V was developed in 1950 at the Illinois Institute of Technology. It is an alpha-beta titanium alloy, containing both alpha and beta phases at room temperature [18, 22]. The alpha phase is similar to unalloyed titanium. However through the addition of alpha elements in the form of aluminum, the alloy is strengthened. The beta phase is the high temperature phase of titanium, this is stabilized at room temperature by the addition of beta stabilizing elements, usually vanadium, molybdenum or iron. When pure titanium is alloyed with 6% aluminum and 4% vanadium the resulting alloy is referred to as grade 5 titanium or Ti-6Al-4V. This specific alloy is widely used and available in many mill forms including bars, sheets, and blocks, as well as powder for casting [22]. Powdered Ti-6Al-4V is used in the EBM process as well and is the focus of this research.

Titanium alloys were first developed for and studied by the aerospace industry. Many applications in other industries were found requiring the high performance of this material. These applications include power generation plants, automotive, naval, and petroleum production. The aerospace industry still consumes about 70% of the world's titanium production. Common uses in aerospace for titanium include engine components such as casings, compressor blades, and rotors. Non industrial applications of titanium alloys include biomedical and sports equipment manufacturing where light weight and high strength products are desired. Titanium is not considered a rare metal, however the high cost of processing has limited its application to selected industries and applications. Ti-6Al-4V is the most common alloy of titanium, constituting 50% to 70% of the world's titanium output [18].

The EBM process is complex and depends on system processing parameters. These parameters range from beam size, to scan speed, and most importantly beam power [18]. Microstructure is important in determining mechanical properties such as strength, creep and fracture toughness of an alloy. Microstructure of Ti-6Al-4V depends on chemical composition, processing method, and heat treatment [23]. Cooling rates during and following manufacture determine grain size while cooling rate and thermal gradient determine grain morphology. Alpha grain size is an important issue as it controls many of a material's mechanical properties [24]. The final microstructure of Ti-6Al-4V samples built using the EBM process is a result of the combination of input control parameters. The microstructure has shown to vary as the process parameters are adjusted. Previous research has hypothesized this difference is due to the changes in build environments and cooling conditions due to changes in the build parameters [18]. When titanium alloys are used in AM, solidification conditions often lead to a coarse columnar beta grain structure [25]. The columnar beta structure aligns with the build direction, which is attributed to heat flowing downward into the build plate. Theoretically, growth should follow the maximum thermal gradient at the solidification front which is normal to the curved melt pool surface. Grain boundaries tended to slightly slope toward the direction of beam travel [23]. Extensive research accomplished by academia as well as industry into the unique microstructure of AM Ti-6Al-4V is ongoing. The flexibility of Ti-6Al-4V, coupled with the design freedom afforded by AM, makes this alloy an ideal match for aerospace applications.

2.5 Nondestructive Inspection

The goal behind NDI is to detect flaws or defects within a component. Once flaws are detected, additional information such as size, location, shape, or orientation is collected depending on the inspection method [26]. Ultimately, these inspections are conducted in a manner not impairing the future use of the part. NDI is used to detect subsurface flaws, measure geometry, or determine composition [27]. The five standard types of NDI used in the United States Air Force, are Liquid Penetrant, Magnetic Particle, Eddy Current, Radiography, and Ultrasonic [13]. The NDI method focused on in this research is the ultrasonic inspection.

NDI methods are an accurate way of detecting flaws when properly used by a well-trained technician. The information provided by NDI allows engineers and maintenance personnel to make actionable decisions about the serviceability of a component. Even with the accuracy of current NDI systems, confirmation of defects using another NDI method is often required [13]. The confidence in a certain NDI method is what drives the requirement for additional inspection techniques. The accuracy of a specific NDI method is also considered when designing critical parts or planning inspection intervals.

Several stages of inspections exist in the acquisition of components, including first article inspection, receiving inspection, manufacturing and assembly inspection, data gathering, vendor qualification, and capability demonstration. First article inspection is accomplished as part of a manufacturer's qualification and is intended to ensure the component meets the applicable engineering requirements. Receiving inspections are

conducted to ensure incoming materials, parts, or assemblies meet outlined requirements. Manufacturing and assembly inspections are performed prior to operations in the manufacturing process, making it impossible to inspect the component. Vendor qualification is ultimately an audit of manufacturers and suppliers, ensuring the vendor's NDI procedures meet qualification requirements [27].

Within the realm of sustainment, NDI is used to insure the safety of structural components throughout the lifecycle of the system. This is accomplished through initial and recurring inspection [27]. Periodic recurring inspections using NDI feed data to specific structural integrity programs for a given weapon system. These programs outline mission requirements, design requirements, operational assumptions, inspection areas, inspection methods, and critical crack criteria. A key tool used in this determination is a durability and damage tolerance assessment. This assessment uses established models to predict crack growth from an assumed initial size to a critical size. The time required for this critical crack growth drives inspection intervals, usually in the span of two inspection cycles under normal operating conditions. Probability of detection studies provide an estimated minimum defect size a technician can find with a certain confidence. Often, probability of detect studies are used to determine the initial assumed flaw size. An example of a probability of detect plot is shown in Figure 2 [28]. Aircraft engineers use a variety of tools in the sustainment of fielded systems. NDI, as one of these tools, plays an important role in the detection of subsurface cracks before they reach the critical size [13].

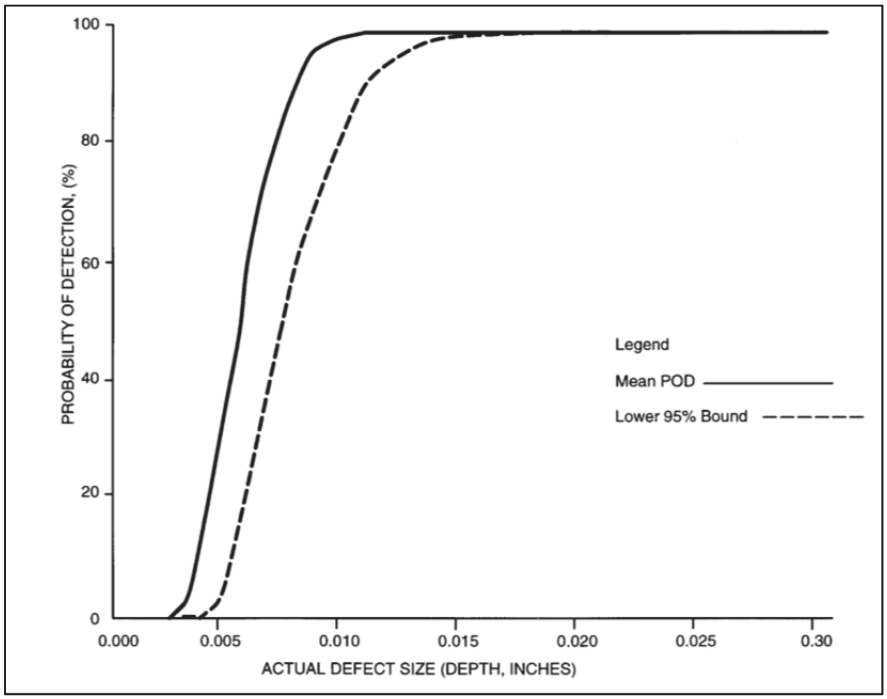

Figure 2. Example of NDI standard probability of detect curve [28]

The DOD's guidance in MIL-HDBK-6870 is to provide NDI capabilities demonstration when new material or manufacturing technique is developed [27]. Currently additive manufacturing falls into the category of a new manufacturing technique. The rapid advancement and shifts in AM have led to hesitation in exploring NDI techniques [10]. However, NDI's versatility has the potential to increase the confidence in AM's production and use. This confidence can lead to broader and more effective use of AM throughout multiple industries. The use of AM has grown despite a number of challenges continuing to impede its more widespread adoption, particularly in the areas of measurement and standardization. AM is currently a high-priority growth area for manufacturers [11]. NDI will play an essential role in the verification of AM hardware and parts [10].

2.6 Ultrasonic Inspection

Ultrasonic inspections employ high-frequency mechanical waves to detect various material variables [29]. Ultrasonic waves provide deep, internal inspection capabilities. Normally, ultrasonics provide the deepest penetration for inspection, depth is often measured in feet as opposed to other methods where penetration is measured in inches [29]. UT does not require the intrusion of foreign substances into a material to facilitate inspection, such as those associated with liquid penetrant or magnetic particle inspections, but consists of movement of the internal atoms which comprise the test sample. This leads to UT remaining among the safest of all inspection methods. The flexibility of UT allows its use on a large variety of materials; this method does not require a material which is magnetic, or electrically conductive as with other methods. UT is used on any material exhibiting volumetric elasticity. UT's flexibility can detect a variety of variables in materials. These variables include flaws, voids, inclusions, disbond, material thickness and density [29].

UT relies on the generation of high frequency mechanical waves directed into a specimen [29]. The ultrasonic range refers to sound waves with a frequency of 20,000 Hz or more. For use in NDI, this high frequency sound wave is generated by a transducer [13]. Just as with audible sound, ultrasound is characterized by periodic molecular vibrations. The vibration propagates at a standard velocity for each material. Each particle is displaced from its neutral point to a maximum distance then reverses direction and translates to a negative maximum. The particle will continue to the neutral point completing one cycle. Each particle subjected to the mechanical wave continues the

cyclic movement until the source of the wave is removed. The amplitude of vibrations in the samples are low enough to cause no permanent deformation in any characteristic of the sample [13]. The amount of time it takes for a particle to complete one cycle is called the period of the wave. Frequency of the wave is the number of cycles the wave completes in one second, measured in hertz. The distance the wave travels in one cycle is referred to as wavelength, and is calculated in Equation 1 below.

$$\lambda = \frac{v}{f} \tag{1}$$

Where λ is the wavelength, ν is the velocity of the wave through a specified medium and f is the wave's frequency.

Four basic types of waves are used in ultrasonics: compression, shear, surface and lamb waves. Compression waves cause motion in the sample's particles in the same direction as the wave propagation, as shown in Figure 3. Compression waves are the fastest wave in terms of traveling through a material and are useable in all forms of materials. This is why it was chosen in this work as the method of inspection. Shear waves move at a slower velocity and cause relative displacement of particles perpendicular to the wave propagation. To use shear waves, assumptions about specimen dimensions and surface effects are made. Surface waves are a combination of shear and compression waves causing an elliptical motion in particles. Energy from a surface wave dissipates quickly through the depth of a material, restricting the use of surface waves to shallow defects. Lamb waves are limited to materials which are very thin, on the order of 1-2 wavelengths thick [29].

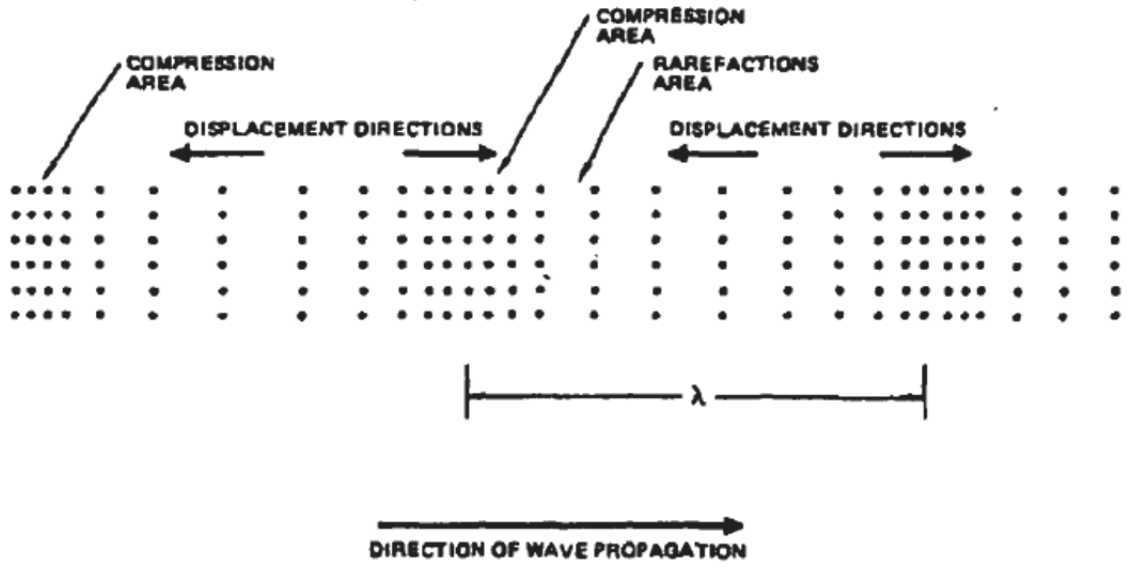

Figure 3. Compression Wave Motion [13]

High frequency ultrasonic beams are generated by transforming electrical energy into mechanical waves using a piezoelectric element. This applied energy produces a sudden high energy spike to the transducer element, transforming the electrical energy into mechanical vibration at a frequency determined by the specific transducer used. The material and thickness of the piezoelectric element determines the frequency produced by each transducer. The element is also designed to receive ultrasonic energy and transform it back into electrical energy. Air has high acoustic impedance, therefore making it a poor transmitter of sound waves [13]. To maintain the energy of ultrasonic waves, a coupling medium is used between the transducer and the sample. The coupling material is used to eliminate air between the transducer and the sample [13, 29]. This coupling agent is usually oil or water [13].

Ultrasonic beams do not propagate uniformly from the face of a transducer. Energy is distributed across the width of the beam with the highest energy at the center

and decreases radially outward. The ultrasonic energy produced by the transducer is varies in intensity in a region from the face of the transducer to a finite distance. This distance is known as the near-field zone. In this region the beam is affected by waves generated from the edge of the transducer, therefore inspections within this zone are not recommended [13]. The length of the near-field is approximated using Equation 2, seen below. Where N_f is the size of the near-field, D_t is the diameter of the transducer, and λ represents the wavelength. Any point beyond the limit of the near-field is referred to as the far-field [29].

$$N_f \approx \frac{D_t^2}{4\lambda} \tag{2}$$

When the ultrasonic wave leaves the transducer and enters a medium, either the sample or a couplant, the wave imparts energy on the atoms of the medium. In a sample under UT atoms are held in equilibrium by the attraction and repulsion to other atoms comprising the material. When the ultrasonic wave transfers energy to the first atom it encounters the atom is displaced elastically. The displacement of an atom causes a change in force balance with surrounding atoms. The inertia of surrounding atoms results in a finite time for a response to the imbalance by the atoms whose forces act on the subject atom. This response creates a wavelike action through the material. A wave's velocity through a material, V_L, is governed by the mechanical properties of the material such as: modulus of elasticity (E), density (ρ), and poisson's ratio (ν). For an isotropic material of sufficient thickness the velocity is estimated using Equation 3, below [29].

$$V_L = \sqrt{\frac{E(1-\nu)}{\rho(1+\nu)(1-2\nu)}} \tag{3}$$

As an ultrasonic wave transmits through a material several types of interaction can occur including, diffraction, scattering, absorption, reflection and refraction. Reflection is a key component to UT, as the wave propagates from atom to atom areas of discontinuity cause the interaction between atoms to change. This variation leads to the energy of the wave dispersing, a portion of the wave is reflected in the direction of the transducer. When the wave reached the transducer the return is captured as an indication based on the intensity of the energy associated with the returning wave. Transducers used in UT fall into two categories based on the beam produced. The first of these is an unfocused beam resulting in a divergence of the beam. The second is a focused beam, used on immersion inspections [13, 29]. Focused beam transducers cause the beam to either spread out or become focused at a certain distance from the face of the transducer [13]. Both can produce desirable and undesirable results during an inspection. A focused beam can provide greater resolution at a fixed distance away from the face of the transducer. This requires knowledge of the flaw under inspection or multiple inspections at varying depths to provide the best result.

An unfocused beam dissipates in intensity once the far-field is reached. This can cause issues in thicker samples as the far-field is where the majority of inspections are required [13]. The intensity drop off is an exponential decay once the far-field is reached. In the near-field the beam propagates straight from the face of the transducer. Once the far-field is reached the beam spreads out at a rate shown in Equation 4; where θ is the half angle of spread, λ represents the wavelength, and D is the diameter of the transducer face. This represents the half angle of the cone produced by the primary beam

of energy as seen in Figure 4. Understanding beam spread is important as the sound beam may reflect off walls causing a false signal [13].

$$\theta = sin^{-1}\left(\frac{1.22\lambda}{D}\right) \tag{4}$$

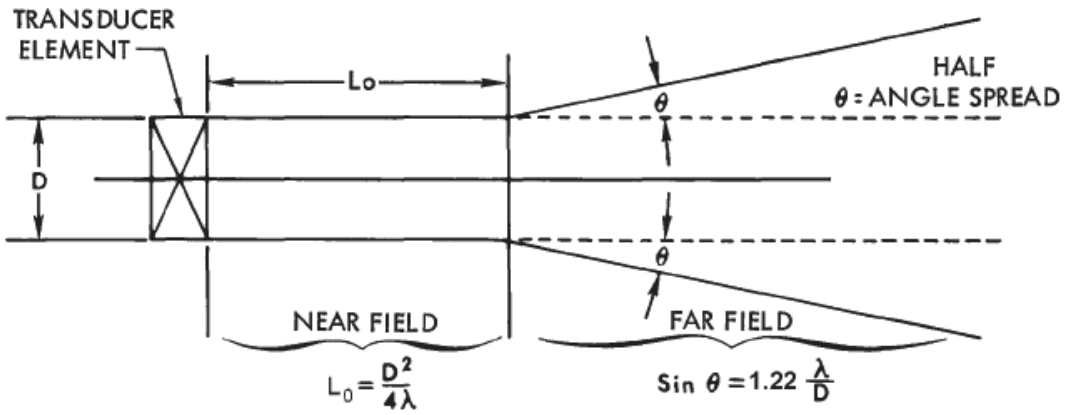

Figure 4. Example of ultrasonic beam dispersion from transducer face including near field, far field, and beam spread angle [13]

Focused beams are created by utilizing a plastic acoustic lens on the face of the transducer. This lens causes sound to converge as it extends beyond the face of the transducer. Due to the refraction at the plastic-water interface, the beam will converge to a desired focal point as seen in Figure 5. This focal point is a constant and is set for each transducer. The distance of this focal point is measured as the distance from the face of the transducer to the focal point using water as a couplant. During an inspection, when the beam is penetrating a sample, the beam refracts at a higher level in the test material than in water, causing the focal point to shift closer to the face of the transducer as seen in Figure 5. The change in focal point in the material is a function of acoustic impedance of the material. Acoustic impedance is calculated using Equation 5; where Z is the

acoustic impedance of a material with units of kg/m^2-sec, ρ is defined as material density in units of kg/m^3, and ν represents the velocity of sound in the material in units of m/sec. Focused transducers have a high sensitivity at the focal point allowing for greater resolution at the specified depth in the sample [13].

$$Z = pv \tag{5}$$

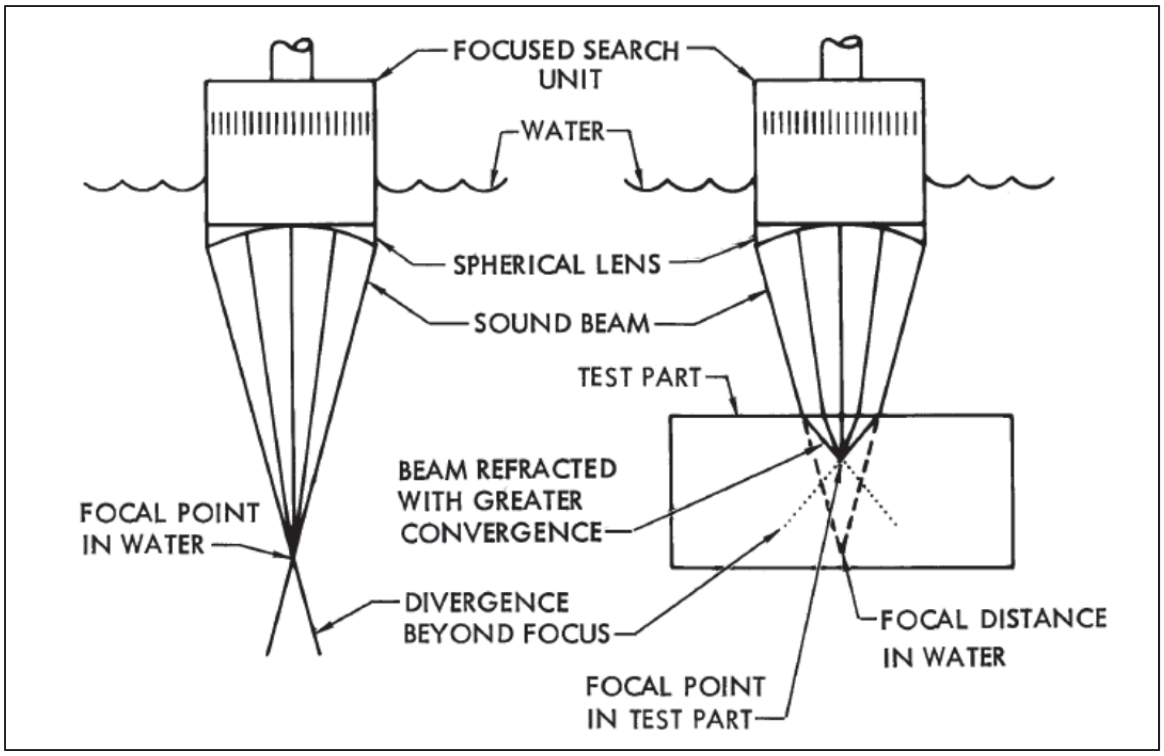

Figure 5. Example of focused ultrasonic beam focal distance change and divergence in water and test specimen [13]

As the transducer sends sound waves, it also receives echoes between the pulses. These echoes are displayed as the amplitude of the return at the distance from the transducer as a function of time producing what is referred to as an "A-scan" as shown in Figure 6 [29]. The first indication in this scan at the front face of the sample is denoted by (1). The middle indication, or (2) is the result of a flaw in the center of the sample,

and the final indication, denoted as (3), is the back wall of the sample. This is also represented in Figure 7 showing a discontinuity and the corresponding indication. If using a computerized controller to move the transducer over the sample, multiple A-scans are compiled into a "B-scan". B-scans provide a cross-sectional representation of the sample. Figure 8 shows an example of a B-scan where the white horizontal line corresponds to the A-scan in Figure 6. A-scans are also electronically gated to produce a "C-scan". C-scans are planar views of the gated region of the A-scans. Figure 9 shows a C-scan as a planar image where the amplitude of the return is shown in 256 greyscale with black as zero and white as 255. C-scans are very useful as they present a large amount of information in one image. This is described in greater detail in later sections.

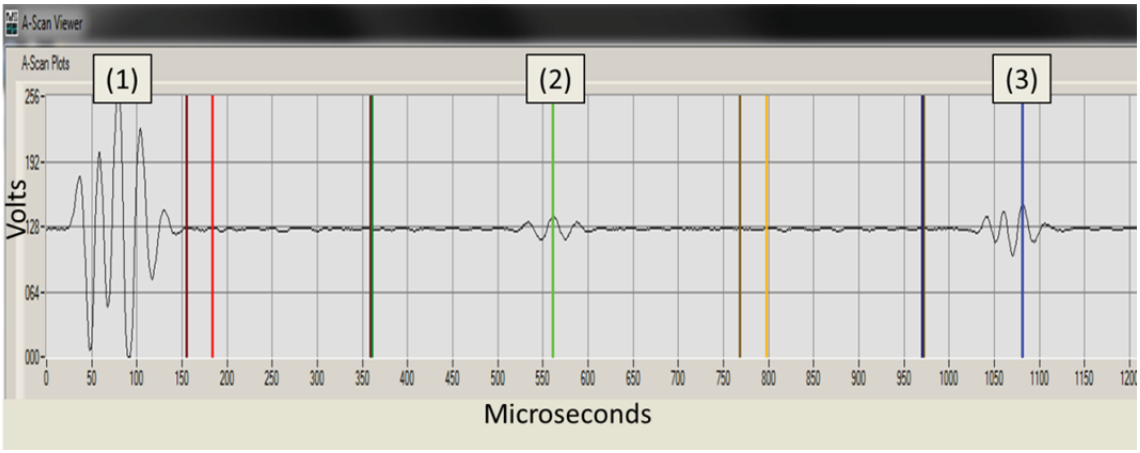

Figure 6. Example of ultrasonic A-Scan through top surface, (1) signal return of top surface, (2) flaw indication, (3) signal return of back surface

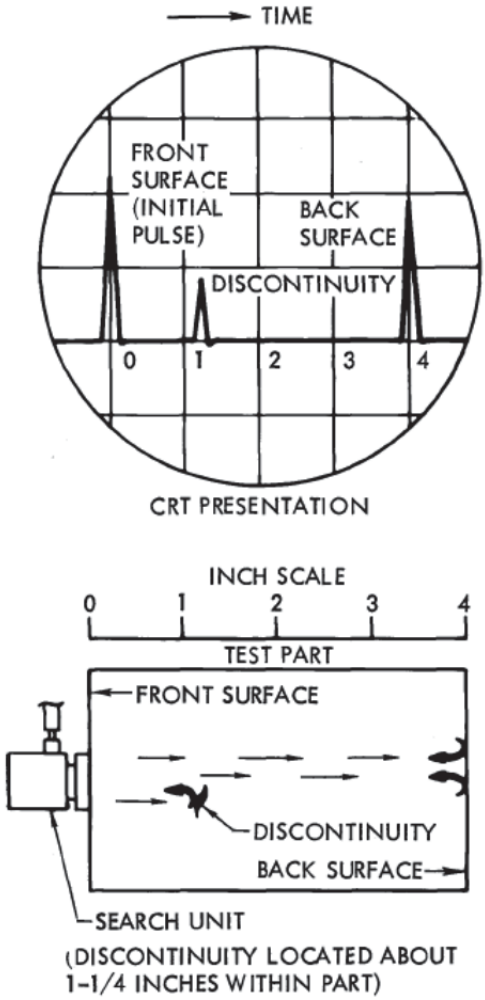

Figure 7. Example of A-Scan indication of imbedded flaw in sample [13]

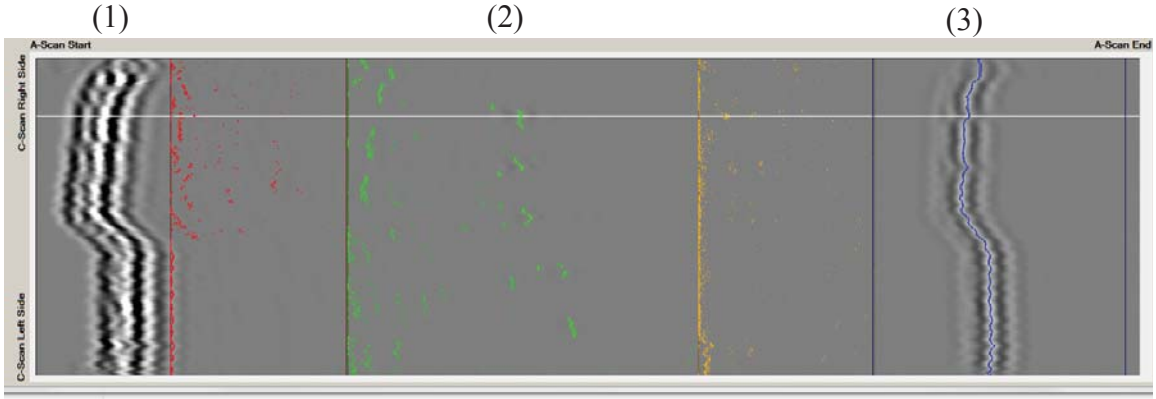

Figure 8. Example of ultrasonic B-Scan scan through top surface (1) signal return of top surface, (2) flaw indication, (3) signal return of back surface

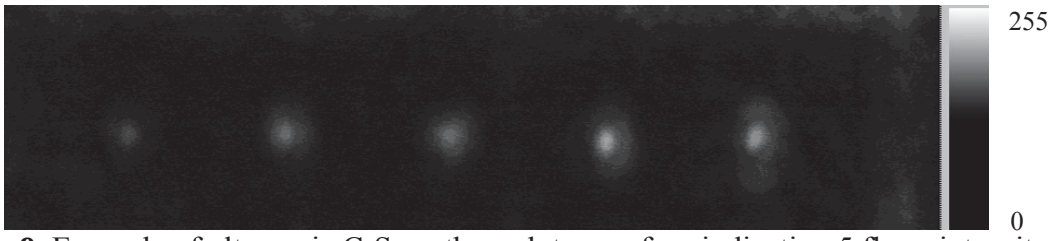

Figure 9. Example of ultrasonic C-Scan through top surface indication 5 flaws intensity of return on 256 greyscale

2.7 Previous Research

Government, academia, as well as private industry have acknowledged the need for NDI of AM [10, 11]. NDI was identified as the preferred method of testing and quality assurance by the National Institute of Standards and Technology (NIST). In-process inspections are desired as a method of providing feedback to machine controls, improving reliability and overall quality of output [11]. While in-process inspections provide for better closed loop feedback, current NDI methods are better suited for post manufacturing inspections.

Current work is underway by various agencies to assess NDI's use on AM materials. The NIST is assessing state of the art methods for testing raw metal powders, as well as non-destructively testing completed components. The focus of the NIST's research is Direct Metal Laser Sintering (DMLS) as opposed to the research in this thesis which focuses on EBM samples [11]. The NIST has listed in-situ monitoring as a higher priority than post manufacturing NDI. The need is identified in the NIST's action plan to build a repository of NDI process parameters and controls. The focus of these

inspections is to enable the validation of process performance, and ultimately parts qualification [11].

NASA has begun exploring the use of Electron Beam Freeform Fabrication (EBF3) to manufacture high thrust engine components. EBF3 is not a PBF technique, but uses a wire feed into an electron beam to build components [30]. This process is more closely related to welding than it is to EBM, see Figure 10. The benefit of this process to NASA is its potential used in a zero gravity situation where a PBF technique is not practical. NASA has explored NDI of EBF3 as well, to include x-ray, CT, eddy current, and ultrasonic inspections. Efforts in the field of NDI's use on EBF3 have focused on the use of infrared in situ inspections to monitor the melt pool temperatures for variations [10].

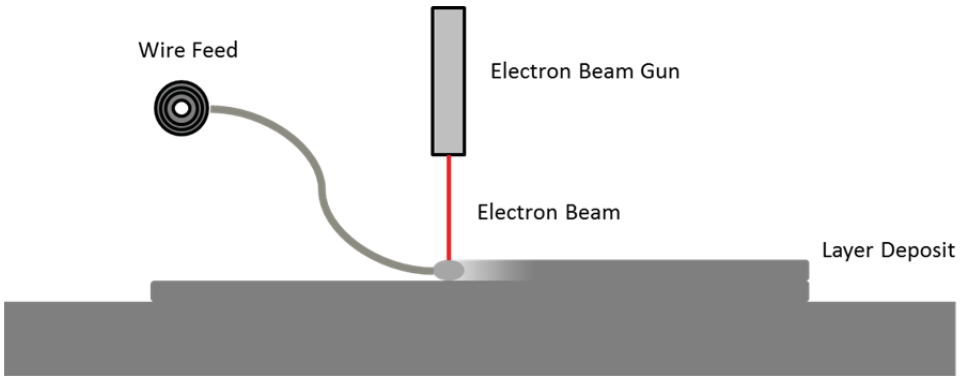

Figure 10. Illustration of Electron Beam Freeform Fabrication (EBF3) Process [30]

NASA's Glenn Research Center is exploring the use of EBM in the manufacture of gaseous hydrogen/liquid oxygen injectors. These injectors are made from Inconel, which is a high temperature, nickel-based alloy [10, 22]. NDI is used in the material characterization of these components. The NDI methods used are CT, ultrasonic, and on machined surfaces liquid penetrant [10].

Research conducted by AFRL in 2006 on early laser based Ti-6Al-4V AM processes used UT to determine lack of fusion defects. The process used to manufacture the samples in this research was called laser additive manufacturing. (LAM). This process is no longer used and AeroMet, the company that developed it, is no longer in business, but valuable lessons were learned from this technique. LAM used a CO_2 laser in conjunction with a nozzle sprayed titanium powder to produce layered products. Many of the technical gaps in the LAM process were addressed and improvements were made as this technology developed into SLS and EBM, which is utilized today. UT was shown extremely effective in the detection of lack of fusion defects. It was noted that the size of the actual flaw was over-estimated using UT of LAM [31].

III. Methodology

The methods used to conduct research for this thesis are detailed in the following chapter. Various inspection techniques were investigated during the preliminary research phase, several of these were later deemed impractical. The resulting procedures are intended to produce the most accurate and reproducible outcomes. Where available, established standards and industry "best practices" were used in order to align this research with other publications. In as many areas as possible human interpretation was replaced with a computer based algorithm or technique; this is intended to remove a potential source of contention.

3.1 Applicable Standards and Guidance

In 2014 ASTM released a standard for the use of powder bed fusion AM of Ti-6Al-4V. ASTM has designated standard F2924-14 to addresses quality, inspection, terminology, manufacturing, processing, mechanical properties, and other requirements [32]. F2924-14 is referenced for terminology as well as specifications. ASTM's 2011 standard E1001 – 11 covers immersed pulse-echo ultrasonic method using longitudinal waves, this standard is referenced for setup of testing procedures as well as techniques and terminology [33]. The Air Force's technical order 33B-1-1 "Nondestructive Inspection Methods, Basic Theory" was also used for setup and data collection during the experimentation.

The coordinate system is defined using ASTM F2921-11, which is also used for terminology and build orientation. The coordinate system is based on initial sample build orientation using orthogonal notation with respect to the build chamber. The ASTM

F2921–11 orthogonal orientation coordinate system is shown below in Figure 11. From Figure 11, the positive Z-axis is normal to the layers added by the build process. The positive X-axis is perpendicular to the Z-axis and parallel to the front, as viewed by the operator, of the machine and the Y-axis is the remaining orthogonal direction. The origin of the coordinate system (0,0,0) is defined by the geometric center of the build plate surface and positive X, Y, and Z directions are as shown in Figure 11.

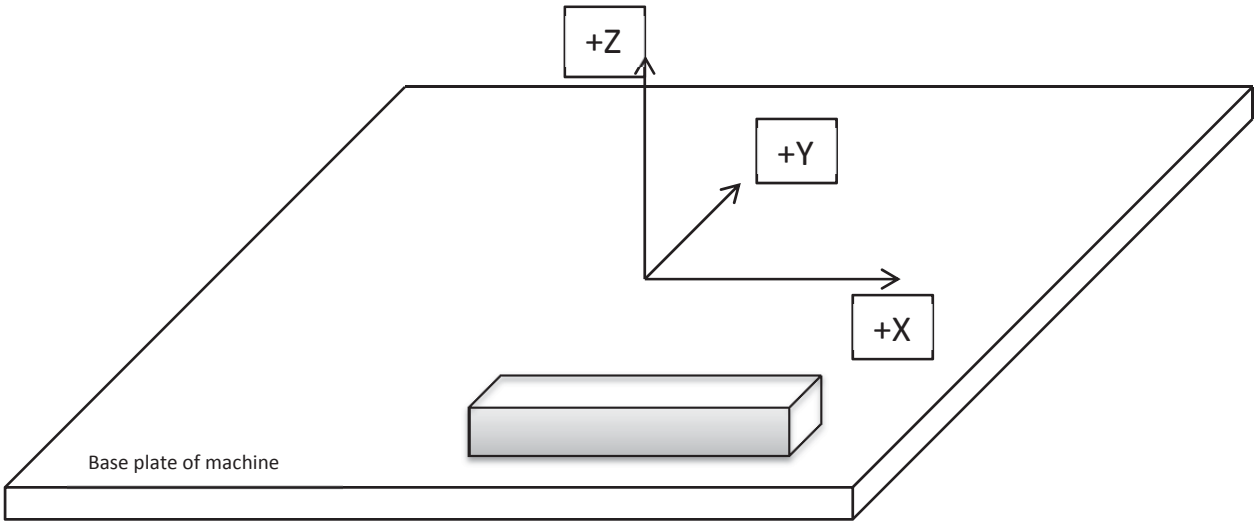

Figure 11. Illustration of build orientation axis

Following the standard sign convention in ASTM F2921-11, a part on the build plate is aligned to the XYZ axes, it is described with a 3-axis designation. The first letter of the designation corresponds to the axis parallel to the longest dimension of the part, the second letter corresponds to the axis parallel to the second longest dimension, and the third letter corresponds to the axis parallel to the shortest dimension. For the sample part shown in Figure 11, the build orientation is described as XZY or XYZ since the Y and Z lengths are the same. The relative position of the part on the build plate is expressed as a

three-dimensional location of the sample's centroid with respect to the origin of the machine's base plate [33].

3.2 Test Specimen Design

The specimens used in this testing were designed by the Structural Materials Division of the Air Force Research Laboratory (AFRL) for the purpose of testing nondestructive as well as destructive inspection techniques. The samples were designed as rectangular blocks 25.4mm wide (Y), 25.4mm tall (Z), and 114.3mm long (X) represented in Figure 12. Specimens were designed and built as sets of two exactly similar samples in each production run. Each block was designed with five embedded spherical flaws ranging in size from 0.51mm to 2.54mm in diameter as listed in Table 1. These flaws were designed on the center line of the sample with the center of the spheres evenly spaced in ascending diameter as shown in Figure 13.

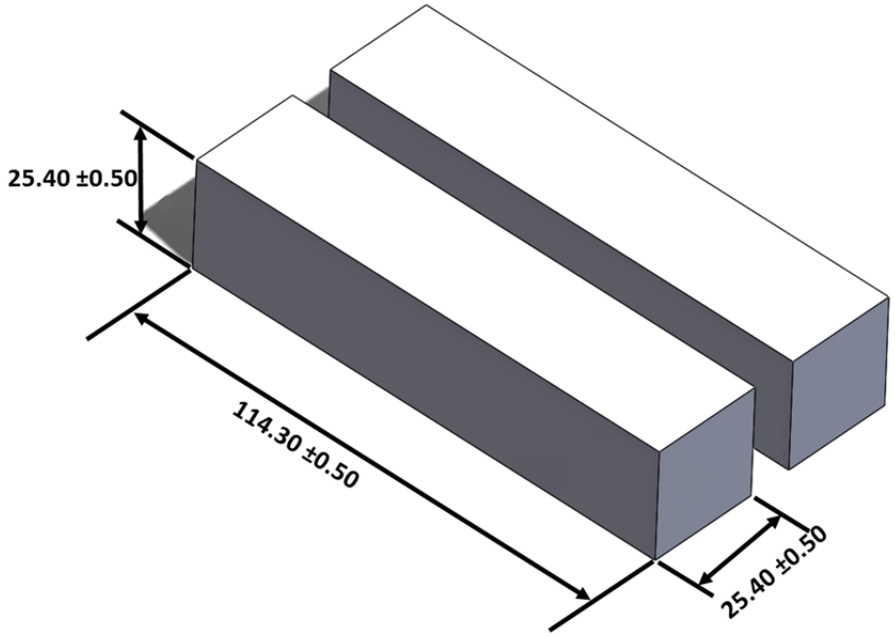

Figure 12. Design of samples, dimensions in mm

Table 1. Sample designed flaw dimensions

Flaw	Diameter (mm)	Diameter (in)
1	2.54	0.100
2	2.03	0.080
3	1.52	0.060
4	1.02	0.040
5	0.51	0.020

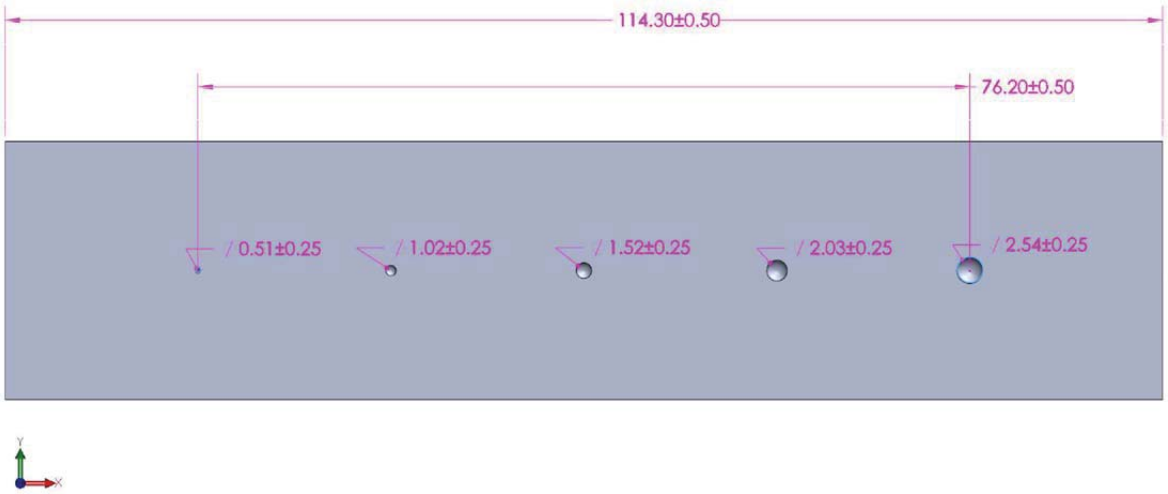

Figure 13. CAD design of samples to include defects with dimensions in mm

Experimental samples were designed using SolidWorks to create a 3D CAD model. The model was processed to create an STL file, which was then converted to an ABF file. The ABF file contains all data which is needed for the system to manufacture each 2D layer comprising the entire part. These 2D layers are stacked in the +Z direction on the build bed of the machine to create the 3D samples. The layered manufacturing process results in the final melted layer as the upper surface, normal to the +Z axis.

During a manufacturing production run, build time is important to resource management. The creation of multiple samples in one build is done in less time than multiple samples individually. To maximize efficient use of manufacturing time other

samples not used in this research were also designed and built in each production run. A representation of the entire production run is seen in Figure 14. The samples not used in UT are used for CT experimentation and other future NDI testing by AFRL.

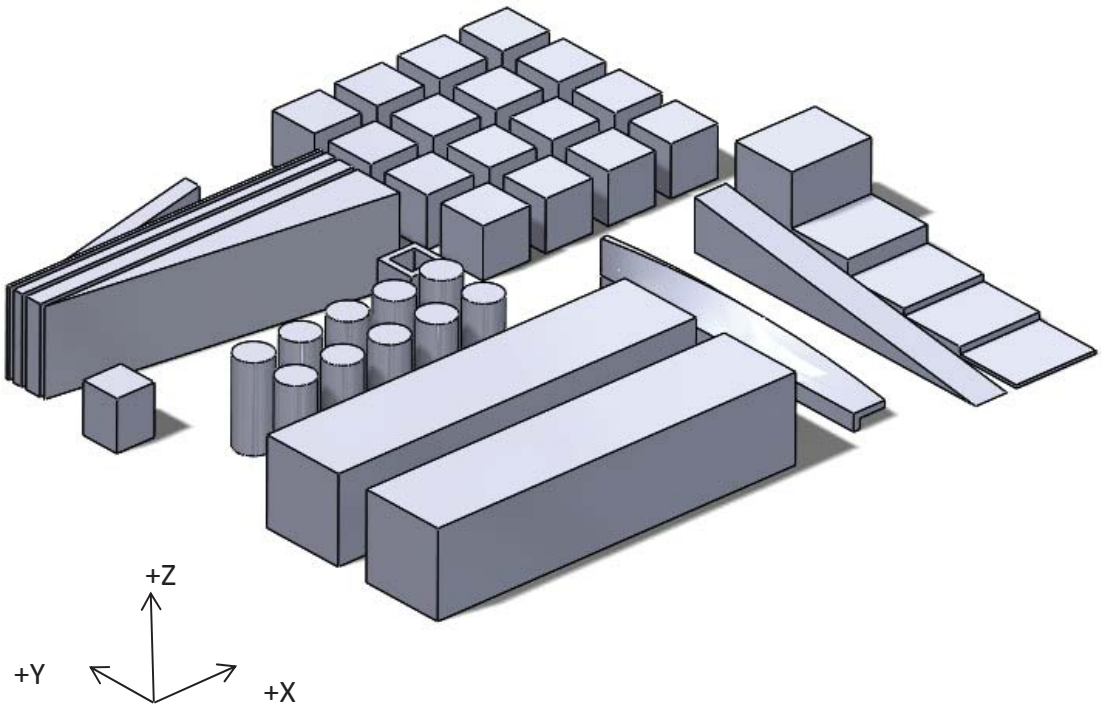

Figure 14. Manufacturing run including ultrasonic samples and additional samples for alternative NDI testing for other studies [12]

3.3 Test Specimen Manufacturing

Samples for this research were manufactured at Oak Ridge National Laboratories in Oak Ridge, TN as part of a joint project with AFRL. A total of twelve samples were manufactured and used to collect the data in this research. These samples were produced as six sets of two. Each production run was given an alphabetic designation. Production runs A, B, D, E, L and M were used to collect the data presented in later chapters. Samples A thru E were manufactured using Arcam's A2 system while samples L and M

were manufactured on Arcam's newer Q10 system. All samples were manufactured with the X-axis of the sample parallel to the X-axis of the AM machine's power bed. The A2 system has a larger build envelope while the Q10 has a smaller height of build envelope as seen in Table 2.

Figure 15. Arcam A2 system [20]

Figure 16. Arcam Q10 System [34]

Table 2. Build dimensions of Arcam systems [34, 20]

System	Width (mm)	Depth (mm)	Height (mm)
A2	200	200	350
Q10	200	200	180

Samples A and B were manufactured using recycled powder from previous builds. Recycled powder is the recovered powder from areas of the build envelope not subjected to the electron beam during the manufacturing process. Recovered powder represents material which in traditional subtractive manufacturing is discarded as waste

or recycled and through extensive processing turned back into usable material. The remaining samples were manufactured using virgin material from one of two powder lots. Table 3 shows the data for the powder used to manufacture samples.

Table 3. Build information for all samples

Sample	Machine	Powder Lot	Recycled
A-41	Arcam A2	P841	Yes
A-42	Arcam A2	P841	Yes
B-41	Arcam A2	P841	Yes
B-42	Arcam A2	P841	Yes
D-41	Arcam A2	P860	No
D-42	Arcam A2	P860	No
E-41	Arcam A2	P860	No
E-42	Arcam A2	P860	No
L-41	Arcam Q10	P866	No
L-42	Arcam Q10	P866	No
M-41	Arcam Q10	P866	No
M-42	Arcam Q10	P866	No

3.4 Surface Roughness Measurement

After each set of samples was manufactured, the excess unmelted powder was removed in a recovery area. Once the loose powder was recovered, the samples were removed from the build plate. The build process resulted in a relatively smooth bottom and top surface and much rougher surfaces normal to the X-Z plane. Measurements were performed using a Taylor-Hobson Form Talysurf model 120 surface profilometer as seen in Figure 17. A representative area of each sample was evaluated on both the upper and side surfaces. The measurement area was 10 mm long and 10 mm wide of the 114.3 mm long, 25.4 mm wide surface. The profilometer took 10 successive linear measurements, spaced 1mm apart, as shown in Figure 22. Each linear measurement was 10 mm long

following a 0.25 mm run-up. The linear measurements collected 100 data points per line, giving a total of 1000 points in which to calculate surface roughness. These data points were used in Equation 6 to calculate the root mean square (RMS) of the surface roughness. RMS was chosen over other industry standards as it accounts for the entire surface as opposed to only peaks and valleys.

$$R_q = \sqrt{\frac{1}{n}\sum_{i=1}^{n} y_i^2} \tag{6}$$

Where y is the height of each point and n is the number of points sampled.

Figure 17. Profilometer set-up, used to generate 3-D surface roughness measurements

The Taylor-Hobson Form Talysurf 120 has a maximum range of 120 μm. Following multiple attempts to measure the side surface with this particular profilometer, the surface was determined as above the range of measurement. Alternate methods were explored and the method of measurement ultimately decided on was a 3D Measuring

Macroscope, shown in Figure 18. The 3D Measuring Macroscope provided similar results to the profilometer. The top surface of samples B-42 and M-42 were measured using both methods as a comparison. The resulting measurements of sample B-42 were 21.2 μm RMS using the profilometer and 20.25μm RMS with the Macroscope, providing approximately a 4% difference. Sample M-42 provided results of 15.8 μm RMS and 15.76 μm RMS, a difference of 0.2% between measurement methods. Due to resource constraints, only sample -42 from each set was measured for side surface roughness. It is assumed samples from the same production run, both sample -41 and -42, have the same side surface roughness. Figure 19 is a representative image taken with a scanning electron microscope of the side surface of a sample. Figure 19 shows the surface irregularity and several partially adhered grains using a scanning electron microscope.

Figure 18. 3-D Measuring macroscope, Keyence Model VR-3200

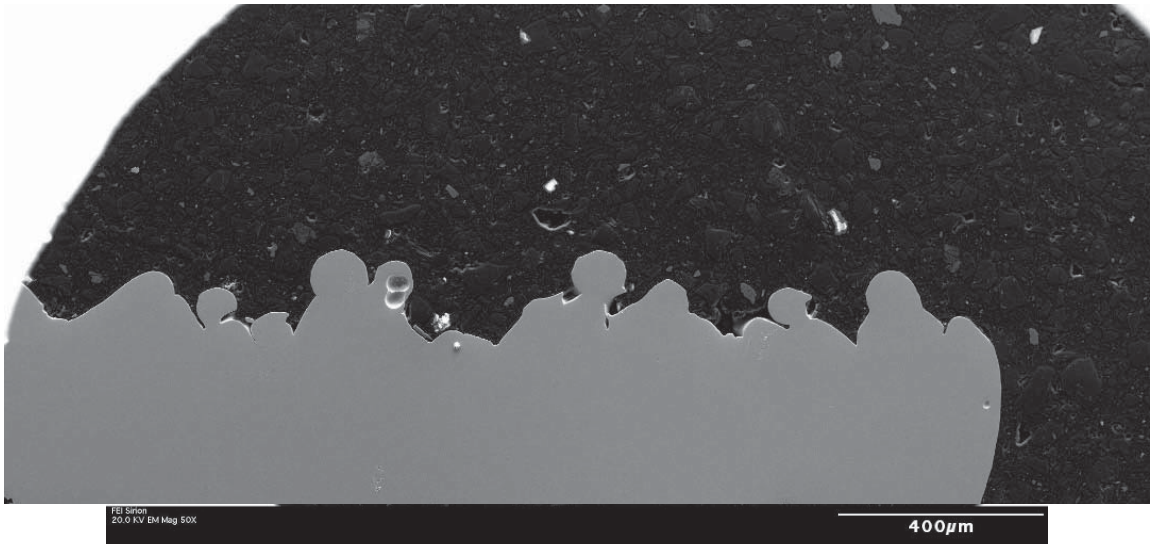

Figure 19. Example of SEM image illustration side surface roughness, Ti-6Al-4V samples in the X-Y plane [12]

3.5 As-Manufactured Surface Roughness Results

The roughness of the as-manufactured top surfaces of all samples is close in magnitude with a mean of 17.25 µm RMS and a standard deviation of 2.7 µm. For comparison, 220 grit sandpaper has a roughness of 18.5 µm RMS [35]. Figure 20 shows a 3D image of the profile of a representative 10 mm by 10 mm upper surface. The surface profile is also represented as a 2D image as shown in Figure 21. A linear breakout of this 2D image is given in Figure 22, the relative peaks and valleys become apparent in this linear representation. The results of all top surface roughness measurements were compiled and are given in Table 4, along with the measurements from the side surfaces.

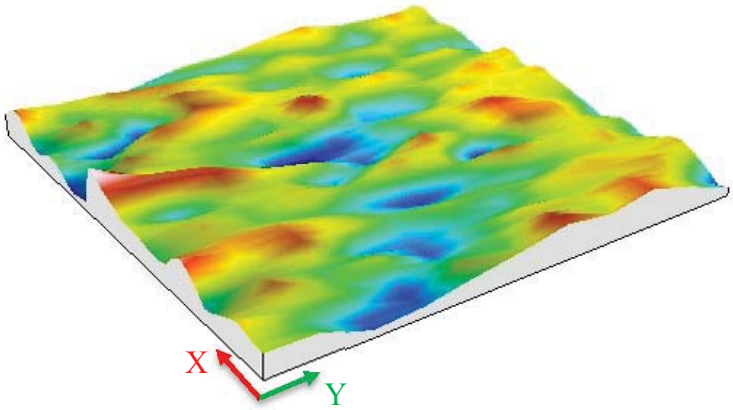

Figure 20. 3-D Surface map of sample A-41, top surface with roughness of 16.8 µm RMS

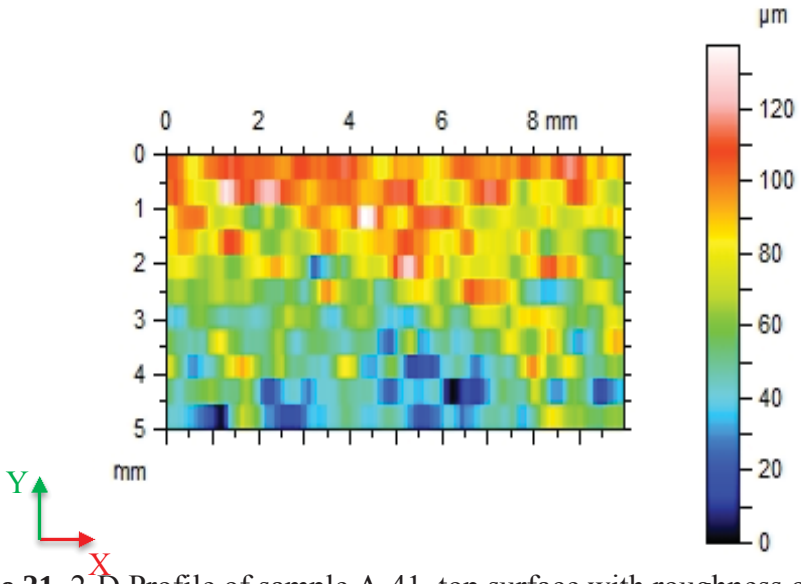

Figure 21. 2-D Profile of sample A-41, top surface with roughness of 16.8 µm RMS

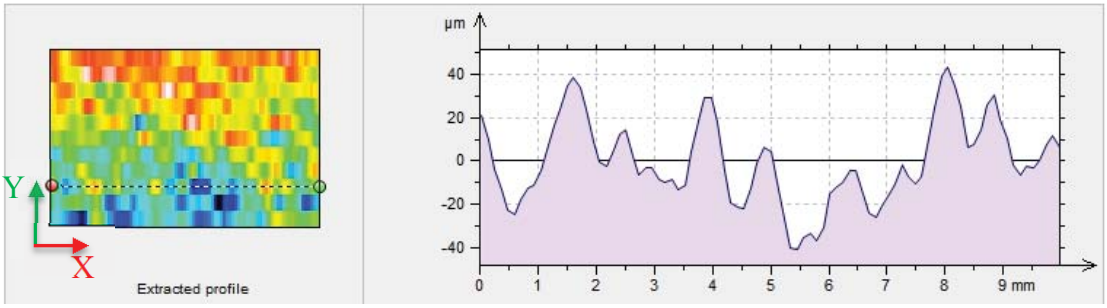

Figure 22. Linear profile of sample A-41, top surface in X-Z plane with roughness of 16.8 µm RMS

Table 4. Sample surface roughness measurements prior to machining

Sample	Top Surface (µm) RMS	Top Max Peak to Peak (µm)	Side Surface (µm) RMS	Side Max Peak to Peak (µm)
A-41	16.8	115.3		
A-42	16.1	102.6	45.14	307
B-41	22	103.8		
B-42	21.2	127	40.91	268.52
D-41	19.6	118.5		
D-42	18.8	118.7	58.7	439.12
E-41	16.2	83.6		
E-42	15.5	93.7	43.78	320.15
L-41	11.1	71.3		
L-42	16.5	101.7	25.46	202.82
M-41	18.3	88		
M-42	15.8	99.8	27.03	208.95

Side surfaces which were in the vertical orientation during the build, resulted in an increased surface roughness, in the range of 25-60µm RMS, which is comparable to 100 grit sandpaper [35]. The increased roughness is attributed to partially melted and adhered powder as seen in Figure 19. In some samples these powder particles led to an almost four times increase in measured surface roughness when compared to the top surface. Measurements of these faces are found in Table 4. In later sections, surface

roughness is examined to determine the degree in which surface finish affects the ability to detect known flaws at various frequencies.

3.6 Ultrasonic Inspection of As-Manufactured Samples

Ultrasonic inspections were completed on all 12 samples at 2.25MHz, 5MHz, and 10 MHz; both through the top and side surfaces. Focused beam transducers were selected for each of these frequencies. A focal length of 7.62 cm was available in each frequency. Focal length is the distance from the point in which the beam is concentrated to the face of the transducer, through a specific medium. The velocity of the longitudinal wave in water is 149,860 cm/sec, and 609,600 cm/sec in titanium, which causes the beam to focus to a point faster in titanium resulting in a shorter focal length, as seen in Figure 5 [13]. The samples under inspection are 2.54 cm in thickness with the flaws located on the centerline as described previously. Given the velocity of the wave in titanium is four times that of water, the equivalent focal length from the surface to the centerline of the sample is 5.08 cm. With a 7.62 cm focal length transducer placed 2.54 cm above a submerged sample the focal point is in the optimal position for the designed flaws.

The transducer was mounted to a three axis translational stage allowing full computer control of the transducer. As seen in Figure 23 the traverse is mounted over an immersion tank. It was discovered during the ultrasonic scanning process opposite sides are not perfectly parallel. A leveling plate was then used to ensure the surface was in a horizontal orientation during scanning. The Z-axis was set to focus the beam on the centerline of each sample and held constant throughout each scan. The primary scan axis was designated as the X-axis with A-scans collected at an interval of 0.06 mm, providing

a minimum of 10 points across the smallest known flaw. The secondary scan axis was the Y-axis with a 0.06 mm step size. Each set of scans resulted in 857,286 A-scans per sample. The raw output A-scans as in Figure 24, were gated in to produce C-scans of each sample. The middle 0.635 cm of each sample was isolated to provide a C-scan of the center region, as shown in Figure 25.

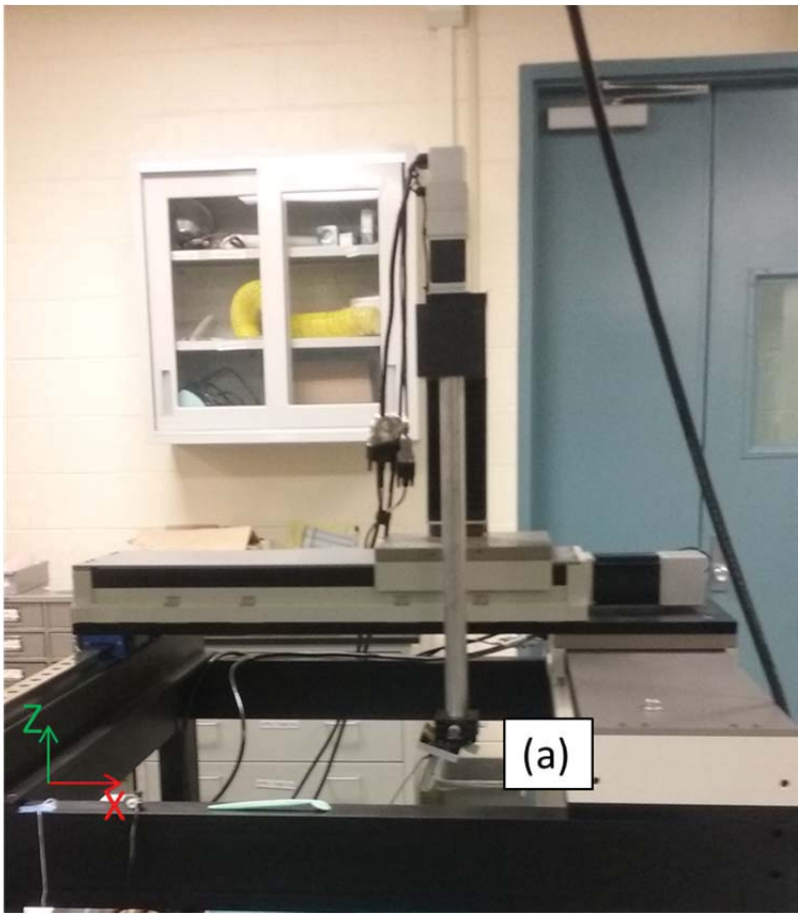

Figure 23. Traverse with transducer (a) installed, Immersion Tank Removed

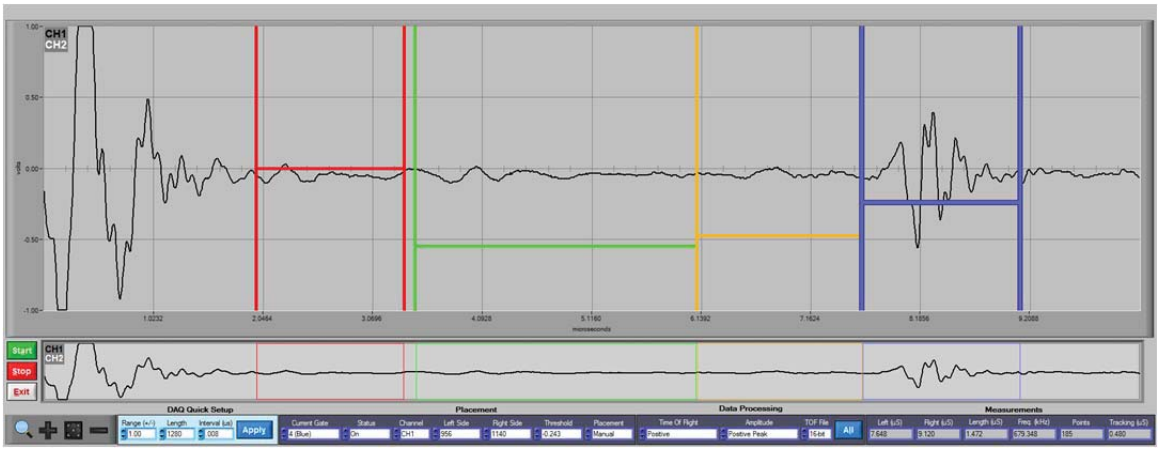

Figure 24. Example of A-scan through top surface, thickness of sample gated in three sections: red, green, and orange with back wall gated in blue.

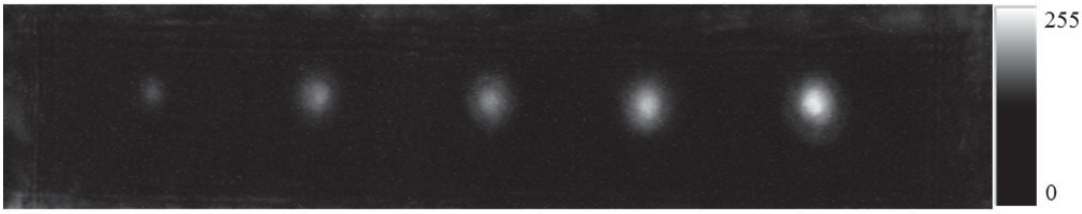

Figure 25. C-scan of middle 0.635 cm of sample through top surface corresponding to green gate in Figure 24

Samples were scanned in matched sets, two at a time. Samples -41 and -42 from each set were placed side by side in the immersion tank in the same orientation. The scan began with -41 then -42 was scanned with the output to a single file. The single data file is later split during the data processing phase. The time to complete each scan was approximately 1.5 hours. When completed, a file containing the data to generate 1,714,571 A-scans was transferred from the data collection computer to a more powerful system for processing. The scan process was completed for a frequency of 2.25 MHz through the as-manufactured top surface. Both samples were then rotated 90º and a scan was taken through the side surface. The 2.25 MHz transducer was then removed from the traverse and a 5MHz transducer was installed. The process was then repeated, scanning

through the top and side surfaces of both samples. The 5 MHz transducer was then replaced with a 10MHz transducer and scans were accomplished again through both the top and side surfaces.

3.7 Post Process Machining

Upon completion of UT on all as-manufactured specimens, post process machining was accomplished. Of each set of specimens, -41 was selected to have the upper and side surfaces milled smooth. Sample -42 of each set was not machined and held as a control, also allowing for future testing of as-manufactured specimens. A shell cutter was used on a three axis mill to remove surface roughness. Planarity was maintained using the mill bed while the minimum amount of material was removed to create a new surface. Figure 26 shows the upper and side surfaces before machining; a slight ridge is seen around the upper perimeter from the manufacturing process. The newly machined surfaces are shown in Figure 27 where only minor tooling marks remain.

Figure 26. Sample B-41 top and side surfaces prior to machining.

Figure 27. Sample B-41 top and side surfaces post machining, tooling marks visible on both surfaces

Surface roughness measurements were conducted on the newly machined surfaces. The reduction in surface roughness allowed the use of the profilometer as the machined surface is within the ±120 μm range of the profilometer. Therefore both the top and side faces were again measured using the Taylor-Hobson profilometer. The previous procedures used to measure the top surface were repeated on the two machined surfaces to generate numerical surface roughness.

3.8 Post Process Machining Surface Roughness Results

A considerable reduction in surface roughness was measured in the machined samples. Figure 28 shows a representative machined surface, tooling marks are well defined and are seen forming high radial bands on the surface. Tooling marks are seen on the machined samples as in Figure 27, even with these tooling marks the machined surfaces provided a large reduction in surface roughness. A three dimensional surface map of sample D-41 after milling is provided in Figure 29. The radial ridges on this surface caused by the machining process are apparent. Sample D-41 is representative of all samples with respect to reduction in surface roughness and the presence of tooling marks.

Table 5 provides post machining surface measurements of the top surfaces, and Table 6 shows measurements of the side surfaces. Machining of the upper surface resulted in a mean surface roughness of 3.5 μm RMS and a standard deviation of 0.94 μm RMS. The roughness of the side surfaces after milling averages 5.2 μm RMS with a standard deviation of 2.04 μm RMS. The reduction in surface roughness was substantial

in all samples. In the case of sample M-41 an order of magnitude reduction was achieved. The post machined surface roughness in

Table 5 and Table 6 are compared to those in Table 4 for evaluation. The post processed samples provide an additional twelve surface roughness data points for assessment of UT on EBM samples.

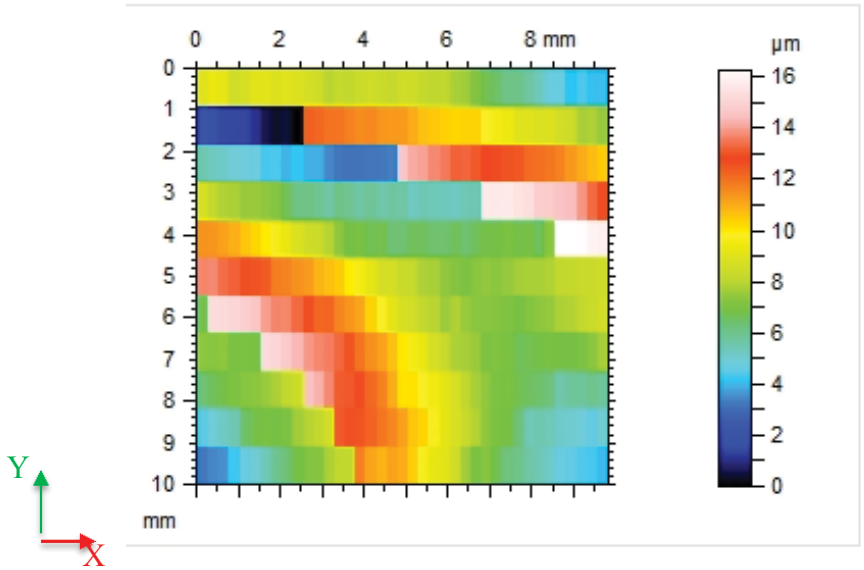

Figure 28. 2-D Profile of sample D-41, top surface post machining with roughness of 3.23 µm RMS

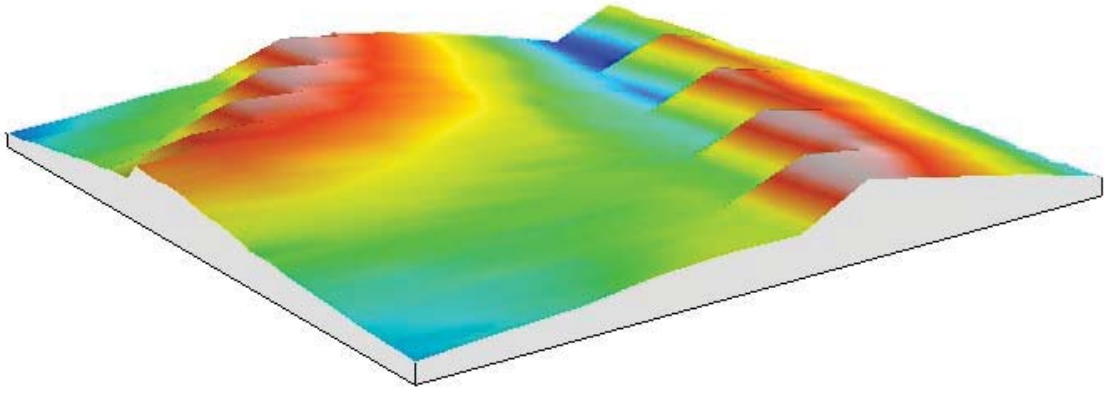

Figure 29. 3-D Surface map of sample D-41, top surface post machining with roughness of 3.23 µm RMS

Table 5. Surface roughness post machining, top surface (μm)

Sample	RMS	Max Valley	Max Peak	Max Peak to Valley	RMS Decrease (%)
A-41	3.22	8.32	9.11	17.43	80.83
B-41	5.02	12.6	8.17	20.77	77.18
D-41	3.23	8.5	7.77	16.27	82.82
E-41	3.85	15.1	9.67	24.77	76.23
L-41	1.86	4.3	5.05	9.35	83.24
M-41	3.72	6	7.67	13.67	79.67

Table 6. Surface roughness post machining, side surface (μm)

Sample	RMS	Max Valley	Max Peak	Max Peak to Valley	RMS Decrease (%)
A-41	7.1	17.6	10.5	28.1	84.27
B-41	7.91	11.7	16.1	27.8	80.66
D-41	5.5	14.2	16.5	30.7	90.63
E-41	5.7	9.69	15.5	25.19	86.98
L-41	2.32	4.86	5.72	10.58	90.89
M-41	2.88	8.31	5.29	13.6	89.35

Resurfacing of samples previously inspected allows for all variables except surface roughness to be held constant, the amount of material removed from each surface was treated as negligible. Multiple surface conditions can provide a reliable assessment on the effect of surface roughness. In order to ensure accurate comparison the same two surfaces on all samples were machined. The orientation of inspection was also accounted for by conduction machining and subsequent UT on the same surfaces previously inspected. The thickness of the removed material is treated as negligible in changing the depth of the flaw from the surface of the sample.

3.9 Post Machining Ultrasonic Inspection

In order to evaluate the effects of surface roughness on the ability to detect flaws, a second set of ultrasonic tests were conducted. Samples were again inspected in sets of two, allowing for comparison with the original set of scans. UT was accomplished through both the top and side surfaces. The same three transducers were used as in previous testing, producing frequencies of 2.25MHz, 5MHz and 10MHz. A representative C-scan is seen in Figure 30.

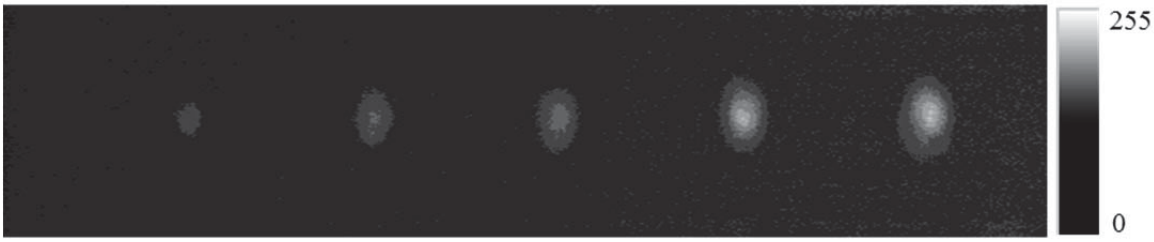

Figure 30. Example of C-Scan, post machining, through top surface

3.10 Data Processing

A useable form of the collected data is required in order to quantify and categorize the data from the ultrasonic scans. The collected data is in the form of one large output file, each approximately two gigabytes. In order to process this large amount of data, MATLAB® was chosen, as it can handle large matrices and arrays. A program was written to read the data into MATLAB in sections, to avoid computer memory issues. Once the data was loaded into MATLAB various built-in functions and user programed codes are available for processing.

Following the initial read-in of the large data file, frequency filtering was accomplished. Raw data was read into an array where a Fourier Transform was performed to decompose the signal into its' frequencies using the following equation.

$$Y_{p+1,q+1} = \sum_{j=0}^{m-1}\sum_{k=0}^{n-1} \omega_m^{jp}\,\omega_n^{kq}\,X_{j+1,k+1} \tag{7}$$

Given an input X, Equation 7 uses ω_m and ω_n to represent complex roots of unity, $e^{-2\pi i/m}$ and $e^{-2\pi i/n}$ respectively. The notation i represents the imaginary unit, p and j are indices ranging from 0 to m–1. Indices q and k run from 0 to n–1 while p and j run from 1 to m and the q and k run from 1 to n [36]. The resulting Y is a decomposed set of frequencies which comprised the original input signal. Decomposition allowed application of a filter to limit the range of frequencies in the data. For all samples this range was set from 0.5 MHz to 12 MHz, reducing outside interference received by the transducer during data collection.

Frequency filtered data was then inversely transformed back into the time domain. In ultrasonic wave transmission, velocity in a medium is constant, therefore time corresponds to distance through the sample [13]. As a result, the inversely transformed array contains filtered layers stacked either parallel or perpendicular to the build direction depending on scan orientation. To obtain the strongest ultrasonic returns from this array in a manageable form, the matrix of data corresponding to the center of the sample was selected. The center-plane matrix was combined with the five matrices above and five below the center, then normalized to form one representative matrix as shown in Figure 31.

Figure 31. Combine data from 11 center matrices compiled into C-Scan, 5 MHz

The processed data compiled into a single greyscale image, seen in Figure 31, allows for the use of image processing techniques. These techniques were used to measure the size and intensity of the flaws detected by the ultrasonic transducer. The single representative matrix was reduced to a greyscale image to facilitate image processing techniques. A single greyscale image allowed for the use of an image erosion function. Image erosion was used to remove indications smaller than the transducer was physically capable of detecting. The erosion of an image uses a structuring element to compare an image pixel with its' neighboring pixels. Generally, UT techniques can only detect a flaw equivalent in size to one half the wavelength at the frequency used [13]. The size of the structuring element was set to one-half of the wavelength size for each frequency and the number was rounded down to the nearest whole number of pixels. An example of this is seen in Figure 32. Image erosion ultimately reduced the intensity of small spikes in amplitude at lower levels while retaining pertinent data. An example of this is seen in Figure 33 on a surface plot. It is easily shown how the localized single pixel signal spikes are reduced. The removal of single pixel spikes in intensity is important for the next image processing tool used on the filtered data as it is a pixel gradient based technique.

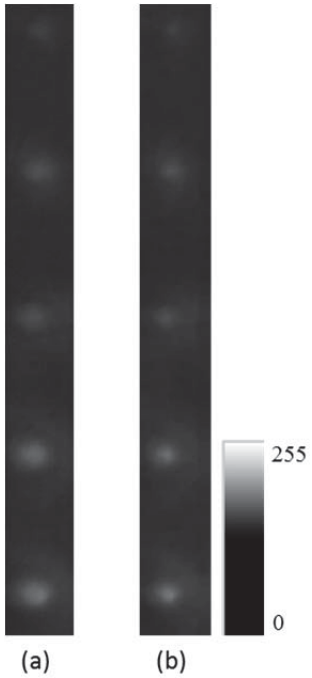

Figure 32. Image erosion (a) raw image prior to erosion, (b) eroded using disk shaped structure element, sample D-41 2.25 MHz transducer top surface

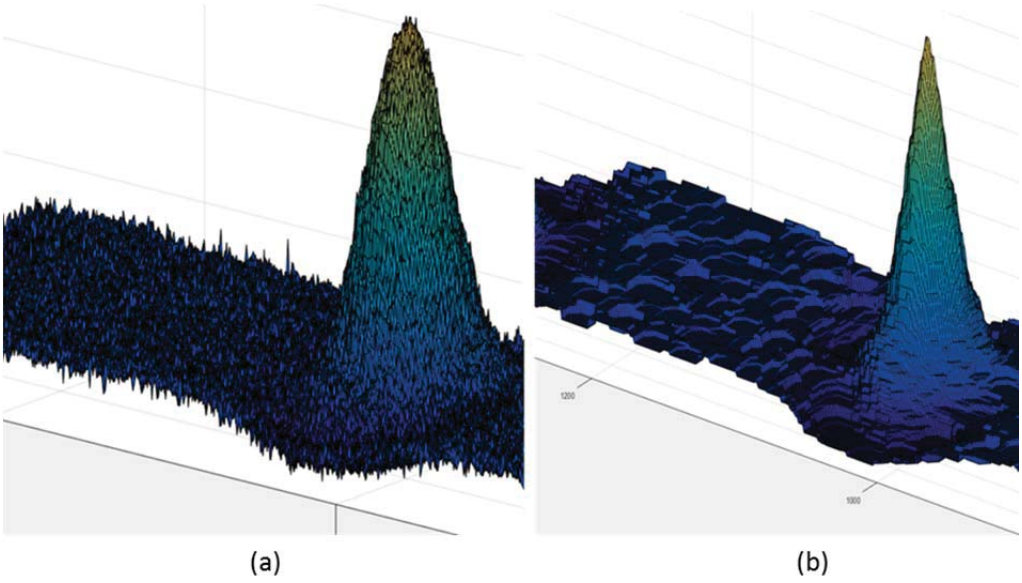

Figure 33. Image erosion example, (a) surface plot before image erosion, (b) surface plot following image erosion

The final function used in this analysis was the Circular Hough Transform. The Hough Transform is the method behind circle detection used to measure and classify the flaws in the samples. The eroded images still contain a certain level of noise; thus the Hough Transform is an excellent tool since it is generally unaffected by this noise [37]. The first step of this approach is the determination of the image pixels with the highest gradient. These pixels are then identified and recorded. As groups of high gradient pixels are identified with a similar distance to a center point, those pixels are set as points on the circumference of the circle. User definable input arguments are: input image, radii range, object polarity, computation method, sensitivity, and edge threshold. Outputs include coordinates of the center of any detected circles, as well as the corresponding radii [38]. Radii range was set to 0.48mm to 3mm based on the design size of the spherical flaws. Image intensity corresponds to the amplitude of return of the ultrasonic wave during testing, therefore object polarity was set to detect bright objects in the image. Sensitivity was found using an iterative method, starting with a low value and incrementally increasing until the maximum number of known flaws were identified. Sensitivity was recorded for each sample set for use in later analysis.

An example of the Hough Transform is shown in Figure 34. A red circle is used to identify the outer diameter of the detected area. A pixel count measurement is used to determine the diameter of the circle. In this example 2.54 cm is 844 pixels, the pixel count of the red circle's diameter is 208. This results in a diameter of 0.6274 cm. The measured diameter of the white circle is 0.642 cm, this gives an error of approximatly

2.3% using this technique. The method described above was used on erroded images to measure the diameter of internal flaws in the samples.

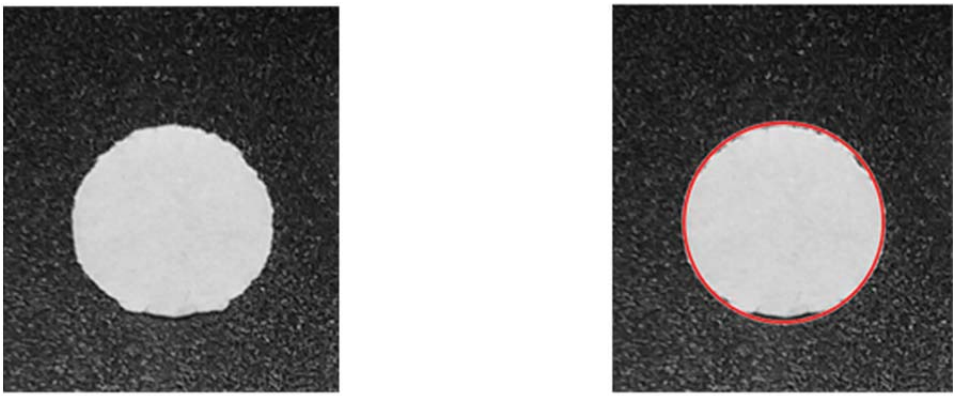

Figure 34. Hough Transform (a) Non-uniform Circular Object (b) Red Circle Identifies Outer Diameter of Circular Object

IV. Analysis and Results

4.1 Observations in Test Specimens

A total of 12 samples were produced in six different production runs. Both the Arcam A2 and Q10 machines produced comparable end products. Some slight differences were noted, mostly to exterior surface condition. The three powder lots used to manufacture all samples were procured from Arcam, or Arcam authorized suppliers to identical specifications. For the scope of this research, all three lots are treated as identical, thus attributing any observed variation in samples to other factors, discussed in subsequent chapters.

Samples A, B, D, and E possess similar top and side surface features. A representative image of these samples is seen in Figure 35. The image shows a series of vertical, parallel to the Y-axis, striations on the surface of the sample. The cause of these striations is a variation in the beam current across the sample in the X direction. Figure 36 gives the current of the beam across the samples, in particularly from a layer of sample A-42. Variation of beam current is a machine parameter built into the standard build program. Even the simple geometry of this layer has an approximately 60% difference in current. As depicted in Figure 36, certain areas of a sample receive significantly less current than others. Note that some builds have seen a variation of up to five times across a single layer of a single sample [39]. Figure 37 shows the alignment of the beam variations with the striations on the upper surface of the as-manufactured sample. It is currently unknown the extent this variation in current and the resulting

surface blemishes affects the internal transmission of ultrasonic waves and is not considered in this work.

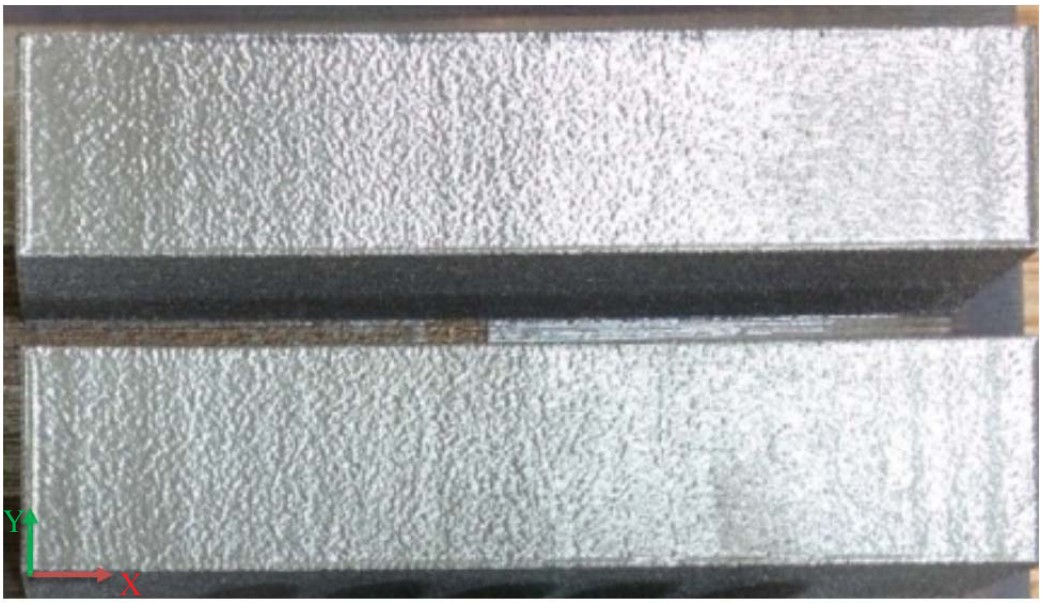

Figure 35. Samples A-41 (top) and A-42 (bottom) top surfaces, vertical lines visible on surface due to current variation during build [39]

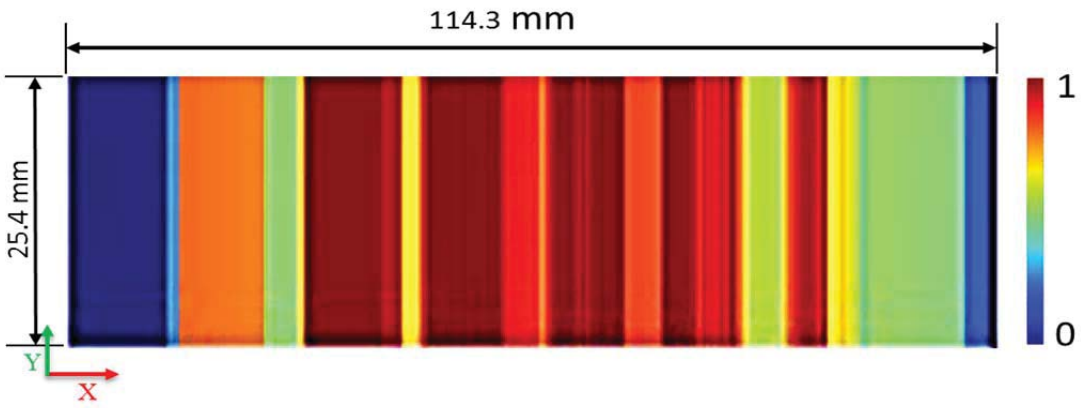

Figure 36. Beam current by location, single layer of Sample A-42 [39]

Figure 37. Beam current map compared to surface striations, Sample A-42 [39]

Previously mentioned in Chapter 3, samples L and M were manufactured on Arcam's Q10 as opposed to the A2 system used for all other samples. The Q10 system uses a different algorithm to determine electron beam pattern and intensity from the A2. Detailed information of the beam current across the build area was not investigated in as much depth for the Q10 system. The Q10 is a newer generation of technology and the software used to control the build is still periodically updated. It is known the Q10 system does not restrict the electron beam to patterns strictly in the X or Y direction, but allows diagonal melting of the powder on the build surface. The diagonal pattern, seen in Figure 38, is created by boundaries imposed by the manufacturing software. The markings on all samples are minor enough to where they are undistinguishable from the surrounding surface using a surface profilometer.

Figure 38. Sample L-41 top surface, visible diagonal striations on top surface due to beam pattern variation.

4.2 EBM Sample Ultrasonic Scan Analysis

Upon completion of the data collection it became apparent many variables factor into the ability of UT to detect a flaw in an EBM sample. This section will focus generally on the findings of all inspections performed on the samples described in section 3.2. Further analysis of the samples by surface roughness is addressed in later sections. Traditionally, NDI data is reported as a "Hit/Miss" or "Pass/Fail" signal response with only the result recorded. Techniques such as this can lead to variability in data due to many parameters such as equipment, procedure, calibration, criteria, and human factors [40]. Several precautions were taken to reduce variability in the data collected for this research. To eliminate equipment and procedural variations, the same UT workstation was used for all collected data. In order to reduce inconsistencies due to acceptance criteria and human interpretation factors, repeatable computer based methods described in chapter 3 were used to classify hit or miss conditions on all data.

Figure 39 provides a representative graph of the ability of the UT and data processing technique to detect the known defects in the Ti-6Al-4V EBM samples. In this graph, the ordinate provides the ratio of detected flaws (n) to the number of known flaws present (N). The abscissa gives the diameter of the designed flaws in the samples. Each

designed flaw size has 36 inspections per frequency, comprising a variety of surface roughness as well as inspection through perpendicular sample faces. From this graph, it is seen a 10 MHz transducer provides a higher detectability throughout the range of flaw sizes. Lower frequencies, such as 2.25 MHz and 5 MHz, both provide lower detectability starting at a 0.51 mm flaw with a slight increase in detection as flaw size increases. Both 2.25 MHz and 5 MHz reach a detectability near 0.75 despite the flaw size, with no regard to surface roughness. The disparity between frequencies, as well as surface roughness factors limiting detectability are explored in depth in later sections.

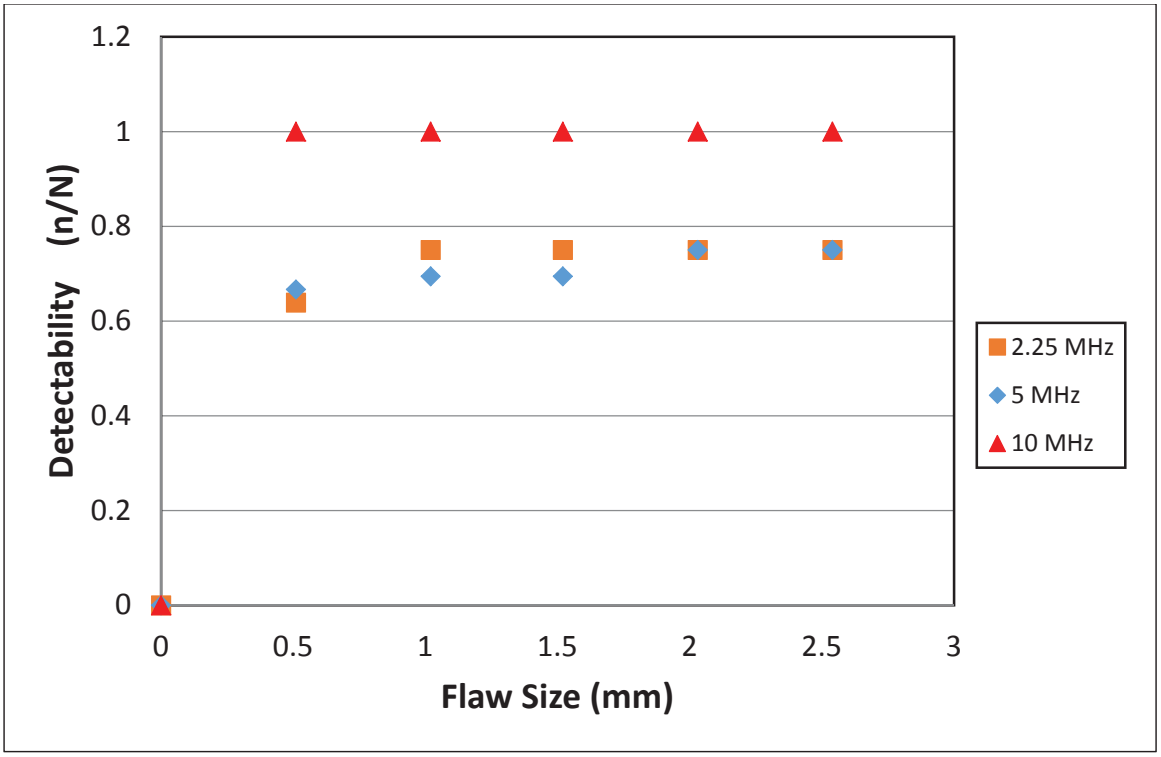

Figure 39. Detectability of flaws by size and frequency using UT

Figure 40 gives a more detailed look into the detection ratio of all samples at all inspection frequencies used. Both 2.25 MHz and 5 MHz frequencies show a reduced

detection ratio for smaller flaws with a slight increase as the size of the flaw increases. Figure 40 indicates no increase in detectability as the designed flaw size increases beyond 0.102 mm for a frequency of 2.25 MHz, while 5 MHz shows similar results, but with another incremental increase at 2.03 cm. The prescribed UT procedure detected all flaws with a designed diameter over 0.51 mm at a frequency of 10 MHz.

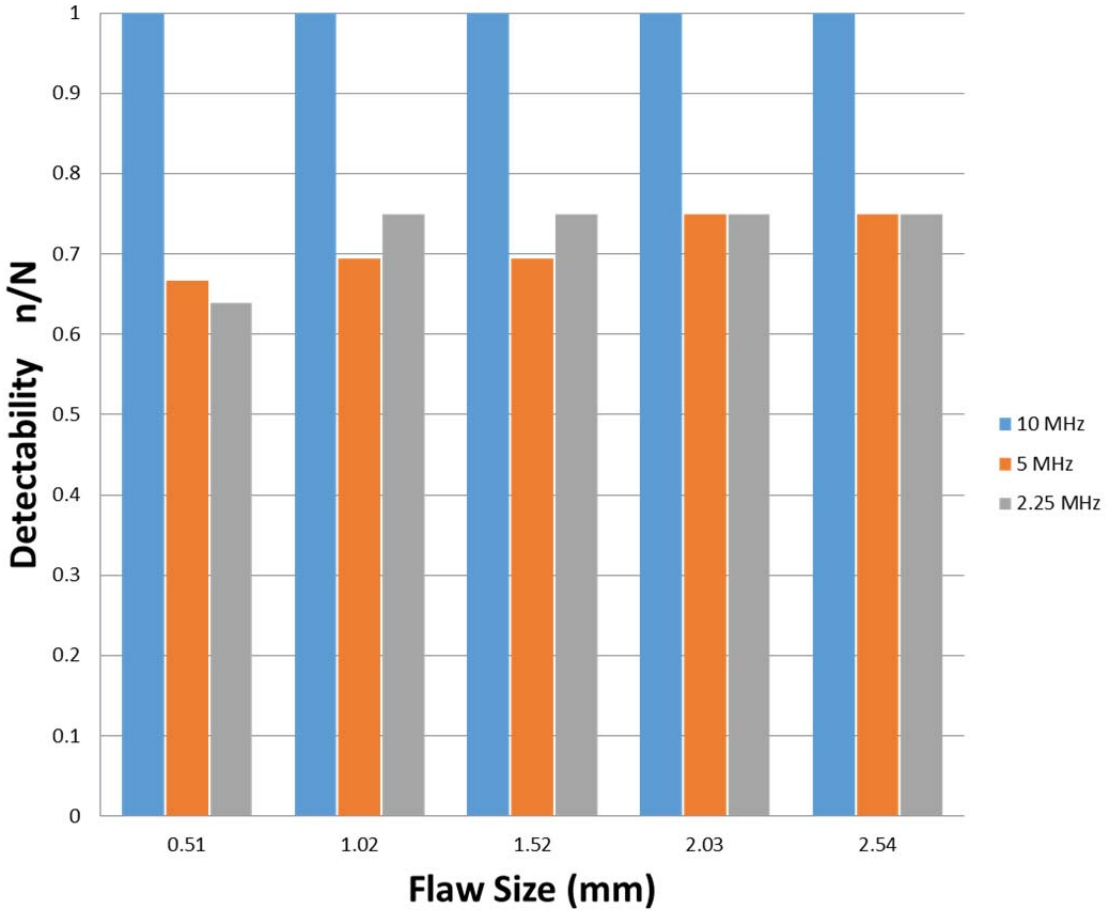

Figure 40. Detectability of flaws by size at all inspection frequencies

The data presented above shows the results of all UT performed regardless of surface roughness or build orientation. Results of this data with consideration to surface roughness reveals for lower frequencies, 2.25 MHz and 5 MHz, approximately 25% of

flaws which were not detected were through surfaces with the highest surface roughness. This implies knowledge of surface roughness can reduce a potential source of uncertainty in the UT of EBM Ti-6Al-4V. Using surface roughness measurements, along with corresponding UT scans, further analysis of the relationship between surface roughness and detectability is conducted in later sections.

4.3 As-Manufactured Ultrasonic Scan Results

Ultrasonic scans were collected and compiled into a usable image of a C-scan. Examples of the compiled images are presented in this section with the Hough transform used to identify the embedded flaws with red circles. Each figure represents the difference in results for C-scans at three different inspection frequencies with subfigure (a) at 2.25 MHz, (b) at 5 MHz and (c) at 10 MHz. Shown in all of these figures, the size of the identified flaw does not correspond to its actual design size. For example, comparing Figure 41 (a) and (b) to Figure 42 (a) and (b), respectively, the size of the identified flaw is not consistent between samples even for the same designed flaw size. To allow future testing of the samples used in this experimentation, destructive testing was not conducted on these samples. With the inability to destructively inspect these samples to measure actual flaw size, CT scans were consulted. Consistent flaw size among samples within a production run was noted based on the data available from CT scans. Figure 43 provides a representative comparison of the 2.54 mm flaw in samples A-41 and A42, using a circular Hough transform to measure the diameter of the flaws. The difference in diameter between the two samples was 5%, based on the CT scan, compared to the UT scans where several detected flaws differ by a factor of five between

samples. Figure 44 is provided as a comparison between production runs, showing again inconsistent size identification throughout the frequency ranges. The inconsistency of detected diameter, compared to design diameter and between samples, lends to the use of the Hough transform as means to provide the standard hit or miss classification for known defects used in previous studies [40].

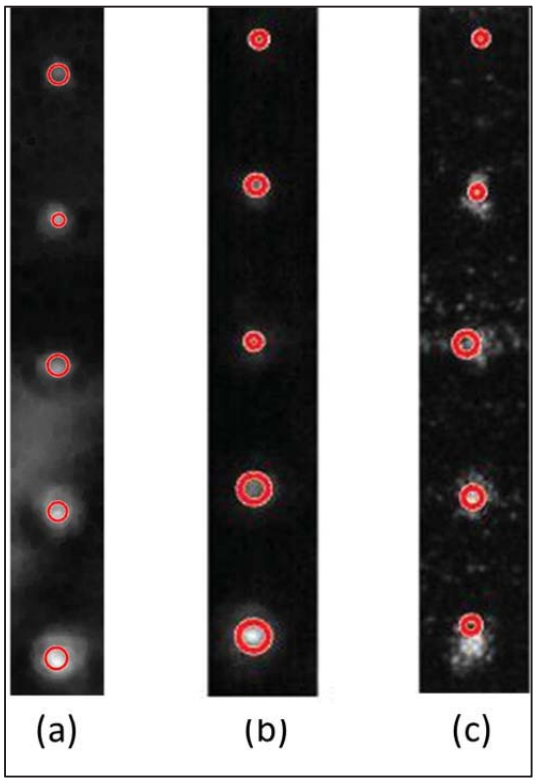

Figure 41. Sample A-41 as-manufactured top surface with roughness of 16.8 µm RMS (a) 2.25 MHz, (b) 5 MHz, (c) 10 MHz

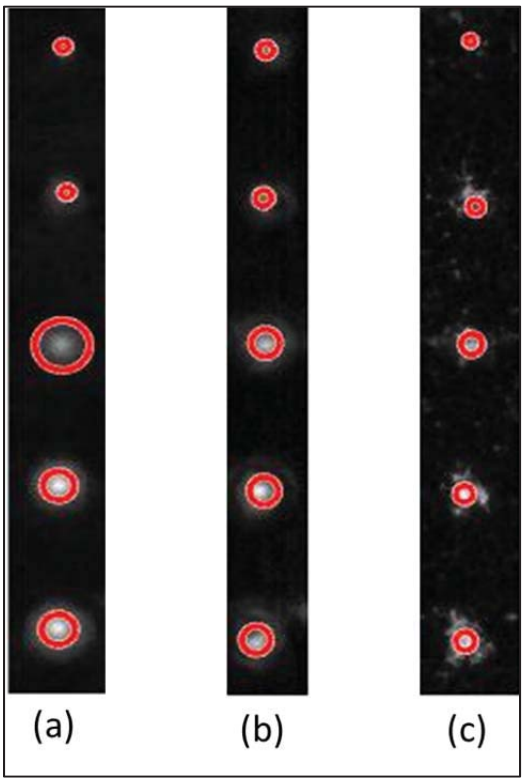

Figure 42. Sample A-42 as-manufactured top surface with roughness of 16.2 µm RMS (a) 2.25 MHz, (b) 5 MHz, (c) 10 MHz

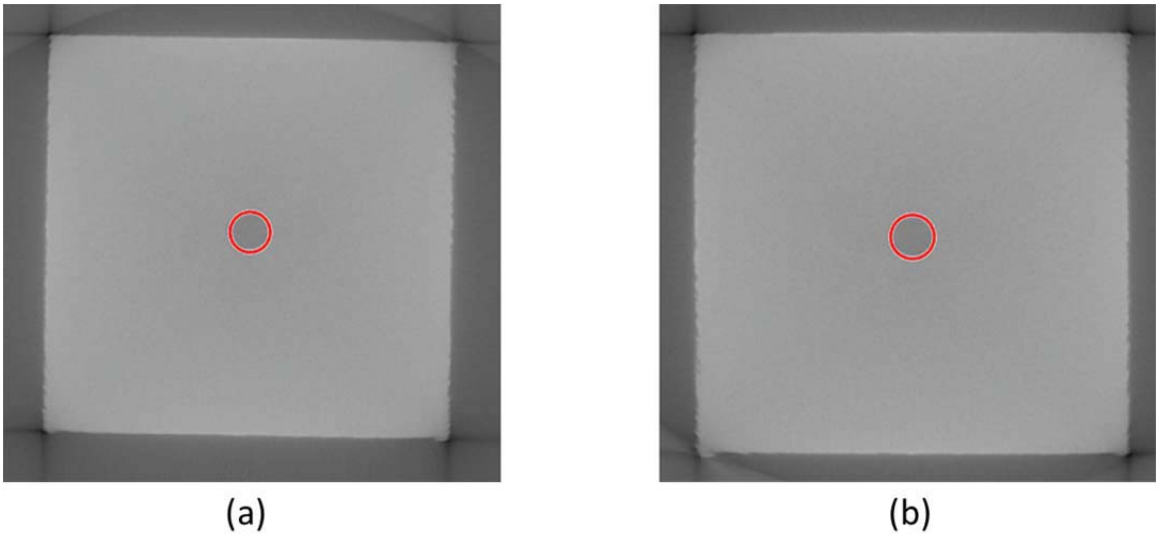

Figure 43. CT scan results comparing flaw size of sample A-41 (a) 2.42 mm, to sample A-42 (b) 2.55 mm

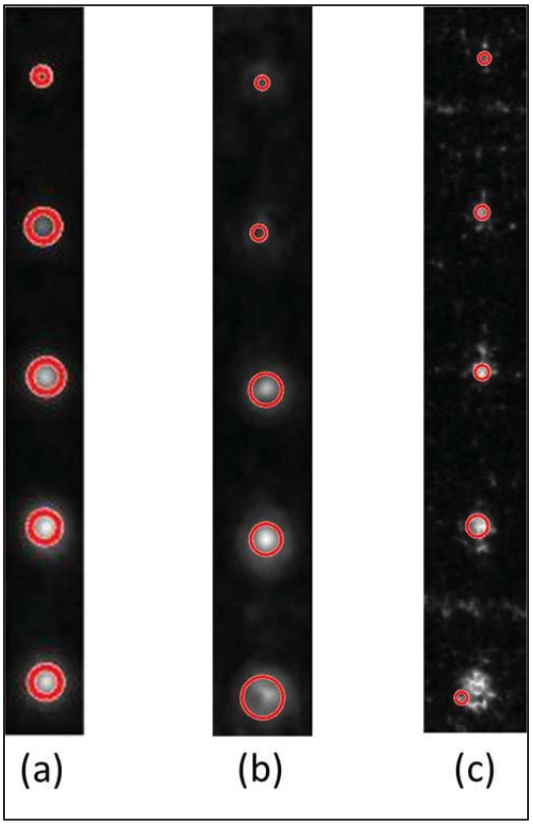

Figure 44. Sample B-41 as-manufactured top surface with roughness of 22 μm RMS (a) 2.25 MHz, (b) 5 MHz, (c) 10 MHz

At 10 MHz, a scattered return is seen through all as-manufactured upper surfaces. This is expected, as grain noise levels increase with inspection frequency. The grain noise is the dispersion of the ultrasonic wave at the boundaries of the microstructural grains for a given sample [41]. Antonysamy *et. al.* examined grain structure of EBM Ti-6Al-4V and determined a coarse β-grain structure, with irregular columnar grains aligning along the z-axis. Figure 45 shows this grain structure using an Electron Back Scatter (EBSD) map [25]. Based on the irregularity and orientation of the grains, the scattered return at 10 MHz is easily attributed to this characteristic. As the ultrasonic wave is transmitted from grain to grain not only is energy dissipated at grain boundaries as with traditional material, but the shape of the grains is causing the transmission of the wave created by the ultrasonic transducer to travel outward away from the area the transducer can receive the return. When the ultrasonic wave hits a discontinuity such as the designed defects in the samples, the wave reflected from the discontinuity is again affected by the shape and orientation of the grains. The length of a wave is inversely proportional to the frequency of the wave through a given medium, therefore higher frequency waves have a smaller wave length [13]. This results in grain size and inter-grain boundary condition having more effect on higher frequency waves in the material studied.

Figure 45. Electron Back Scatter (EBSD) map from X–Z cross sections [25]

Figure 46 is a representative image of samples manufactured using the Arcam Q10 machine. Diagonal sections of high intensity are seen through the upper surface on all samples made on the Q10 system. Prominently seen at 5 MHz and 10 MHz, these returns correspond closely to the surface marking on each sample in lots L and M. Figure 46 (b) illustrates the potential for variation in current used during the build, previously discussed, to mask areas where flaws are present.

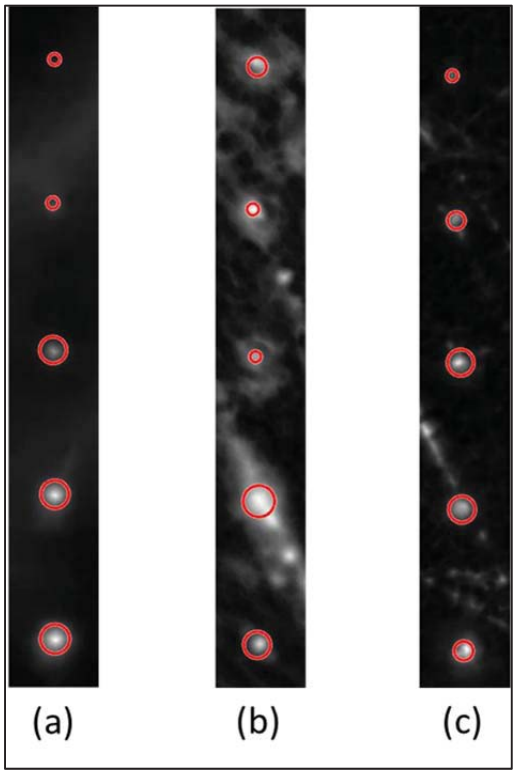

Figure 46. Sample M-42 as-manufactured top surface with roughness of 15.8 μm RMS (a) 2.25 MHz, (b) 5 MHz, (c) 10 MHz

For comparison of EBM samples with a forged titanium alloy sample, Figure 47 is included below. The C-scan is of a 5.08 cm cube of titanium alloy, including nine flat bottom holes drilled from the face opposite the inspection surface. A frequency of 10 MHz was used and the beam was focused at the bottom of the holes [42]. This setup differs slightly from the 10 MHz scans collected on the EBM AM samples. The primary difference is the manufacturing process, the sample in Figure 47 was forged as opposed to additively manufactured. Forging is a process which uses mechanical forces to shape a material through compression. As a result of the AM process, it is assumed the spherical defects remain filled with un-melted powder while the forged samples have empty holes as the subject of inspection [14]. This has the potential for the embedded flaws to cause

returns unlike those of a drilled hole, as the ultrasonic wave transmits through the unsintered powder with unknown interactions between powder grains. Thompson *et. al.*, did not provide a surface roughness for the sample under inspection but did state the sample was forged [42]. Forged materials traditionally have a surface roughness less than 12 μm RMS depending on the forging technique used [43]. Figure 48 represents the most similar C-scan from the data collected during this study, sample L-41 with a surface roughness of 11.1 μm RMS. Sample L-41 shows high amplitude returns at the areas of the flaws, in the same manner as the forged sample shown in Figure 47. In the forged sample, areas where no hole exists no additional returns are seen, where in the EBM sample, returns from beam current variations and potentially grain scattering are present throughout. It is evident at 10 MHz the forged material produces a less scattered return in the C-scan, when compared to a similar EBM sample.

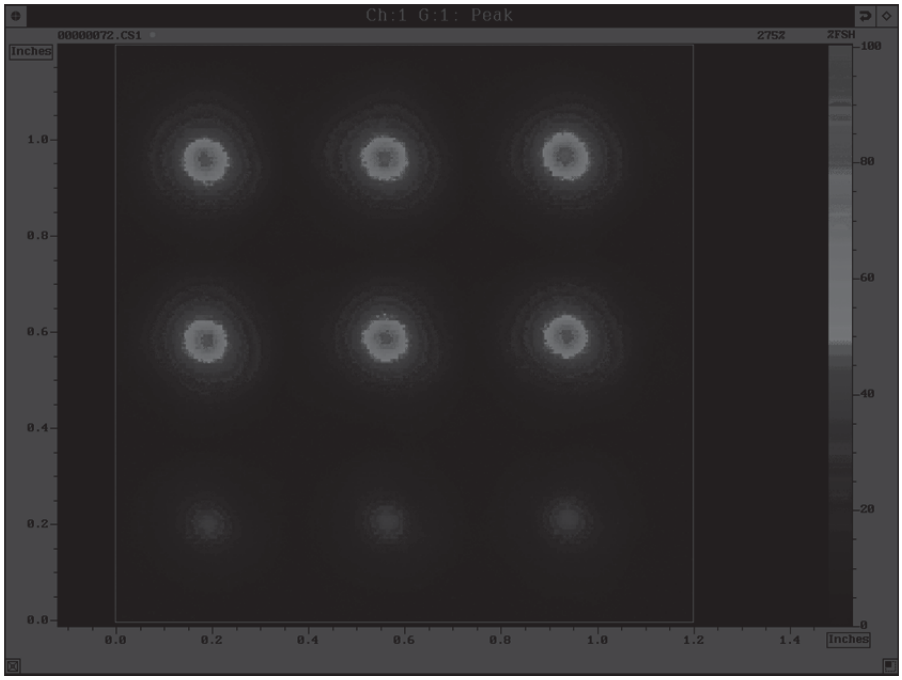

Figure 47. Ultrasonic scan of titanium alloy at 10 MHz of flat bottom holes drilled in 2 inch block, top 6 holes 0.397 mm diameter, bottom 3 holes 0.254 mm diameter [42]

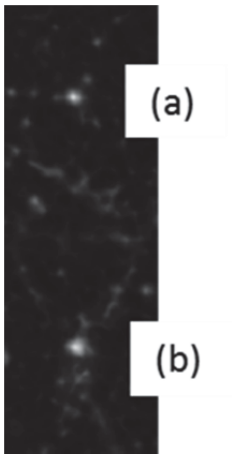

Figure 48. Sample L-41 C-Scan as-manufactured top surface with roughness of 11.1 μm RMS (a) 0.508 mm defect (b) 1.016 mm defect

Figure 49 and Figure 50 provide examples of scans taken through the rougher side surfaces of the samples. All samples A through E exhibited similar behavior at 2.25

MHz and 5 MHz where no detectable defects were found. Scans performed through these surfaces at 10 MHz produced a smaller return, closer in size to the actual design size of each flaw. At 10 MHz the intensity of the return was high in the defect area with a sharp gradient to the surrounding material. Samples L and M provided similar results at 10 MHz through the side of the sample, but had usable returns at 2.25 MHz and 5 MHz. Figure 50(a) and (b) illustrate the returns at lower frequencies where four of five and two of five flaws were found. Note the lower surface roughness, 25.5 µm RMS, of sample M-42 in Figure 50 compared to the 45.1 µm RMS of sample A-41 in Figure 49. Likewise, when sample B-41 in Figure 50 is compared to sample M-42, Figure 44, all flaws are detected though a surface with a 3.5 µm RMS lower surface roughness.

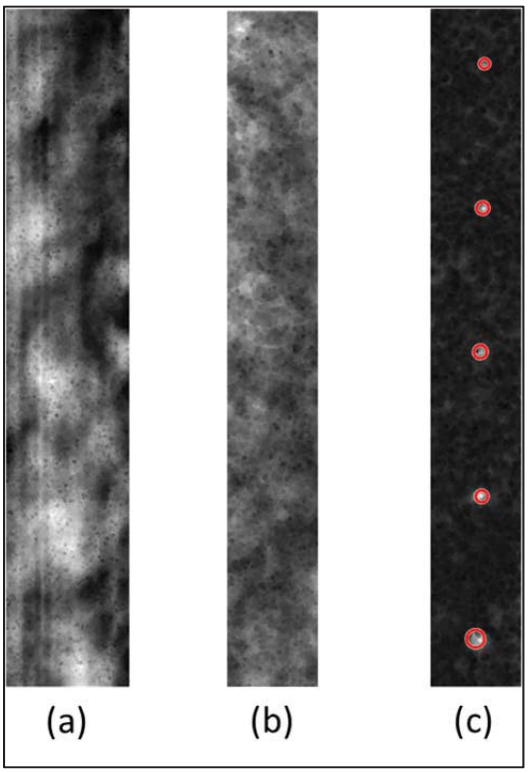

Figure 49. Sample A-41 as-manufactured side surface with roughness of 45.1 µm RMS (a) 2.25 MHz, (b) 5 MHz, (c) 10 MHz

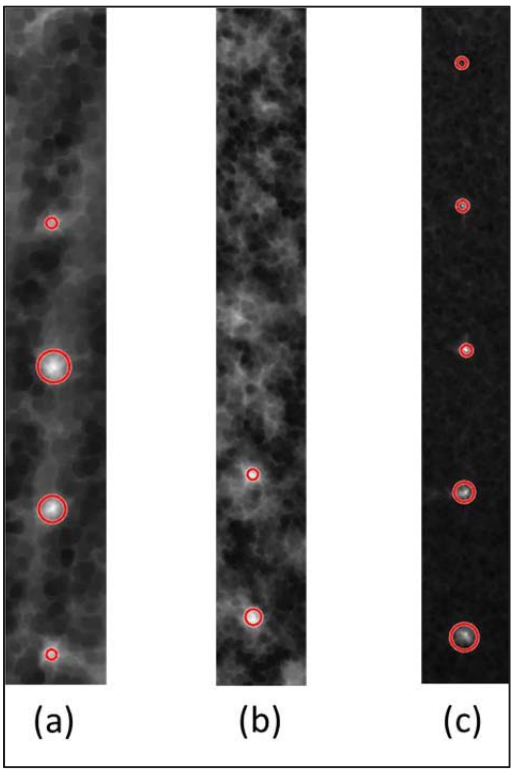

Figure 50. Sample M-42 as-manufactured side surface with roughness of 25.5 µm RMS (a) 2.25 MHz, (b) 5 MHz, (c) 10 MHz

Detection data from all as-manufactured top surfaces was tabulated and is included in Appendix E. These tables show detection based on hit/miss of the Hough Transform on the eroded images representing C-scans of each sample. All three inspection frequencies were examined using this criterion. Based on this principle, all designed flaws were detected when scans were taken through the upper surface prior to any post process machining. Surface roughness ranged from 11.1 μm to 21.2 μm with corresponding peak to peak surface measurements from 71.3 μm to as high as 115.3 μm as detailed in the previous chapter.

Similar to the top surface detection data Appendix F contain detection data from UT scans, but taken through the rougher as-manufactured side surfaces. Unlike the scans taken through the upper surface, all flaws were not detected at all inspection frequencies. At a frequency of 2.25 MHz, all samples manufactured on the A2 system, samples A-41 through E-42, provided no defect indications through the side surface. Samples in lots L and M, manufactured on the Q10 system, inspected at 2.25 MHz provided flaw indications on designed defects larger than 1.02 mm in diameter. Likewise, at 5 MHz, samples A through E had no flaw indications through the side surface. Samples with lower surface roughness, L and M, did provide returns which were detectable but not as consistently at 2.25 MHz. As with scans taken through the upper surface, 10 MHz scans through the side surface identified all designed defects in all twelve samples.

The data provided in this section presents detection data for ultrasonic scans through as-manufactured surfaces of varying roughness. Detectability was examined at two orientations, through the upper surface and the side surface. To investigate the

influence of surface condition on the detection of the designed defects, surface roughness of the samples was reduced through machining as described in Chapter 3. The change in surface roughness of each sample and any change in flaw detection through the newly machined surface is examined.

4.4 Post Machining Ultrasonic Scans Results

Once the machined surface roughness was established, UT was repeated on all samples. With samples scanned in pairs, as before, sample -41 of each set was machined while -42 was still in as-manufactured condition. No change was noted in samples not subject to post process machining therefore the focus is on the refinished samples. There was however a noticeable difference in the results for samples in which the surface was machined. The figures in this section are repetitive of all scans taken through machined surfaces. Images not referenced in this chapter are found in the appendices.

Figure 51 (a), (b), and (c) denotes the flaws found in sample A-41 after machining. Comparing Figure 51 (a), (b), and (c) to Figure 51 (d), (e), and (f), machining appears to diminish the large areas of returns not associated with known flaws. This reduction is seen more at 2.25 MHz but exists at all frequencies. The decrease allows better distinction between designed defects and noise. Figure 52, similarly shows sample B-41 with a reduction in surface roughness of approximately 17 μm. As with sample A-41 a general reduction in noise is seen in the machined sample. The results seen in samples A-41 and B-41 were typical of all samples manufactured on the Arcam A2 system. Figure 53 shows sample M-41 before and after machining, the diagonal lines seen on this sample were not a result of machining. The streaks were present prior to

machining and were also seen in Figure 46 on sample M-42, they are a result of the algorithm used in the building phase. Even with the removal of the original surface to include the visible diagonal striations, these patterns are detected from within the sample. The intensity of these returns created by the diagonal pattern is shown on a surface plot in Figure 54, three of the five designed defects are visible while the other two are obscured.

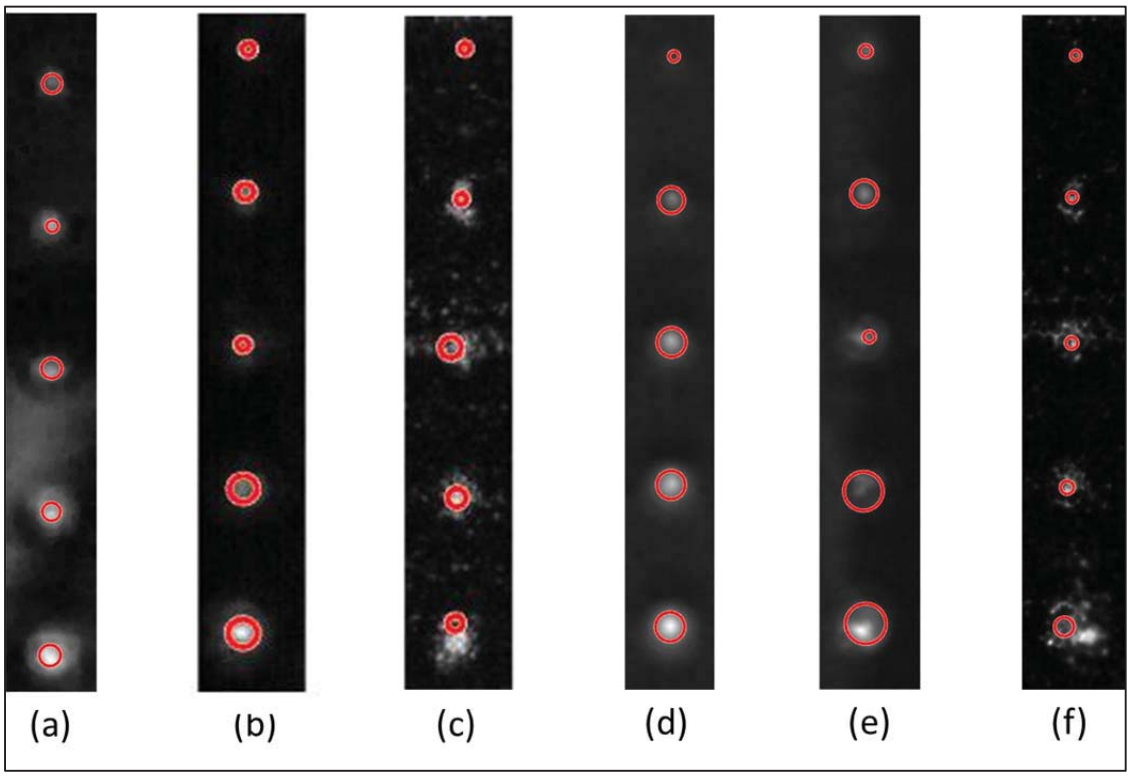

Figure 51. Sample A-41 top surface (a) 2.25 MHz as-manufactured, (b) 5 MHz as-manufactured, (c) 10 MHz as-manufactured, (d) 2.25 MHz milled, (e) 5 MHz milled, (f) 10 MHz milled.

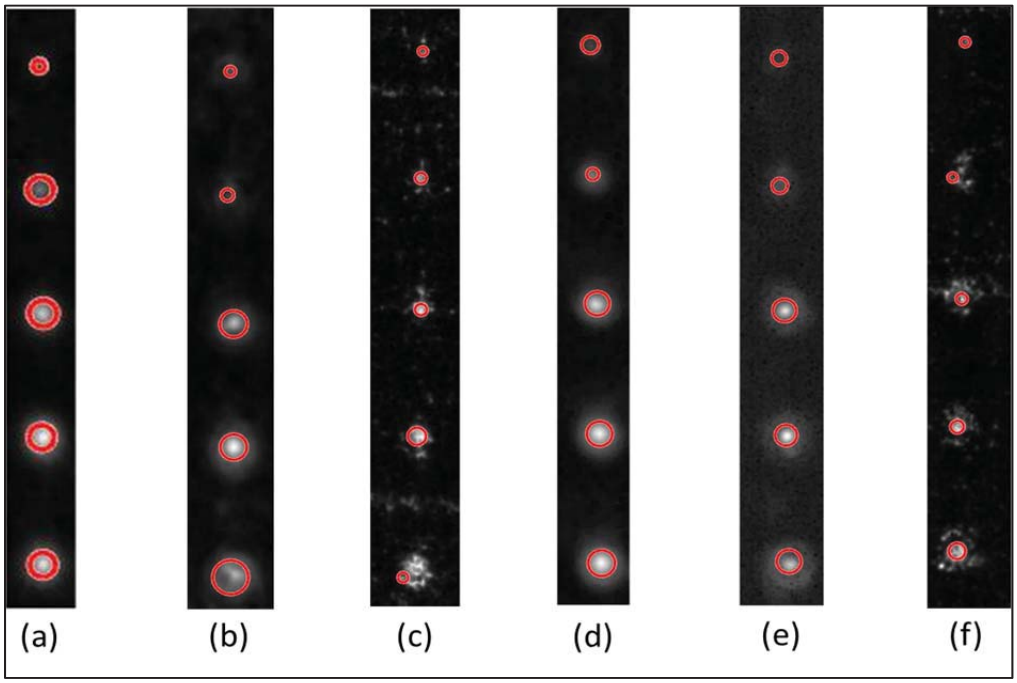

Figure 52. Sample B-41 top surface (a) 2.25 MHz as-manufactured, (b) 5 MHz as-manufactured, (c) 10 MHz as-manufactured, (d) 2.25 MHz milled, (e) 5 MHz milled, (f) 10 MHz milled.

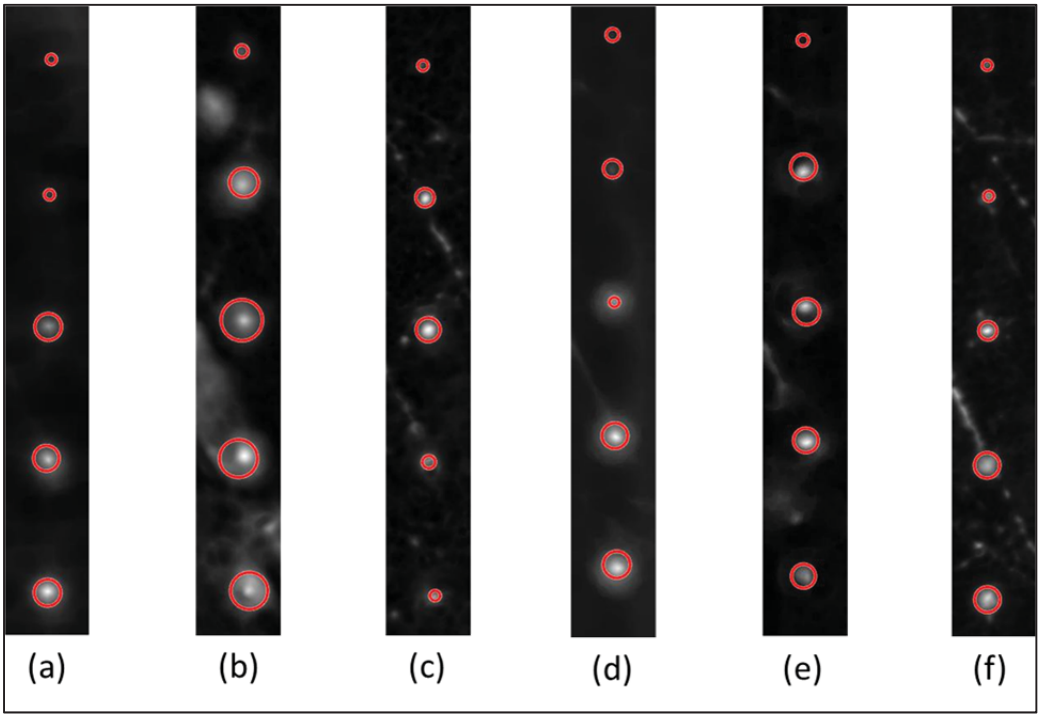

Figure 53. Sample M-41 top surface (a) 2.25 MHz as-manufactured, (b) 5 MHz as-manufactured, (c) 10 MHz as-manufactured, (d) 2.25 MHz milled, (e) 5 MHz milled, (f) 10 MHz milled.

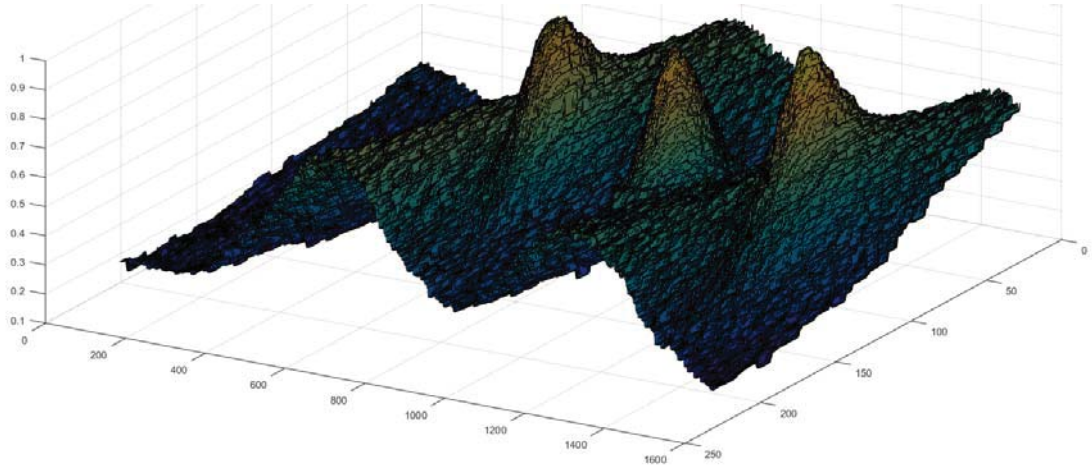

Figure 54. Surface plot of sample M-41 top surface, 2.25 MHz

Unlike the as-manufactured side surfaces, the machined side surfaces did provide usable returns at 2.25 MHz and 5 MHz. As shown in Figure 55 (d) and (e) all designed defects are now visible and detectable using the circular Hough Transform. With the as-manufactured side surface's roughness of 45.14 μm and a peak to peak distance of 307 μm, no flaws were visible. Now with a reduction in RMS roughness of 38 μm, all designed spherical defects are identifiable. Sample M-41, seen in Figure 56, is the only sample where a previously undetectable defect remains undetectable after the machining process. Upon close visual inspection of Figure 56 (a), a slight indication is seen at the top of the sample in the properly spaced vicinity of the designed 0.51 mm defect. Even with this visual indication the Hough Transform was unable to detect the flaw, therefore it is counted as a miss.

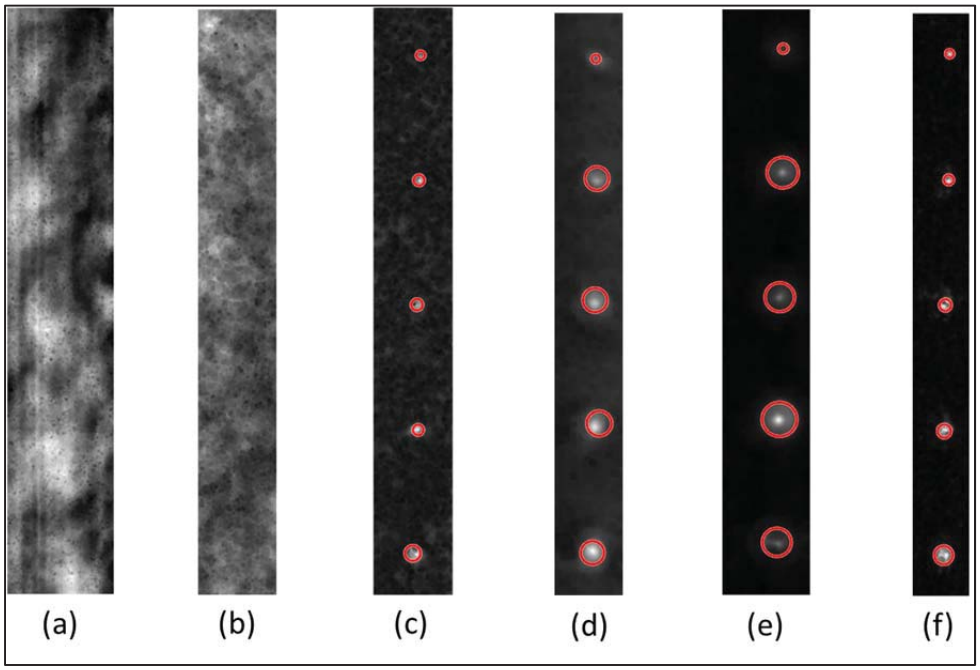

Figure 55. Sample A-41 Side Surface (a) 2.25 MHz as-manufactured, (b) 5 MHz as-manufactured, (c) 10 MHz as-manufactured, (d) 2.25 MHz milled, (e) 5 MHz milled, (f) 10 MHz milled.

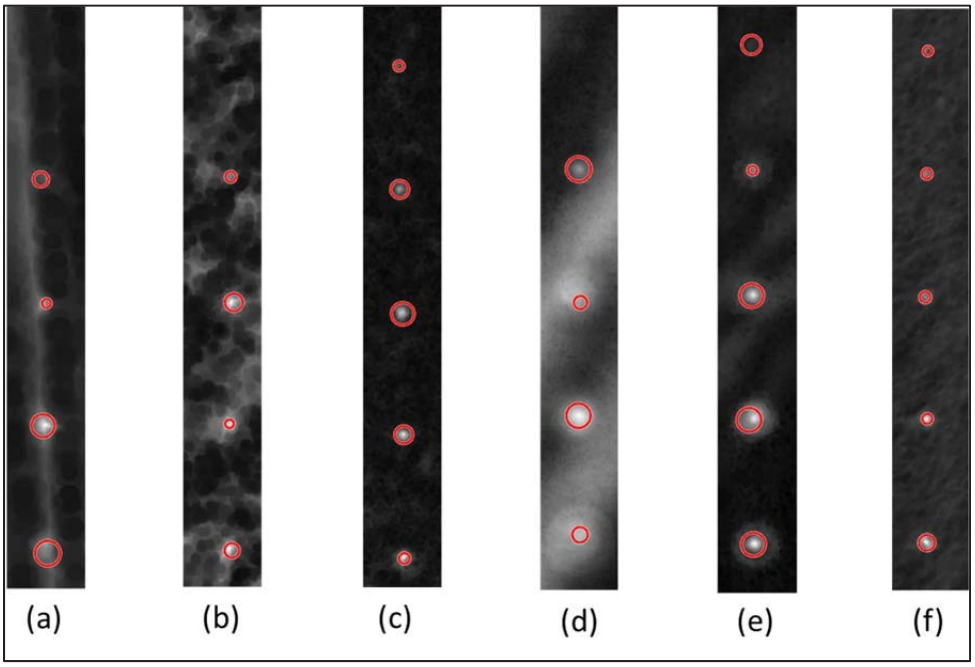

Figure 56. Sample M-41 Side Surface (a) 2.25 MHz as-manufactured, (b) 5 MHz as-manufactured, (c) 10 MHz as-manufactured, (d) 2.25 MHz milled, (e) 5 MHz milled, (f) 10 MHz milled.

The failure of the UT scans to identify the 0.051 cm defect at 2.25 MHz on a machined surface only for sample M-41 led to further investigation of this designed defect. CT scans were performed to verify the existence of this flaw in the sample and examine its characteristics. The output from CT scans of multiple samples were compared, the results are seen in Figure 57. Subfigures (b) and (c) are CT images of samples A-41 and B-41, respectively. Both of these samples had positive flaw indications, where M-41 seen in subfigure (a) did not. Using a circular Hough Transform to identify the diameter of the defect in the CT image, it was discovered the 0.051 flaw in sample M-41 has a diameter of 0.0655 cm. Samples A-41 and B-41 have detected diameters of 0.1428 cm and 0.1166 cm respectively, roughly twice the size of M-41. From this size difference it is concluded the designed 0.051 cm flaw is undersized in sample M-41 when compared to other samples. This causes the size to fall below the threshold of detectability for a frequency of 2.25 MHz through this material at the surface roughness of 3.72 μm RMS.

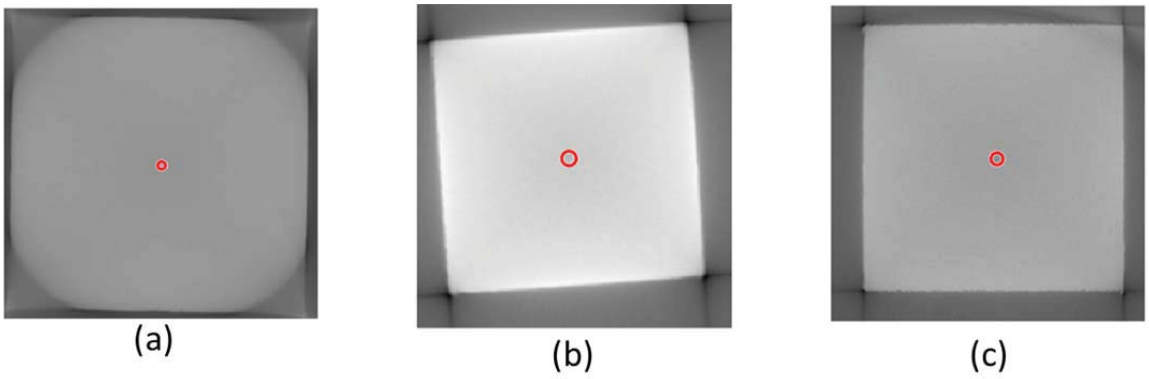

Figure 57. CT scans 0.051 cm designed defect; (a) sample M-41, (b) sample A-41, (c) sample B-41

The results of post machining ultrasonic scans through the top surface were tabulated and are shown in Appendix G. The results indicate at the three experimental frequencies, all designed defects were detected. This demonstrates machining surfaces of the samples did not adversely affect the results of UT through the top face. Any previously identified flaws were still identifiable after machining. Any improvements were not determined, as even the smallest defects were detectable through the roughest as-manufactured upper surface.

Appendix H contains detection information for machined side surfaces of each sample. As indicated in Figure 56 (d), sample M-41, had no flaw indication at 2.25 MHz for the 0.51 mm designed defect. As previously examined, this defect was found to have a smaller diameter on CT scans compared to other flaws of identical design diameter. Unlike with the sample's as-manufactured side surfaces, the machined side surfaces provided flaw indications on all samples. With the exception of the aforementioned M-41, all flaws were detected at all frequencies once the sample's side surfaces were machined. These findings are significant, because prior to machining, most flaws were not detected at 2.25 MHz and 5 MHz. This is especially true for the smallest flaw in each sample, where at the two lowest frequencies no flaws were detected prior to machining. Once surface machining was completed on these samples eleven of the twelve known defects were identified.

4.5 Ultrasonic Inspection Surface Roughness Analysis

As presented in the previous sections, when the surface finish of a sample is reduced, the ability to detect smaller defects is increased. Figure 58 and Figure 59 clearly

shows for 2.25 MHz and 5 MHz a higher percentage of the designed defects are detected at lower surface roughness. Figure 58 also indicates the irregularity noted previously with sample M-41 at a frequency of 2.25 MHz. Analyzing these diagrams, several patterns are observed. For UT performed at 2.25 MHz and 5 MHz, no defects were detected on a surface with a roughness greater than 40.9 μm. Using a 2.25 MHz transducer, 24 scans were conducted on surfaces with a roughness of less than 22 μm. These 24 scans inspected 120 flaws, and only failed to detect one designed defect, the 0.51 mm defect in sample M-41. At a frequency of 5 MHz, all designed defects were detected through surfaces of less than 22 μm. In the range of 22 μm to 27 μm, four scans were performed inspecting 20 defects identifying eight of the 20. This range appears as a transition zone, since above this range no defects were found and below all defects are identified at 5 MHz. An equivalent chart was not prepared for 10 MHz since all designed defects were identified in the samples tested regardless of surface roughness.

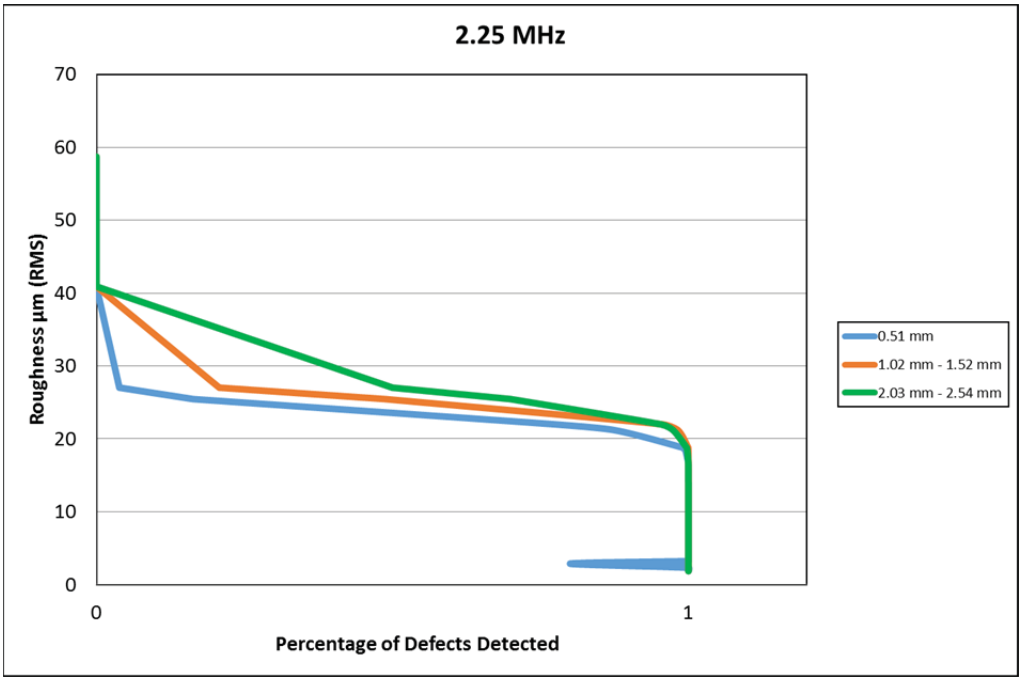

Figure 58. Percentage of defects detected at measured surface roughness at 2.25 MHz

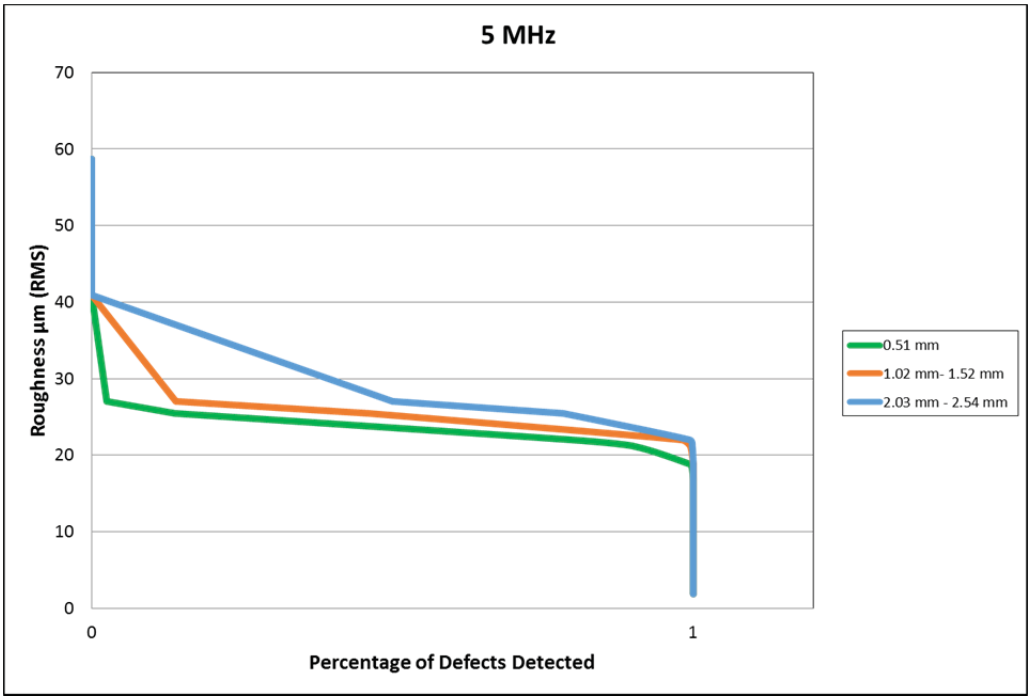

Figure 59. Percentage of defects detected at measured surface roughness at 5 MHz

4.6 Conclusion of Results

Table 7 shows an overview of all inspections performed as a ratio of flaws detected to known flaws inspected. It is concluded, at lower frequencies, as-manufactured side surfaces with high surface roughness provide no detection of the embedded flaws. Top as-manufactured surfaces appear to provide consistent detection of a spherical defect as small as 0.51 mm. Certain samples with lower as-manufactured side surfaces did provide positive identification of larger flaws. The size of the smallest flaw detected was dependent on the surface roughness as well as the frequency of the inspection.

Table 7. Number of designed defects detected

			Flaw Design Dimeter (mm)				
Frequency	Condition		0.51	1.02	1.52	2.03	2.54
2.25 MHz	As-manufactured	Top Face	12/12	12/12	12/12	12/12	12/12
		Side Face	0/12	4/12	4/12	4/12	4/12
	Milled	Top Face	6/6	6/6	6/6	6/6	6/6
		Side Face	5/6	6/6	6/6	6/6	6/6
5 MHz	As-manufactured	Top Face	12/12	12/12	12/12	12/12	12/12
		Side Face	0/12	1/12	1/12	3/12	3/12
	Milled	Top Face	6/6	6/6	6/6	6/6	6/6
		Side Face	6/6	6/6	6/6	6/6	6/6
10 MHz	As-manufactured	Top Face	12/12	12/12	12/12	12/12	12/12
		Side Face	12/12	12/12	12/12	12/12	12/12
	Milled	Top Face	6/6	6/6	6/6	6/6	6/6
		Side Face	6/6	6/6	6/6	6/6	6/6

Figure 60 gives a representation of designed flaw size detectable for samples with a surface roughness less than 22 μm RMS. All frequencies used for testing demonstrate the ability to identify a designed defect greater than 1.02 mm in diameter. Frequencies at 5 MHz and 10 MHz were able to distinguish all flaws with a designed diameter of 0.051

cm or larger through a surface of less than 22 µm RMS. 2.25 MHz scans were able to detect 0.51 mm flaws on all samples with a surface roughness less than 22 µm with the single exception of sample M-41. Figure 61 reveals the ability to detect flaws through surfaces rougher than 22 µm is reduced. When inspected through a rougher surface, above 22 µm, frequency appears to have more of an impact on detectable flaw size. At an inspection frequency of 10 MHz all flaws were found even through the roughest surfaces inspected. However at lower frequencies smaller known flaws in the samples were unidentified.

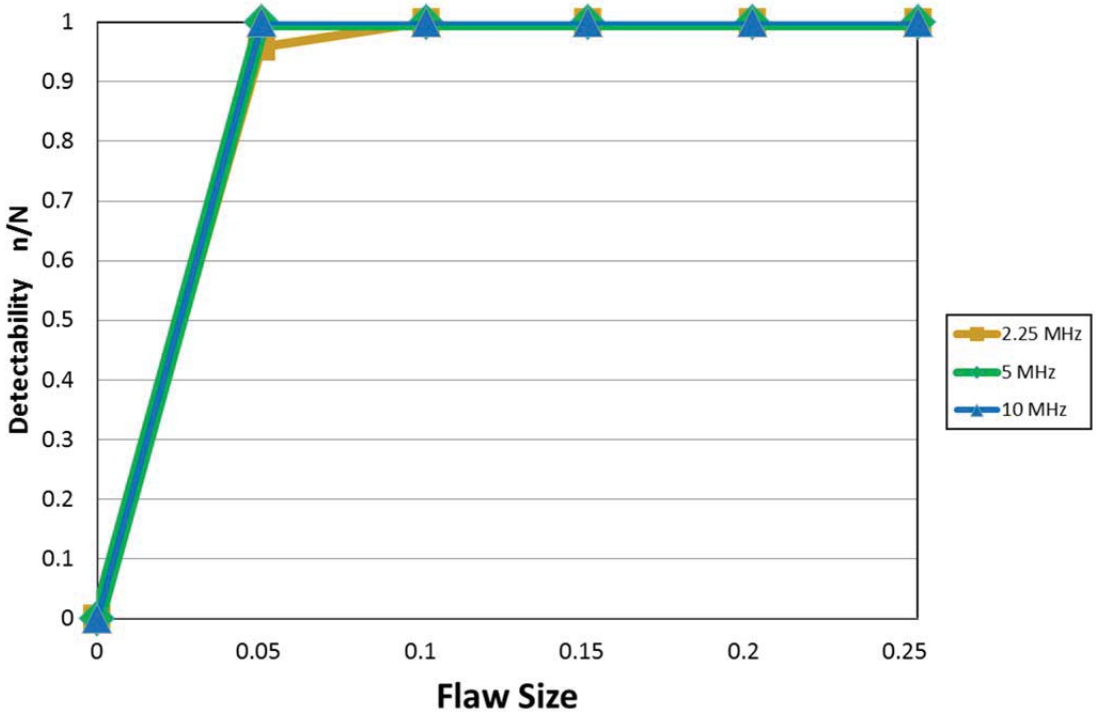

Figure 60. Detectable flaw of sample with surface roughness below 22 µm RMS

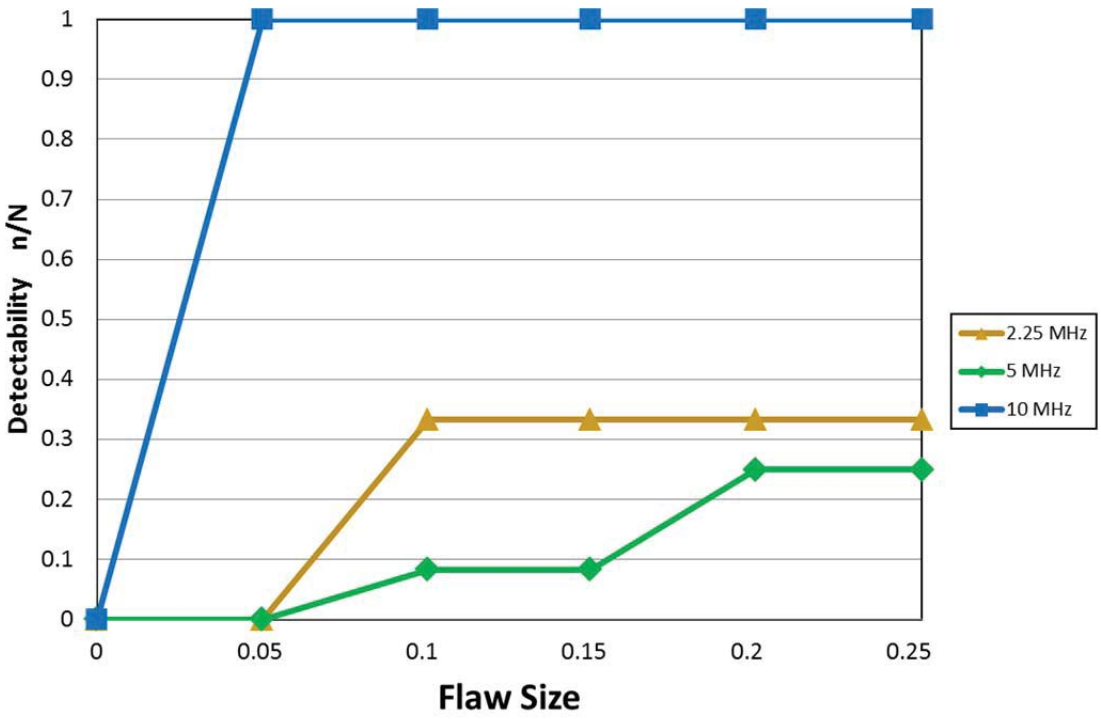

Figure 61. Detectable flaw of sample with surface roughness over 22 µm RMS

V. Conclusions and Recommendations

5.1 Review of Research Objectives

The primary goal of this research was to investigate the effect of surface roughness on UT of EBM Ti-6Al-4V and to determine whether the ability to detect known defects in a sample improves with the reduction of surface roughness. To fulfill this goal, research was conducted to support the following research objectives:

1. Determine to what extent an as-manufactured versus a machined surface affects the ability of ultrasonic testing to detect known defects in a Ti-6Al-4V sample.
2. Determine detectable size of flaw as a function of ultrasonic frequency, on a range of frequencies from 2.25 to 10 MHz.
3. Determine the effect of depth of a defect on the detectability over a range of frequencies from 2.25 to 10 MHz.

A total of 12 specimens were manufactured in six production runs with either an ARCAM A2 or Q10 system at Oak Ridge National Laboratories. One sample of each production run was machined on two adjacent faces to reduce the surface roughness of the as-manufactured sample.

The first research objective was satisfied through UT of as-built test specimens using three inspection frequencies, 2.25 MHz, 5 MHz and 10 MHz. Test results from the as-built and machined specimens demonstrated as-built top surfaces and machined surfaces show better flaw detection than as-built side surfaces at 2.25 MHz and 5 MHz. Additionally, when 10 MHz was employed as an inspection frequency all flaws were

detected regardless of surface roughness or sample orientation. Experimental data indicates improvement to the likelihood of identifying internal defects once an as-manufactured surface was machined. The ability to detect flaws also increases as inspection frequency is increased from 5 MHz to 10 MHz regardless of machining.

Objective 2 was fulfilled through the correlation of flaw sizes providing positive indication with inspection frequency regardless of surface roughness. Based on the data collected using the outlined methods a transition in detectability appears to occur in the range of 22 μm to 27 μm RMS of surface roughness. Based on this, all flaws with the exception of the smallest flaw in sample M-41 were detected through surfaces of less than 22 μm RMS while above this roughness detectability was reduced at 2.25 MHz and 5 MHz.

The thorough investigation of objective 3 was not conducted during this research. For all samples used in testing, defects were designed on the centerline of the specimen. This results in the only variation in depth of the flaw as the diameter, with the larger flaws having less material between the upper most point and the surface. Initially, it was thought this difference could correlate the depth of a flaw below the surface to its detectedability. Once scans were analyzed, it was discovered surfaces were not completely perpendicular or parallel to one another. Furthermore, with the inability to destructively inspect the sample following NDI, actual depths, much like actual flaw diameters, were indistinguishable.

5.2 Recommendations for Future Work

Experimental data collected and analyzed during this study provides an initial evaluation of the impact of surface roughness to the UT of EMB Ti-6Al-4V specimens. Such insight is beneficial to the future use of AM components on aircraft and is a necessary step to ensure build quality and provide for recurring inspection of in-use components. As outlined by the NIST AM roadmap, exploration of existing NDI techniques is required, along with identification of candidate techniques applicable to AM [11]. This thesis follows the near term goal of identifying practical methods for post manufacturing inspection of AM materials. Given the preliminary nature of this research many areas of future work were identified throughout the process. Some aspects of future work came from the number of samples available to test. Others facets stem from the simplistic design of the existing samples.

The simple geometry of both the samples and flaws contained therein was important to the initial capability assessment of UT on EBM Ti-6Al-4V. Since certain parameters were identified in this research, exploration of more complex geometry is possible, both in the sample and in the flaws. The next generation of samples, intended for further testing, have replaced the spherical defects with a twisting flat wide flaw. This new design is intended to more closely simulate an internal crack in the sample. Further evolution in the design of test specimen should include complex external geometry. The simple bar design of the samples tested in this research does not fully exercise the capability of AM. Replacement with an off-the-shelf wrought product is more feasible for components of this design. Therefore a sample design more resembling

an end component for an aircraft would allow for a more realistic understanding of UTs capability in this application.

Traditionally when a new material or NDI technique is introduced, the capabilities are explored on several levels. The primary focus is to identify a confidence level for detection of various sized flaws, by compiling the results from oftentimes hundreds of inspections [40]. Data from these studies is presented as a probability of detection for a specific method under specific conditions [40]. For the development of probability of detection data many more samples are needed for testing. MIL-HDBK-1823A suggests in order to provide reasonable precision at least 60 targeted sites require inspection if the system is to provide a binary, hit/miss response [44]. Given the data obtained in the research of this thesis, a smaller focused range of data points will allow a more concise collection of future data.

As mentioned in the motivation, inspection of in-use AM components is desired. The ability to UT components of an aircraft without full disassembly and removal of the component currently exist through the use of portable UT equipment. With the implementation of AM materials in aircraft comes the need to periodically inspect those materials. While this research used laboratory quality UT equipment for the purpose of evaluation, the viability of portable systems was not explored. Future work of establishing limits and conditions for the use of this portable field level UT equipment will establish the capability of these existing systems to find flaws. It was shown through the work conducted, UT is a viable option to detect flaws in samples under the optimal

conditions of an immersion tank but has not explored the practicality under the conditions of a flight line or maintenance hangar.

The data presented in this thesis shows for 2.25 MHz and 5 MHz there is a range between 22 μm RMS and 27 μm RMS where flaws transition from undetectable to detectable. This range presents the opportunity to identify a specific roughness or a smaller range where the transition of detectability occurs. Additional UT scans collected on surfaces with a roughness in the range of 22 μm RMS to 27 μm RMS oriented both through the top and side surfaces will assist in the understanding of surface roughness and orientation relationship.

Flaws with a diameter greater than 0.51 mm were always identified at a frequency of 10 MHz. Additional samples with flaws progressively smaller than 0.51 mm will aid in the determination of the minimum diameter 10 MHz transducers can reliably detect. As addressed in MIL-HDBK-1823A, there is a tendency to include more large targets than necessary in NDI testing [44]. Previous research by Margetan *et. al.*, show UT inspection data with positive returns for induced flaws in the range of 0.20 mm for titanium forgings [41]. The goal of NDI studies is not to identify the smallest detectable defect, but the largest undetectable defect [44]. This information is then used in the design phase of a component to compensate for the possible undetected flaw. It is important to identify these limits for AM and compare them to the established data for wrought or cast material.

5.3 Discussion of Results

Experimental data from this report indicates an overall improvement in detectability of flaws using UT on EBM Ti-6Al-4V with reduction in surface roughness. At frequencies of 2.25 MHz and 5 MHz orientation of the inspections surface, side versus top, appears to have no impact on the ability to detect internal defects. However surface roughness has a direct impact on the ability to identify defects at these low frequencies. As discussed in the previous chapter an as-manufactured side surface with a roughness greater than 40.9 μm RMS provides no detection of defects. When the same surface is inspected after machining, through a surface roughness of less than 7.9 μm RMS all designed defects were identified. It was also discovered the electron beam current pattern was seen throughout the thickness of a sample, even with surface striations removed through machining. In certain cases, this has the potential to mask defects within a sample under inspection.

Inspections performed at 10 MHz produced high intensity returns through side surfaces of samples, both in as-manufactured and machined condition. The same scans taken through the top surface at 10 MHz include irregularities, such as grain scatter and returns from varying electron beam current distribution patterns. This leads to the premise of build direction and scan orientation affecting the ability to identify defects in a sample at certain frequencies. It was shown, within the range of surface roughness available for this research, 10 MHz inspections are not affected by sample surface roughness to the extent of 2.25 MHz and 5 MHz inspections. With the potential future

use of AM for critical components it is important to understand inspection techniques and the limitations associated with their use on AM materials.

Appendix A. As-Manufactured Top Surface Flaw Identification

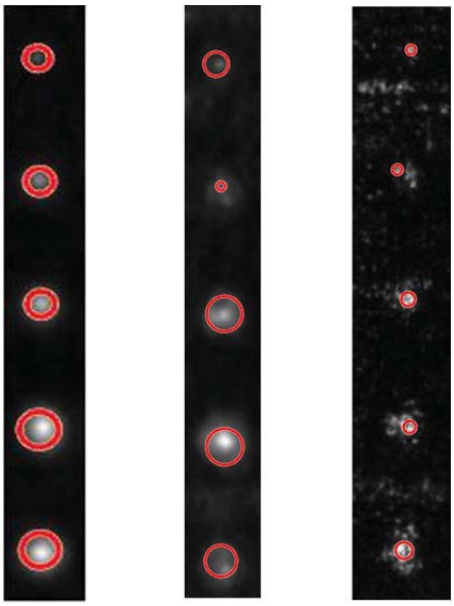

Figure 62. Sample B-42 as-manufactured top surface with roughness of 16.1 µm RMS (a) 2.25 MHz, (b) 5 MHz, (c) 10 MHz

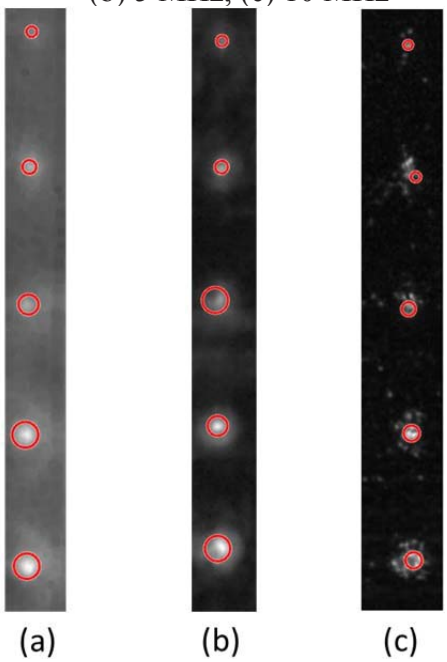

Figure 63. Sample D-41 as-manufactured top surface with roughness of 18.8 µm RMS (a) 2.25 MHz, (b) 5 MHz, (c) 10 MHz

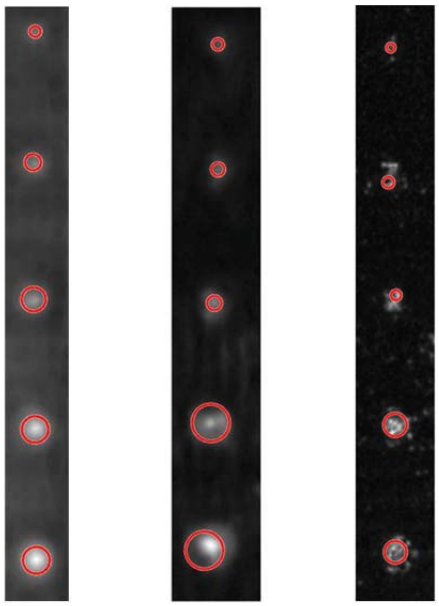

Figure 64. Sample D-42 as-manufactured Top Surface with roughness of 18.7 µm RMS (a) 2.25 MHz, (b) 5 MHz, (c) 10 MHz

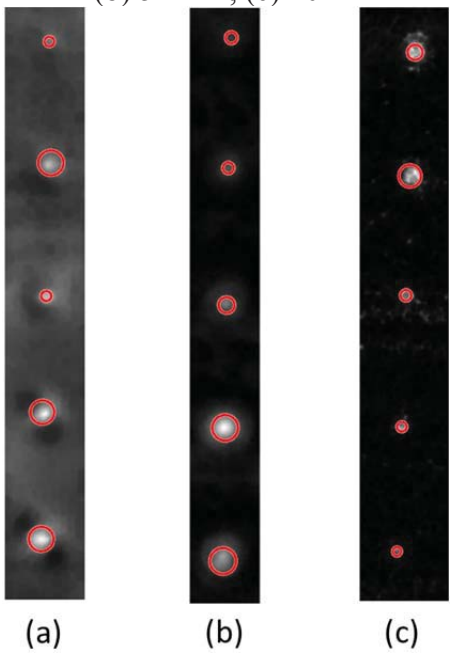

Figure 65. Sample E-41 as-manufactured top surface with roughness of 16.2 µm RMS (a) 2.25 MHz, (b) 5 MHz, (c) 10 MHz

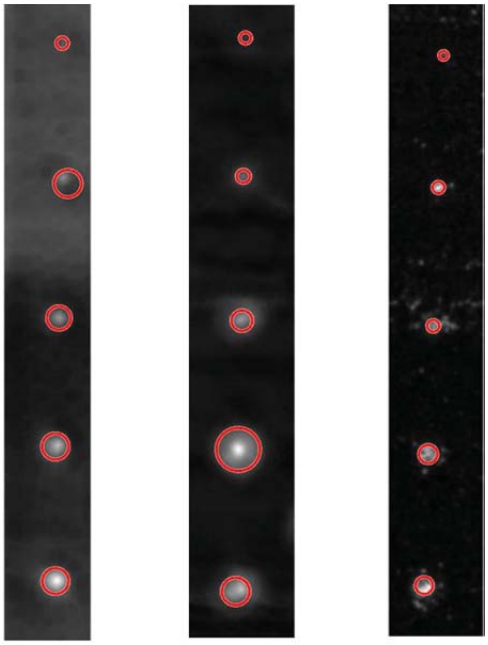

Figure 66. Sample E-42 as-manufactured top surface with roughness of 15.5 µm RMS (a) 2.25 MHz, (b) 5 MHz, (c) 10 MHz

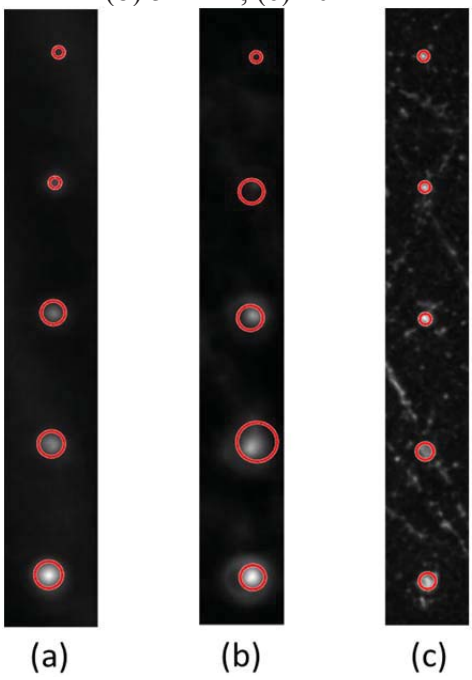

Figure 67. Sample L-41 as-manufactured top surface with roughness of 11.1 µm RMS (a) 2.25 MHz, (b) 5 MHz, (c) 10 MHz

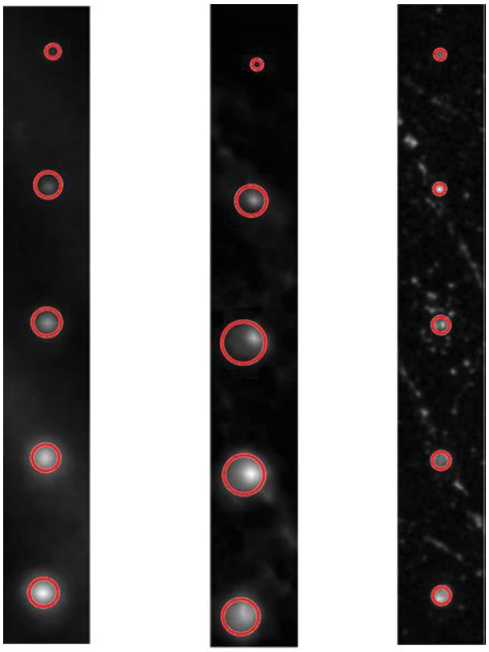

Figure 68. Sample L-42 as-manufactured top surface with roughness of 16.5 µm RMS(a) 2.25 MHz, (b) 5 MHz, (c) 10 MHz

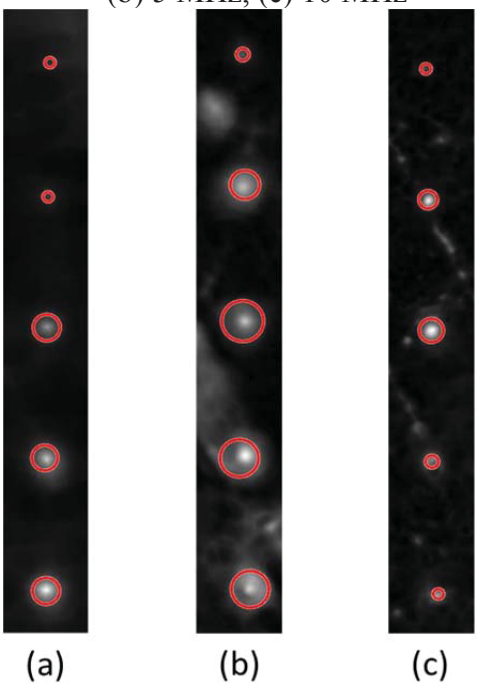

Figure 69. Sample M-41 as-manufactured top surface with roughness of 18.3 µm RMS (a) 2.25 MHz, (b) 5 MHz, (c) 10 MHz

Appendix B. As-Manufactured Side Surface Flaw Identification

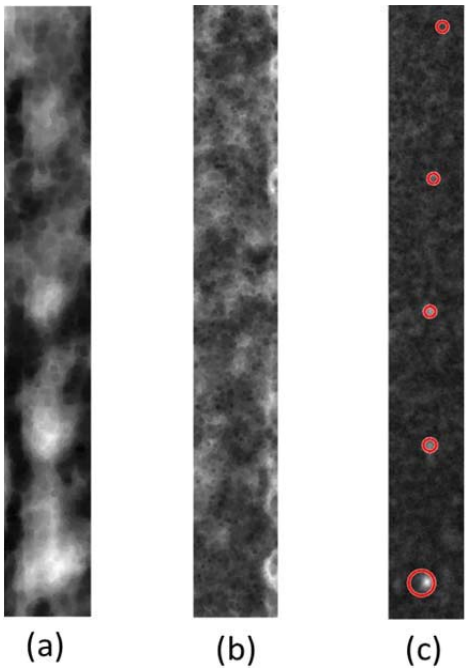

Figure 70. Sample A-42 as-manufactured side surface with roughness of 45.14 µm RMS(a) 2.25 MHz, (b) 5 MHz, (c) 10 MHz

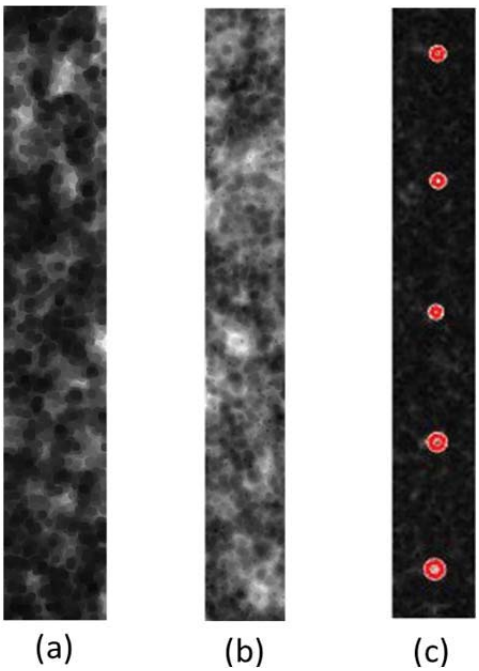

Figure 72. Sample B-42 as-manufactured side surface with roughness of 40.91 µm RMS (a) 2.25 MHz, (b) 5 MHz, (c) 10 MHz

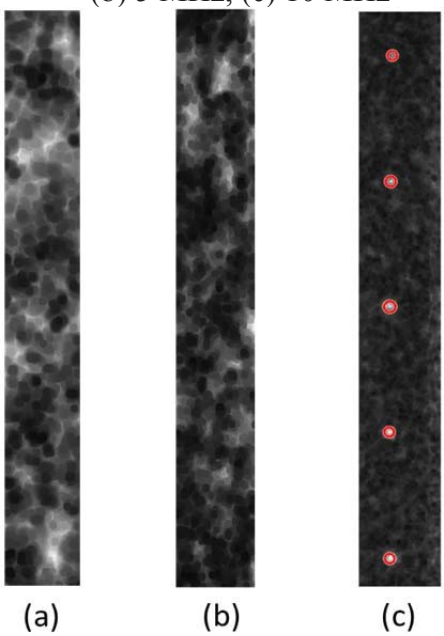

Figure 71. Sample B-41 as-manufactured side surface with roughness of 40.91 µm RMS(a) 2.25 MHz, (b) 5 MHz, (c) 10 MHz

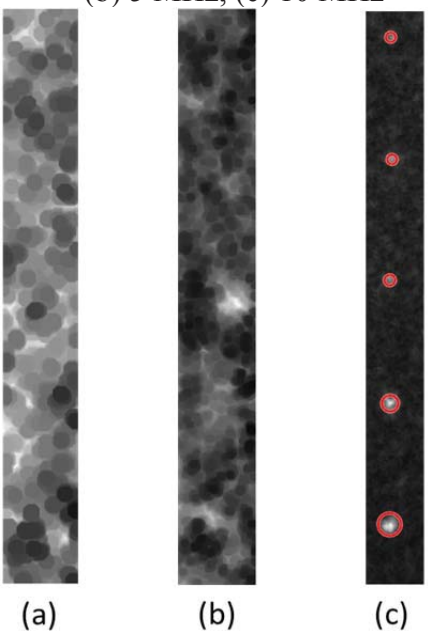

Figure 73. Sample D-41 as-manufactured side surface with roughness of 58.7 µm RMS (a) 2.25 MHz, (b) 5 MHz, (c) 10 MHz

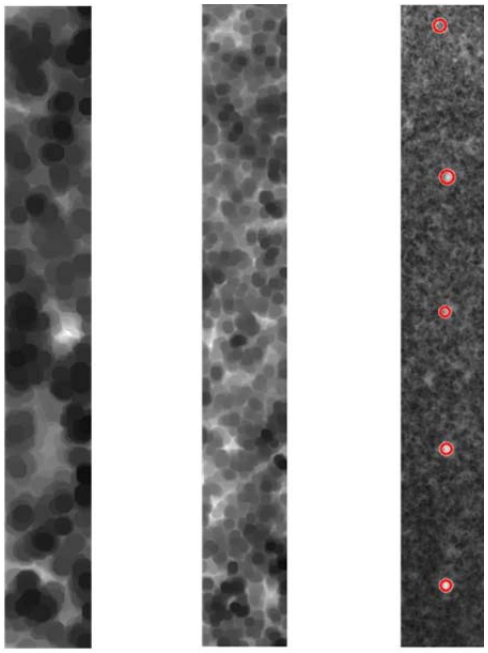

Figure 74. Sample D-42 as-manufactured side surface with roughness of 58.7 µm RMS (a) 2.25 MHz, (b) 5 MHz, (c) 10 MHz

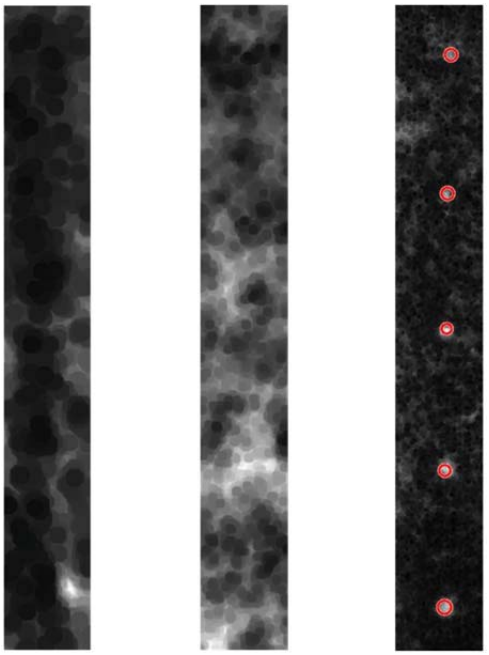

Figure 76. Sample E-42 as-manufactured side surface with roughness of 43.78 µm RMS (a) 2.25 MHz, (b) 5 MHz, (c) 10 MHz

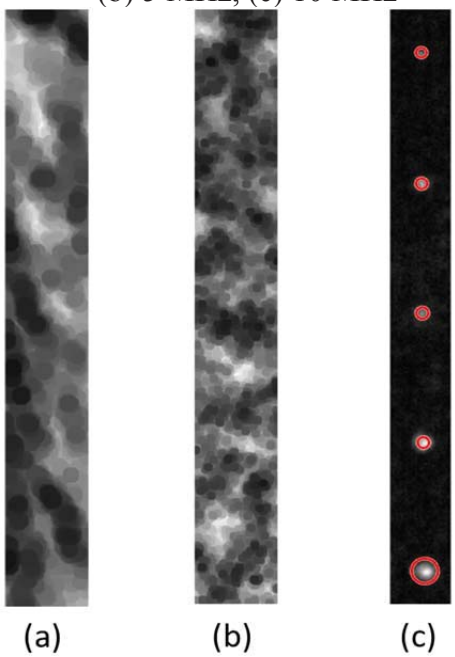

Figure 75. Sample E-41 as-manufactured side surface with roughness of 43.78 µm RMS(a) 2.25 MHz, (b) 5 MHz, (c) 10 MHz

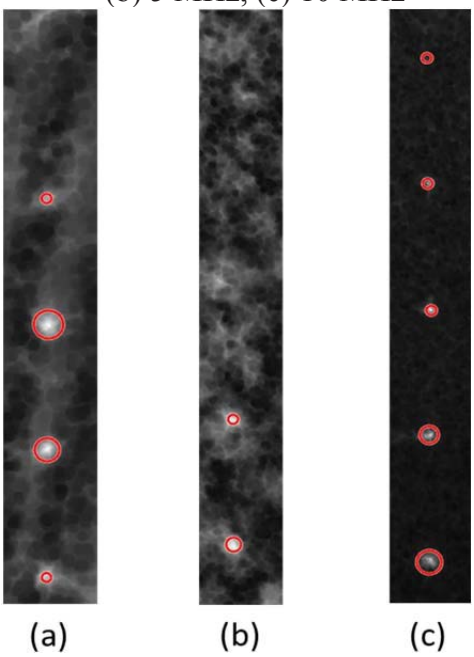

Figure 77. Sample L-41 as-manufactured side surface with roughness of 25.46 µm RMS (a) 2.25 MHz, (b) 5 MHz, (c) 10MHz

Appendix C. Machined Top Surface Flaw Identification

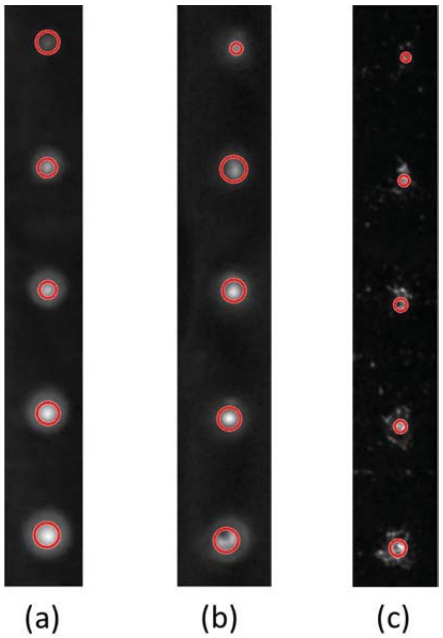

Figure 78. Sample D-41 machined top surface with roughness of 3.23 µm RMS (a) 2.25 MHz, (b) 5 MHz, (c) 10 MHz

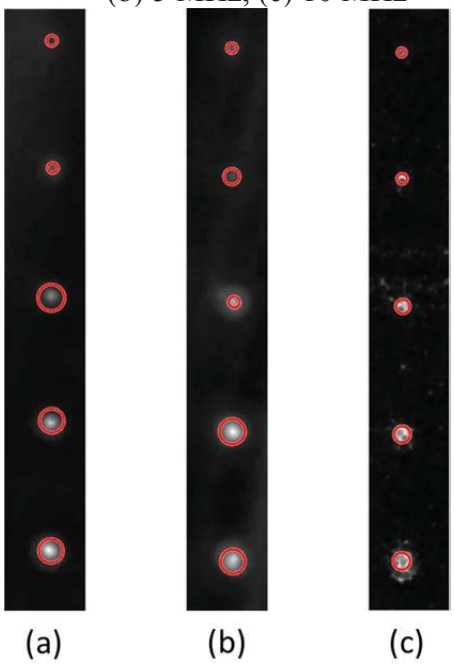

Figure 79. Sample E-41 machined top surface with roughness of 3.85 µm RMS (a) 2.25 MHz, (b) 5 MHz, (c) 10 MHz

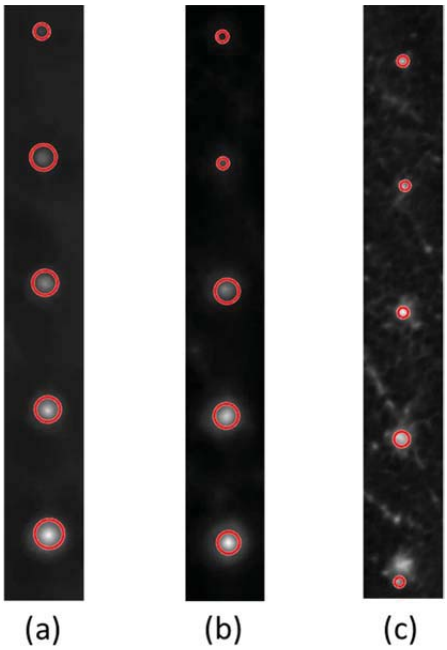

Figure 80. Sample L-41 machined top surface with roughness of 1.86 µm RMS (a) 2.25 MHz, (b) 5 MHz, (c) 10 MHz

Appendix D. Machined Side Surface Flaw Identification

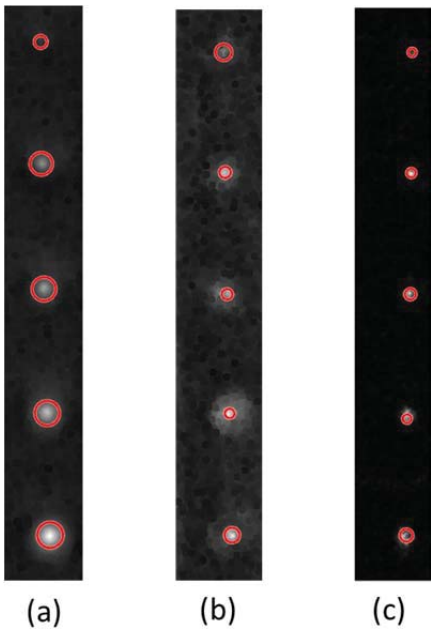

Figure 81. Sample B-41 machined side surface with roughness of 7.91 µm RMS (a) 2.25 MHz, (b) 5 MHz, (c) 10 MHz

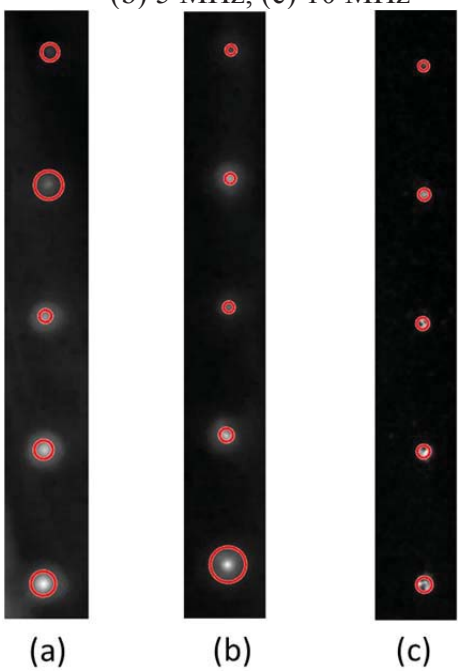

Figure 82. Sample D-41 machined side surface with roughness of 5.5 µm RMS (a) 2.25 MHz, (b) 5 MHz, (c) 10 MHz

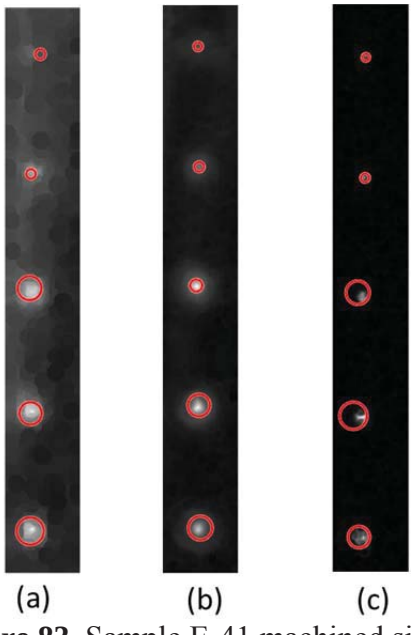

Figure 83. Sample E-41 machined side surface with roughness of 5.7 µm RMS (a) 2.25 MHz, (b) 5 MHz, (c) 10 MHz

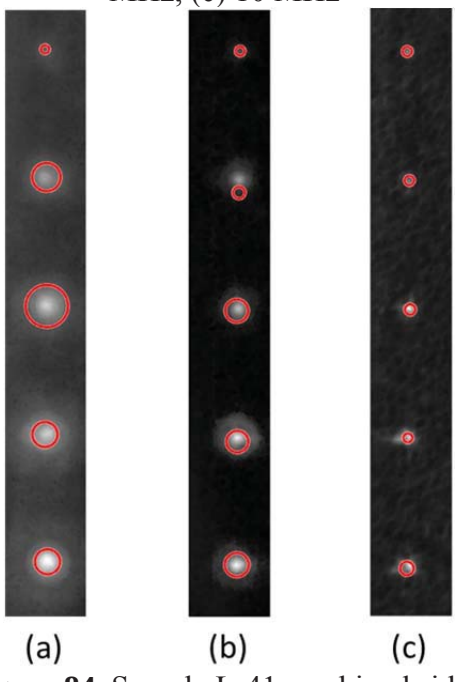

Figure 84. Sample L-41 machined side surface with roughness of 2.32 µm RMS (a) 2.25 MHz, (b) 5 MHz, (c) 10 MHz

Appendix E. Detection Data As-Manufactured Top Surfaces

Table 8. 2.25 MHz UT scan as-manufactured top surface

			Flaw Designed Dimeter (mm)				
Sample	Surface (µm)	Peak to Peak (µm)	0.51	1.02	1.52	2.03	2.54
A-41	16.8	115.3	Hit	Hit	Hit	Hit	Hit
A-42	16.1	102.6	Hit	Hit	Hit	Hit	Hit
B-41	22	103.8	Hit	Hit	Hit	Hit	Hit
B-42	21.2	127	Hit	Hit	Hit	Hit	Hit
D-41	18.8	118.5	Hit	Hit	Hit	Hit	Hit
D-42	18.7	118.7	Hit	Hit	Hit	Hit	Hit
E-41	16.2	83.6	Hit	Hit	Hit	Hit	Hit
E-42	15.5	93.7	Hit	Hit	Hit	Hit	Hit
L-41	11.1	71.3	Hit	Hit	Hit	Hit	Hit
L-42	16.5	101.7	Hit	Hit	Hit	Hit	Hit
M-41	18.3	88	Hit	Hit	Hit	Hit	Hit
M-42	15.8	99.8	Hit	Hit	Hit	Hit	Hit

Table 9. 5 MHz UT scan as-manufactured top surface

			Flaw Design Dimeter (mm)				
Sample	Surface (µm)	Peak to Peak (µm)	0.51	1.02	1.52	2.03	2.54
A-41	16.8	115.3	Hit	Hit	Hit	Hit	Hit
A-42	16.1	102.6	Hit	Hit	Hit	Hit	Hit
B-41	22	103.8	Hit	Hit	Hit	Hit	Hit
B-42	21.2	127	Hit	Hit	Hit	Hit	Hit
D-41	18.8	118.5	Hit	Hit	Hit	Hit	Hit
D-42	18.7	118.7	Hit	Hit	Hit	Hit	Hit
E-41	16.2	83.6	Hit	Hit	Hit	Hit	Hit
E-42	15.5	93.7	Hit	Hit	Hit	Hit	Hit
L-41	11.1	71.3	Hit	Hit	Hit	Hit	Hit
L-42	16.5	101.7	Hit	Hit	Hit	Hit	Hit
M-41	18.3	88	Hit	Hit	Hit	Hit	Hit
M-42	15.8	99.8	Hit	Hit	Hit	Hit	Hit

Table 10. 10 MHz UT scan as-manufactured top surface

			Flaw Designed Dimeter (mm)				
Sample	Surface (μm)	Peak to Peak (μm)	0.51	1.02	1.52	2.03	2.54
A-41	45.14	307	Hit	Hit	Hit	Hit	Hit
A-42	45.14	307	Hit	Hit	Hit	Hit	Hit
B-41	40.91	268.52	Hit	Hit	Hit	Hit	Hit
B-42	40.91	268.52	Hit	Hit	Hit	Hit	Hit
D-41	58.7	439.12	Hit	Hit	Hit	Hit	Hit
D-42	58.7	439.12	Hit	Hit	Hit	Hit	Hit
E-41	43.78	320.15	Hit	Hit	Hit	Hit	Hit
E-42	43.78	320.15	Hit	Hit	Hit	Hit	Hit
L-41	25.46	202.82	Hit	Hit	Hit	Hit	Hit
L-42	25.46	202.82	Hit	Hit	Hit	Hit	Hit
M-41	27.03	208.95	Hit	Hit	Hit	Hit	Hit
M-42	27.03	208.95	Hit	Hit	Hit	Hit	Hit

Appendix F. Detection Data As-Manufactured Side Surfaces

Table 11. 2.25 MHz UT scan as-manufactured side surface

			Flaw Design Dimeter (mm)				
Sample	Surface (µm)	Peak to Peak (µm)	0.51	1.02	1.52	2.03	2.54
A-41	45.14	307	Miss	Miss	Miss	Miss	Miss
A-42	45.14	307	Miss	Miss	Miss	Miss	Miss
B-41	40.91	268.52	Miss	Miss	Miss	Miss	Miss
B-42	40.91	268.52	Miss	Miss	Miss	Miss	Miss
D-41	58.7	439.12	Miss	Miss	Miss	Miss	Miss
D-42	58.7	439.12	Miss	Miss	Miss	Miss	Miss
E-41	43.78	320.15	Miss	Miss	Miss	Miss	Miss
E-42	43.78	320.15	Miss	Miss	Miss	Miss	Miss
L-41	25.46	202.82	Miss	Hit	Hit	Hit	Hit
L-42	25.46	202.82	Miss	Hit	Hit	Hit	Hit
M-41	27.03	208.95	Miss	Hit	Hit	Hit	Hit
M-42	27.03	208.95	Miss	Hit	Hit	Hit	Hit

Table 12. 5 MHz UT scan as-manufactured side surface

			Flaw Design Dimeter (mm)				
Sample	Surface (µm)	Peak to Peak (µm)	0.51	1.02	1.52	2.03	2.54
A-41	45.14	307	Miss	Miss	Miss	Miss	Miss
A-42	45.14	307	Miss	Miss	Miss	Miss	Miss
B-41	40.91	268.52	Miss	Miss	Miss	Miss	Miss
B-42	40.91	268.52	Miss	Miss	Miss	Miss	Miss
D-41	58.7	439.12	Miss	Miss	Miss	Miss	Miss
D-42	58.7	439.12	Miss	Miss	Miss	Miss	Miss
E-41	43.78	320.15	Miss	Miss	Miss	Miss	Miss
E-42	43.78	320.15	Miss	Miss	Miss	Miss	Miss
L-41	25.46	202.82	Miss	Miss	Miss	Hit	Hit
L-42	25.46	202.82	Miss	Miss	Miss	Hit	Hit
M-41	27.03	208.95	Miss	Hit	Hit	Hit	Hit
M-42	27.03	208.95	Miss	Miss	Miss	Miss	Miss

Table 13. 10 MHz UT scan as-manufactured side surface

			Flaw Designed Dimeter (mm)				
Sample	Surface (μm)	Peak to Peak (μm)	0.51	1.02	1.52	2.03	2.54
A-41	45.14	307	Hit	Hit	Hit	Hit	Hit
A-42	45.14	307	Hit	Hit	Hit	Hit	Hit
B-41	40.91	268.52	Hit	Hit	Hit	Hit	Hit
B-42	40.91	268.52	Hit	Hit	Hit	Hit	Hit
D-41	58.7	439.12	Hit	Hit	Hit	Hit	Hit
D-42	58.7	439.12	Hit	Hit	Hit	Hit	Hit
E-41	43.78	320.15	Hit	Hit	Hit	Hit	Hit
E-42	43.78	320.15	Hit	Hit	Hit	Hit	Hit
L-41	25.46	202.82	Hit	Hit	Hit	Hit	Hit
L-42	25.46	202.82	Hit	Hit	Hit	Hit	Hit
M-41	27.03	208.95	Hit	Hit	Hit	Hit	Hit
M-42	27.03	208.95	Hit	Hit	Hit	Hit	Hit

Appendix G. Detection Data Machined Top Surfaces

Table 14. 2.25 MHz UT scan milled top surface

			Flaw Designed Dimeter (mm)				
Sample	Surface (µm)	Peak to Peak (µm)	0.51	1.02	1.52	2.03	2.54
A-41	3.22	17.43	Hit	Hit	Hit	Hit	Hit
B-41	5.02	20.77	Hit	Hit	Hit	Hit	Hit
D-41	3.23	16.27	Hit	Hit	Hit	Hit	Hit
E-41	3.85	24.77	Hit	Hit	Hit	Hit	Hit
L-41	1.86	9.35	Hit	Hit	Hit	Hit	Hit
M-41	3.72	13.67	Hit	Hit	Hit	Hit	Hit

Table 15. 5 MHz UT scan milled top surface

			Flaw Designed Dimeter (mm)				
Sample	Surface (µm)	Peak to Peak (µm)	0.51	1.02	1.52	2.03	2.54
A-41	3.22	17.43	Hit	Hit	Hit	Hit	Hit
B-41	5.02	20.77	Hit	Hit	Hit	Hit	Hit
D-41	3.23	16.27	Hit	Hit	Hit	Hit	Hit
E-41	3.85	24.77	Hit	Hit	Hit	Hit	Hit
L-41	1.86	9.35	Hit	Hit	Hit	Hit	Hit
M-41	3.72	13.67	Hit	Hit	Hit	Hit	Hit

Table 16. 10 MHz UT scan milled top surface

			Flaw Designed Dimeter (mm)				
Sample	Surface (µm)	Peak to Peak (µm)	0.51	1.02	1.52	2.03	2.54
A-41	3.22	17.43	Hit	Hit	Hit	Hit	Hit
B-41	5.02	20.77	Hit	Hit	Hit	Hit	Hit
D-41	3.23	16.27	Hit	Hit	Hit	Hit	Hit
E-41	3.85	24.77	Hit	Hit	Hit	Hit	Hit
L-41	1.86	9.35	Hit	Hit	Hit	Hit	Hit
M-41	3.72	13.67	Hit	Hit	Hit	Hit	Hit

Appendix H. Detection Data Machined Side Surfaces

Table 17. 2.25 MHz UT scan milled side surface

			Flaw Designed Dimeter (mm)				
Sample	Surface (µm)	Peak to Peak (µm)	0.51	1.02	1.52	2.03	2.54
A-41	7.1	28.1	Hit	Hit	Hit	Hit	Hit
B-41	7.91	27.8	Hit	Hit	Hit	Hit	Hit
D-41	5.5	30.7	Hit	Hit	Hit	Hit	Hit
E-41	5.7	25.19	Hit	Hit	Hit	Hit	Hit
L-41	2.32	10.58	Hit	Hit	Hit	Hit	Hit
M-41	2.88	13.6	Miss	Hit	Hit	Hit	Hit

Table 18. 5 MHz UT scan milled side surface

			Flaw Designed Dimeter (mm)				
Sample	Surface (µm)	Peak to Peak (µm)	0.51	1.02	1.52	2.03	2.54
A-41	7.1	28.1	Hit	Hit	Hit	Hit	Hit
B-41	7.91	27.8	Hit	Hit	Hit	Hit	Hit
D-41	5.5	30.7	Hit	Hit	Hit	Hit	Hit
E-41	5.7	25.19	Hit	Hit	Hit	Hit	Hit
L-41	2.32	10.58	Hit	Hit	Hit	Hit	Hit
M-41	2.88	13.6	Hit	Hit	Hit	Hit	Hit

Table 19. 10 MHz UT scan milled side surface

			Flaw Designed Dimeter (mm)				
Sample	Surface (µm)	Peak to Peak (µm)	0.51	1.02	1.52	2.03	2.54
A-41	7.1	28.1	Hit	Hit	Hit	Hit	Hit
B-41	7.91	27.8	Hit	Hit	Hit	Hit	Hit
D-41	5.5	30.7	Hit	Hit	Hit	Hit	Hit
E-41	5.7	25.19	Hit	Hit	Hit	Hit	Hit
L-41	2.32	10.58	Hit	Hit	Hit	Hit	Hit
M-41	2.88	13.6	Hit	Hit	Hit	Hit	Hit

Bibliography

[1] H. Kodama, "Automatic method for fabrication a three-dimensional plastic model with photo-hardening polymer," *Review of Scientific Instruments,* vol. 52, no. 11, pp. 1770-1773, 1981.

[2] D. L. Walker, "Topology Optimization of an Aircraft Wing," Air University, Wright-Patterson Air Force Base, Ohio, 2015.

[3] R. Neal, "Dreambox: The World's First 3D Printing Vending Machine Hits UC Berkeley," *International Business Times,* 3 June 2013.

[4] S. Ford, "Additive Manufacturing Technology: Potential Implications for U.S. Manufacturing Competitveness," *Journal of International Commerce and Economics,* vol. 6, p. September, 2014.

[5] S. Shipp, "Emerging Global Trends in," Institute for Defense Analyses, Alexandria, 2012.

[6] J. Ruan, *A review of layer based manufacturing processes for metals,* Rolla: University of Missouri, 2006.

[7] C. M. McNulty, N. Arnas and T. Campbell, "Toward the Printed World:Additive Manufacturing and Implications for National Security," *Defense Horizons,* vol. 73, 2012.

[8] T. A. Yonkers, "What is the Price of Energy Security: from Battlefields to Bases," in *House Committee on Armed Services*, Washington, 2012.

[9] J. W. Lincoln, "Managing the Aging Aircraft Problem," Aeronautical Systems Center, Wright-Patterson Air Force Base, 2003.

[10] J. Waller, "Nondestructive Evaluation of Additive Manufacturing: State-of-the-Discipline Report," NASA Langley Research Center, Hampton, 2014.

[11] Energetics Incorporated, "Measurement Science Roadmap for Metal-Based Additive Manufacturing," National Institute of Standards and Technology, Columbia,

2013.

[12] E. Schwalbach, Interviewee, *Electron Beam Melting.* [Interview]. August 2015.

[13] Department of Defense, NONDESTRUCTIVE INSPECTION METHODS, BASIC THEORY, T.O. 33B-1-1, Robins Air Force Base: United States Air Force, 2014.

[14] I. Gibson, D. W. Rosen and B. Stucker, Additive Manufacturing Technologies, New York: Springer , 2010.

[15] K. Hartke, "MANUFACTURING TECHNOLOGY SUPPORT," AIR FORCE RESEARCH LABORATORY, Wright-Patterson Air Force Base, 2011.

[16] C. W. Hull, "Apparatus for Production of Three-dimensional Objects by Stereolithography". US Patent 4575330 A, 08 Aug 1984.

[17] C. Fink, "An Overview of Additive Manufacturing, part I," *AMMTIAC Quarterly,* vol. 4, no. 2, pp. 9-12, 2009.

[18] A. Safdar, "A Study on Electron Beam Melted Ti-6Al-4V," Lund University, Lund, Sweden, 2012.

[19] D. Cormier, O. Harrysson and H. West, "Characterization of h13 steel produced via electron beam melting," *Rapid Prototyping Journal,* vol. 10, no. 1, pp. 34-41, 2004.

[20] Arcam, *Arcam A2 - Additive Manufacturing for Aerospace Industry,* Mölndal: Arcam, 2013.

[21] ARCAM, "EBM Hardware," 2015. [Online]. Available: http://www.arcam.com/technology/electron-beam-melting/hardware. [Accessed 5 November 2015].

[22] Department of Defense, Metallic Materials and Elements for Aerospace Vehicle Structures, Mil-Hdbk-5j, Wright-Patterson: Department of Defense, 2003.

[23] A. Safdar, L. Wei, A. Snisb and Z. Lai, "Evaluation of microstructural development in electron beam melted Ti-6Al-4V," *Materials Characterization,* vol. 65, pp. 8-

15, 2012.

[24] J. Glockel and J. Beuth, "Understanding Ti-6Al-4V Microstructure Control in Additive Manufacturing via Process Maps," University of Texas, 2013.

[25] A. Antonysamy, J. Meyer and P. Prangnell, "Effect of build geometry on the beta-grain structure and texture in additive manufacture of Ti-6Al-4V selective electron beam melting," *Materials Characterization,* vol. 84, pp. 153-168, 2013.

[26] S. Doctor, T. Hall and L. Reid, "SAFT- The Evolution of a Signal Processing Technology for Ultrasonic Testing," Pacific Northwest Laboratory, Richland, 2003.

[27] Department of Defense, *Nondestructive Inspection Program Requirements for Aircraft and Missile Materials and Parts, Mil-Hdbk-6870B,* Wright-Patterson AFB: ASC/ENRS, 2012.

[28] Department of Defense, Nondestructive Evaluation System Reliability Assesment Mil-Hbdk-1823, Wright Patterson AFB, OH: Department of Defense, 1999.

[29] Department Of Defense, Military Handbook Ultrasonic Testing Mil-Hdbk-728/6, Department Of Defense, 1985.

[30] K. Taminger and R. Hafley, "Electron Beam Freeform Fabrication: A Rapid Metal Deposition Process," in *Annual Automotive Composites Conference*, Troy, 2003.

[31] P. Kobryn, N. Ontko, L. Perkins and J. Tiley, "Additive Manufacturing of Aerospace Alloys for Aircraft Structures.," in *NATO Research and Technology Organization-139*, Neuilly-sur-Seine, France, 2006.

[32] ASTM, *Standard Specifications for Additive Manufacturing Titanium-6 Aluminum-4 Vandium with Powder Bed Fusion,* West Conshohocken: ASTM International, 2014.

[33] ASTM, *Standard Terminology for Additive Manufacturing-Coordinate Systems and Test Methodologies,* West Conshohocken: ASTM Interntional, 2013.

[34] Arcam, *Arcam Q10 Technical Data,* Mölndal: Arcam AB, 2014.

[35] B. Mell, "Topography & Roughness Testing of Sandpaper Surface," Nanovea.

[36] Mathworks, *Matlab Documentatio: Fast Fourier Transform,* Mathworks, 2015.

[37] R. Fisher, S. Perkins, A. Walker and E. Wolfart, "Hough Transform: Image Transforms," Hypermedia, 2003.

[38] Mathworks, *Matlab Documentation: Find Circles Using Hough Transform,* Mathworks, 2015.

[39] E. Schwalbach, "Trip Report: Powder Bed Electron Beam Melting at Oak Ridge National Laboratory Manufacturing Demonstration Facility," Wright Patterson, OH, 2014.

[40] W. D. Rummel and G. A. Matzkanin, Nondestructive Evaluation Capabilities Data Book, Austin: Nondestructive Testing Information Analysis Center , 1997.

[41] F. Margetan, J. Umbach, R. Roberts and e. al., "Inspection Development for Titanium Forgings," U.S. Department of Transportation, Federal Aviation Administration, Washington, 2007.

[42] B. Thompson, T. Duffy, A. Kinney, J. Bartos, K. Smith, J. Umbach and L. Brasche, "Quarterly Report," Engine Titanium Consortium, 2001.

[43] E. Avallone and T. Baumeister, Marks' Standard Handbook for Mechanical Engineers, New York: MaGraw-Hill, 1996.

[44] Department of Defense, Nondestructive Evaluation System Reliability Assesment, MIL-HDBK-1823A, Wright Patterson: Department of Defense, 2009.

REPORT DOCUMENTATION PAGE

Form Approved
OMB No. 0704–0188

1. REPORT DATE (DD–MM–YYYY)	2. REPORT TYPE	3. DATES COVERED *(From — To)*
24-03-2016	Master's Thesis	Sept 2014- Mar 2016

4. TITLE AND SUBTITLE
Surface Roughness of Electron Beam Melting TI-6AL-4V Effect on Ultrasonic Testing

5a. CONTRACT NUMBER

5b. GRANT NUMBER

5c. PROGRAM ELEMENT NUMBER

6. AUTHOR(S)

Evan T. Hanks, Capt, USAF

5d. PROJECT NUMBER

5e. TASK NUMBER

5f. WORK UNIT NUMBER

7. PERFORMING ORGANIZATION NAME(S) AND ADDRESS(ES)
Air Force Institute of Technology
Graduate School of
2950 Hobson Way
WPAFB OH 45433-7765

8. PERFORMING ORGANIZATION REPORT NUMBER

AFIT-ENY-MS-16-M-216

9. SPONSORING / MONITORING AGENCY NAME(S) AND ADDRESS(ES)
Joint Aircraft Survivability Program
Dennis Lindell
735 S Courthouse Road Suite 1100 Arlington, VA 22204-2489
dennis.lindell@navy.mil

10. SPONSOR/MONITOR'S ACRONYM(S)
AFRL/RQRC

11. SPONSOR/MONITOR'S REPORT NUMBER(S)

12. DISTRIBUTION / AVAILABILITY STATEMENT
Distribution Statement A. Approved for Public Release; Distribution Unlimited

13. SUPPLEMENTARY NOTES
This work is declared a work of the U.S. Government and is not subject to copyright protection in the United States.

14. ABSTRACT

Experimental research was conducted on the effects of surface roughness on ultrasonic non-destructive testing of Electron Beam Melted (EBM) additively manufactured Ti-6Al-4V. Additive Manufacturing (AM) is a developing technology with many potential benefits, but certain challenges posed by its use require further research before AM parts are viable for widespread use in the aviation industry. Possible applications of this new technology include, Aircraft Battle Damage Repair (ABDR), small batch manufacturing to fill supply gaps, and replacement for obsolete parts. The research presented here assesses the effectiveness of ultrasonic inspection in detecting manufactured flaws in EBM manufactured Ti-6Al-4V. EBM products are known to have high surface roughness in as-manufactured condition, and surface roughness is known to affect the results of ultrasonic inspections. The experimental data from this research demonstrates the ability of ultrasonic inspections to identify flaws as small as 0.51 mm at 2.25 MHz, 5 MHz and 10 MHz through a machined surface. A frequency of 10 MHz provides better results than 2.25 MHz and 5 MHz through an as manufactured surface, where the highest natural surface roughness is present.

15. SUBJECT TERMS
Additive Manufacturing, Nondestructive Inspection, Ultrasonic Testing,

16. SECURITY CLASSIFICATION OF:			17. LIMITATION OF ABSTRACT	18. NUMBER OF PAGES	19a. NAME OF RESPONSIBLE PERSON
a. REPORT	b. ABSTRACT	c. THIS PAGE			Maj David Liu, AFIT/ENY
U	U	U	U	128	19b. TELEPHONE NUMBER (Include Area Code) (937) 255-3636, ext 4542

Standard Form 298 (Rev. 8–98)
Prescribed by ANSI Std. Z39.18